Design of an Impedance-based, Gold Nanoparticle Enhanced Biosensor System

By

Scott MacKay

A thesis submitted in partial fulfillment of the requirements for the degree of

Doctor of Philosophy

in

Biomedical Engineering

Department of Electrical and Computer Engineering
University of Alberta

Abstract

The detection of biological molecules is a useful tool for diagnostics, research, and general health monitoring. By measuring concentrations of certain key components of biological samples, vital information can be gained as to the condition of the entire biological system. Diseases such as cancer can be detected by monitoring changes in concentrations of certain biomarkers for example. The more accessible and versatile biological sensing becomes, the more good it can do for more people. To this end, a biosensor system has been designed with a focus on simplicity, low cost, versatility, and accessibility. The system consists of a portable impedance sensor, microfabricated interdigitated gold electrodes, and modified gold nanoparticles.

Detection of biological components using this sensor is based on electrical impedance changes in interdigitated electrodes caused by the binding of modified gold nanoparticles to those electrodes. Molecular recognition elements, such as antibodies or aptamers, bind specifically to target biomolecules and facilitate the binding of nanoparticles which change the measured impedance. Because this change does not depend on the biomolecule itself, the system is very versatile.

Several generations of interdigitated electrodes have been made over the course of this research. The electrical properties of different designs have been simulated, and processes in making electrodes have been refined to create smaller electrodes (reducing cost), with smaller dimensions (increasing sensor sensitivity). The newest generation of electrode chips used for testing consist of eight gold electrode pairs with interlocking digits on silicon dioxide substrates. The surfaces of the electrodes can be modified with molecular recognition elements for detecting specific metabolites.

Methods have been developed for modifying the surface of the electrode chips with molecular recognition elements (such as antibodies) as well as modifying gold nanoparticles with similar molecules. Tests have been completed on direct chemical bonding of gold nanoparticles onto electrodes and measuring the resulting impedance change. Using antibodies, proteins have been detected (using a secondary antibody to bind gold nanoparticles) at concentrations that have been found to be relevant for clinical diagnosis. Work is continuing focusing on quantitative detection of metabolites and other biomarkers.

The impedance sensor circuit is an Arduino-based system on a printed circuit board with Bluetooth connectivity. The device connects to the sensor electrodes, and is controlled using a smartphone app. The app controls the settings for impedance measurement, calculates values and interprets incoming data, and displays and saves the resulting data. The circuit is capable of measuring impedances over a range of frequencies (1 kHz to1 MHz), and can track changes in impedance over time. The results from the circuit are comparable to much larger and more expensive systems (within ±2% error). The circuit is handheld and has a total cost (without a smartphone) of around $60 (compared to $15000 for more complex tabletop electrochemical stations).

Acknowledgments

I would like to acknowledge funding provided by NSERC, Alberta Innovates Technology Futures (AITF), and the CRIO grant. Without this funding, very little of this research could have been possible. I would also like to of course acknowledge Dr. Jie Chen, who allowed me the freedom and resources to do this research, Dr. David Wishart, head of the CRIO Tricorder Program and the reason I can do research based on technology from Star Trek, and other professors involved with the CRIO program, like Dr. John Davis and Dr. Wayne Heibert. I have also worked with, and depended upon numerous research assistants, graduate students, undergraduate students, post docs, and high school students. Peter Hermanson, Ryan Coupz, Gaser Abdelrasoul, Donghai Lin, Marcus Tamura, Ian Prescott, Ben Flanders, Nikola Pekas, Shiang Qi, Xiaojian Yu, Rudransh Kumar, Kathleen Ismond, Xiaoyan Yang, and Yollanda Hao just to name a few of the people I worked with and relied upon. I will of course be naming names through the course of this document to acknowledge specific contributions.

Through the course of my research I have personally worked with people from all over the world, including China, Iran, Egypt, Saudi Arabia, India, Ukraine, Turkey, Canada, the U.S., and others. I feel I am a better researcher, and a better person because of it.

Table of Contents

List of Tables

List of Figures

List of Abbreviations

ADC	Analog-Digital Converter
AFM	Atomic Force Microscope
APTES	(3-Aminopropyl)triethoxysilane
DNA	Deoxyribonucleic Acid
EDC	N-(3-Dimentylaminopropyl)-N′-ethylcarbodiimide
EIS	Electrochemical Impedance Spectroscopy
ELISA	Enzyme-Linked Immunosorbent Assay
FTIR	Fourier Transform Infrared Spectroscopy
GNP	Gold Nanoparticle
IDE	Interdigitated Electrodes
I-FABP	Intestinal Fatty-acid Binding Protein
MRE	Molecular Recognition Element
NHS	N-Hydroxysuccinimide
NMR	Nuclear Magnetic Resonance
PBS	Phosphate Buffered Saline
PDMS	Polydimethylsiloxane
PEG	Polyethylene glycol
POC	Point-of-Care
RNA	Ribonucleic Acid
RT-CES	Real Time Cell Electronic Sensing
SERS	Surface-Enhanced Raman Spectroscopy
SPR	Surface Plasmon Resonance
ssDNA	Single Stranded Deoxyribonucleic Acid
ssRNA	Single Stranded Ribonucleic Acid
TCEP	Tris(2-carboxyethyl)phosphine

TEM	Transmission Electron Microscope
THF	Tetrahydrofolic Acid
TSC	Trisodium Citrate Dihydrate
V/V	Volume by volume concentration
XPS	X-ray photoelectron Spectroscopy

Chapter 1 : Introduction

Medical point-of-care (POC) testing is an increasingly popular field of research [1]–[3]. Transitioning medical testing out of labs and onto portable devices has numerous potential benefits including reduced cost, faster detection times, and increased accessibility to tests [4]. By integrating existing medical diagnostic techniques (or new approaches to achieve the same goals) into more compact forms and automating testing processes, devices can be created that complete complex testing and analysis on biological samples and systems directly at or near patients being tested (thus point-of-care testing) [5]. Lab-on-chip technologies, microfluidics, and biosensing techniques are all being utilized to this end [6].

One widely used example of POC testing technology is glucose sensors. These portable biosensors are commonly used by individuals with diabetes to monitor their blood glucose levels so they can manage their conditions. Thanks to the POC nature of the device, testing can be done quickly and affordably enough to get an accurate accounting of blood glucose levels at a precise time, when needed, something that would be impossible if blood samples had to be sent away for testing. Testing convenience is not the only advantage of POC devices. The increased affordability and portability of such devices make them ideal for deployment in low-resource areas like developing countries, and remote locations [3], [4], [7]. Without practical access to large scale medical facilities combined with increased disease risks in remote areas, the use of POC devices can have a significant impact.

1.1. Biosensors

Glucose sensors used for monitoring the blood glucose levels of diabetics is a prime example of a biosensor. In the most general sense, a biosensor is a device which can measure the biological activity or content of a biological organism, or set biological sample. More specifically, molecular biosensors can detect the presence of a target biomolecule or species of interest in a biological sample. Even for this more specific class of biosensor, the open-ended nature of what constitutes a molecular biosensor leads to a multitude of different implementations, each with

advantages and disadvantages [8]. The best way to differentiate these different biosensors is by characterizing the way they recognize biomolecules, and how they detect and report them.

1.1.1. Recognition elements

The recognition element of a biosensor (one of two characteristic components of biosensors, the other being the detection element) is the active component which recognizes the biomolecule or biomolecules of interest. Non-specific binding involves species in a biological sample adhering to a sensing element indiscriminately, then using an external detection technique to distinguish what molecules are present. Examples of this type of recognition include mass spectroscopy, gas chromatography and infrared spectrum analysis [9]–[11]. While these techniques can be very versatile and generally simplify recognition (the only requirement being that samples be present on the sensor), detection can be a complicated process involving interpretation of results based on properties of the sample (e.g. known IR spectroscopy peaks). This process becomes even more difficult for complex samples containing many different components.

The other major form of recognition element employed by biosensors, specific recognition, relies on chemical or biological molecular recognition elements (MREs) to bind to or react with a specifically intended biomolecule of interest. The above-mentioned example of glucose sensors use a catalyst, glucose oxidase, to catalyze a redox reaction with glucose in a blood sample [12]. In this way, the detection of glucose is dependent on the recognition element, the catalyst, and that recognition allows for detection. Rather than design completely new elements to bind to and recognize biomolecules, it is far more common to simply “steal from nature” and utilize existing naturally occurring recognition elements in biosensor design. The human immune system already has an intricate system for recognizing the presence of biomolecules in the form of antibodies. As a function of the immune system, antibodies bind to antigens, marking them for destruction by immune cells. Biosensor design can leverage this specific binding mechanism to capture analytes in a biological sample. Antibodies can be chemically bound to surfaces on sensing components such as electrodes or mass sensing cantilevers [13]–[15] or can be used in solution [16]. This type of recognition element isn’t limited to antibodies. Membrane proteins found in bacteria also have specific binding properties [17] and single stranded DNA or RNA can be used to detect the presence of complementary strands [18].

Besides recognition of existing sequences, DNA and RNA can also be utilized as "designer" recognition elements in the form of aptamers. Like other DNA machinery (such as the DNA tweezer [19]), the specific function of aptamers is determined by the 3D shape of the DNA, which is in turn is determined by the base sequence of the DNA. Given the right conditions, single stranded DNA (ssDNA) or RNA (ssRNA) folds in on itself, with its own bases interacting with each other, forming base pairs, causing bends, turns and an emergent general 3D structure. For aptamers, these structures are refined to a point where the structure forms binding sites which can bind strongly and specifically to targets. The designed targets for aptamers can vary widely from large organic molecules to small inorganic targets. This versatility makes them ideal for biosensor applications for detecting multiple and exotic analytes. In general aptamers are hardier than antibodies in terms of temperature and environment [20], [21]. There can be some disadvantages with aptamers compared to antibodies too, as they need the proper conditions to form the right structure for binding, and they are sensitive to nucleic acid breaking enzymes (especially for RNA aptamers) which are readily found in biological fluids [22].

1.1.2. Detection Elements

Once an analyte is recognized through specific binding or a chemical reaction, this recognition needs to be detected and reported by the biosensor. There are multiple ways to measure the detection endpoint of binding between the analyte and detection element. One significant example of this is mass-based detection. This type of detection relies on the added mass of bound analytes, causing damping on oscillating quartz [23], or measurable deflections on cantilevers [24], [25]. This technique can be very sensitive and only relies on specific binding and analyte mass (not other specific chemical or physical properties). However, confounding sources of signal may exist in the detection environment and there is added complexity from the need to measure the deflections caused by the analytes. Another significant class of detection methods is optical detection where the presence of the target biomolecule causes a change that can be detected optically. This category encompasses multiple mechanisms, ranging from relatively simple, like aggregation of MRE tagged nanoparticles causing a colour change [26]–[28], to more complex systems relying on surface enhanced Ramen spectroscopy (SERS) [29], [30].

Electrical detection methods are employed by many biosensor designs (including the one described here) and they generally offer simple, quick, and accurate detection. Generally, electrical

detection relies on sensing changes in the electrical properties of a system caused by the presence of a designed biological target. Changes can come in the form of added current from catalyzed reactions or redox reactions, or changes in conductivity or capacitance caused by the presence of the target or signal enhancing labels. Glucose biosensors for monitoring diabetes use catalyzed reactions detected electrically [31], [32]. Ion concentrations in blood or urine along with charged molecules can be detected due to their ability to change the conductivity of a fluid [33]. The growth and number of cells in a sample can even be determined by their electrical impedance when grown on electrodes [34].

1.2. The Tricorder Project

The main drive of the research presented in this thesis is the design and creation of a versatile, handheld, impedance-based biosensor system for the detection of metabolites and other biomolecules for applications in personal health monitoring, rapid diagnostics by medical personnel in off-site locations, environmental monitoring, as well as in many other applications. Point-of-care diagnostic devices offer superior accessibility over traditional lab based techniques [35], [36]. The genesis of this project was as part of the Metabolomic Tricorder Project (www.tricorder.ca); a NINT/University of Alberta project funded by the CRIO program (the Collaborative Research and Innovation Opportunities program from Alberta Innovates Health Solutions) and comprised of a number of research groups in areas spanning from engineering, sciences, physics, computer science, chemistry, organic chemistry, nanofabrication, microfluidics, biology, and medicine. Like its *Star Trek* namesake, one goal of the Metabolomic Tricorder Project is to create a portable biosensor system capable of quickly and accurately detecting multiple conditions and monitoring general health.

The way that this proposed system can detect multiple conditions and monitor general health is in the "metabolomic" part of the title. Like other "-omics" (genomics, proteomics, etc.) metabolomics concerns itself with building a database of biological information to obtain a complete phenotypic assessment of an entire biological organism or process. In this case, instead of individual genes coding for an entire organism, metabolomics tracks the metabolic products of cells and biological processes, called metabolites [37]. And while genes and proteins do determine the state of an organism (genes coding for physical traits for example), these are far removed from the day to day condition of that organism. Concentrations of metabolites change in response to

environmental stressors and gauge the direct condition and function of the organism in the moment. Therefore, information gathered on what metabolites are present and in what concentrations can reveal a great deal of information about the current condition of an organism or biological system. For example, metabolomics can be used to predict the likelihood of developing certain types of cancer [38].

One challenge in developing a biosensor system to accommodate the detection of a wide range of different metabolites is just how radically different each metabolite can be. With genetics or proteomics, the building blocks are all generally the same (nucleotides and amino acids, respectively), but metabolites run the gamut from small molecules to large complex structures like hormones and amino acids. The following table outlines the full list of metabolites originally proposed for detection in the Tricorder project along with normal concentration ranges for these metabolites in blood and urine. These metabolites vary widely in their sizes, chemical properties and natures, and their concentration ranges. The purpose of showing this information is to display the necessity for a "universal" biosensor system; a single system that could detect multiple metabolites in a single biological sample, despite the different qualities and concentrations of those metabolites. One important note is that the goal of the research presented in this thesis is not to create a biosensor that detects each of these metabolites, but rather a detection system and measurement platform that could. Once a truly versatile system has been developed, it can allow for developing tests for these specific metabolites.

Table 1.1: List of Metabolites to be Detected by the Tricorder Project

Metabolite	**Normal Concentration in Blood (μM)**	**Normal Concentration in Urine (μmol/mmol creatinine)[1]**
Asymmetric Dimethylarginine (ADMA)	0.41 - 0.79	2.50 - 3.34
Aldosterone	0.000008 - 0.000044	0.006 - 0.014
Aminoadipic acid	0.0 - 5.0	3.4 - 11.2
Beta-Hydroxybutyrate	40 - 80	23.6 - 41.0

[1] Here, metabolite concentrations in urine are normalized against creatinine. This provides a standard as the concentration of urine can vary with hydration.

Metabolite	Normal Concentration in Blood (μM)	Normal Concentration in Urine (μmol/mmol creatinine)[1]
Betaine	20.0 - 144.0	6.4 - 92.7
Billirubin	5.0 - 21.0	0.0019 - 0.21
Carnosine	5.54 - 7.54	0.8 - 6.2
Choline	8.7 - 12.5	1.4 - 6.1
Creatinine	50.0 - 80.0	800 - 1100
Estradiol	0.0 - 0.00018 (male)	0.00034 - 0.00084 (female)
Folate	0.011 - 0.036	0.000013 - 0.0026
Formate	23.9 - 219.5	8.55 - 32.23
Glucose	4070 - 4810	11.98 - 39.62
Glutamate	44.0 - 76.0	3.3 - 18.4
Glutamine	581 - 709	9.0 - 33.0
Glycerol	34.0 - 52.0	0.12 - 0.73
Homocysteine	7.0 - 11.0	0.48 - 3.42
HPHPA	(unknown)	0.00 - 90.0
Indoxylsulfate	9.8 - 18.2	14.48 - 25.0
Lactate	600 - 2300	0.0 - 0.25
Leucine	127.0 - 187.0	1.5 - 4.5
Neopterin	0.0109 - 0.0191	0.13 - 0.29
Phenylalanine	56.0 - 74.0	2.63 - 6.37
Pyruvate	38.0 - 88.0	0.54 - 8.67
Taurine	102.0 - 222.0	21.1 - 105.0
Testosterone	0.009 - 0.03472 (male) 0.00052 - 0.00243 (female)	0.88 - 1.26 (male) 0.0000 - 0.0002 (female)
TMAO	17.4 - 58.2	0.00 - 151.0
Tyrosine	57.0 - 87.0	4.3 - 13.3
Uric Acid	242.0 - 362.0	119.0 - 294.0

Metabolite	Normal Concentration in Blood (μM)	Normal Concentration in Urine (μmol/mmol creatinine)[1]
Vitamin D	0.063 - 0.221	0

As mentioned previously, the Tricorder project is an interdisciplinary group effort comprised of many labs in many fields working together. This collaborative effort includes chemists and biologists for modifying metabolites and preparing molecular recognition elements for the sensor, as well as engineers and physicists for designing sensors. To accommodate the scope of the project and cover the widest range of potential metabolites and applications, several different sensor designs are part of this project including SERS based detection methods, mass based detection methods and electrical impedance sensor designs. The research described here in this thesis involves the design and testing of a portable electrical impedance based biosensor design which is one aspect of the Tricorder project.

1.3. Biosensor Overview

The biosensor system designed through this research is an impedance-based sensor which uses interdigitated electrodes and gold nanoparticle signal enhancement. The details of the design process, detection principles, and device testing are described in later chapters. Essentially, the biosensor is based on measuring changes in the impedance of interdigitated electrodes (IDEs) caused by the binding of gold nanoparticles (GNPs) on their surface.

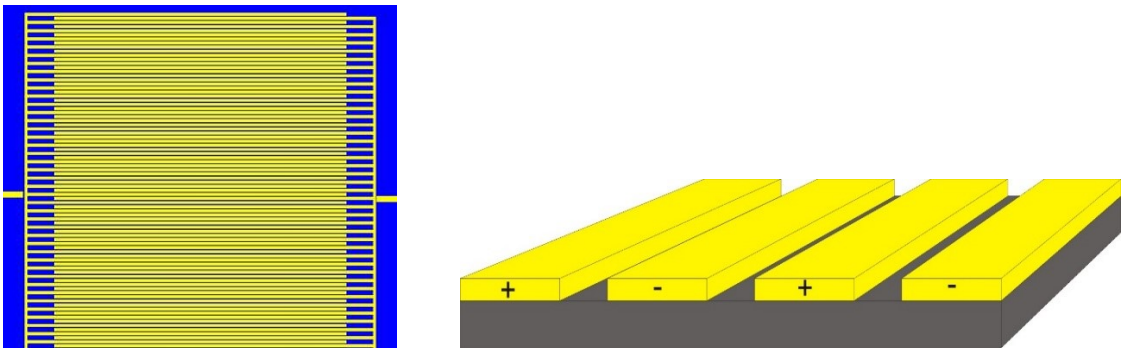

Figure 1.1: Left: The basic structure of the electrodes used in this biosensor design. There are two comb-like electrodes which overlap, but do not touch. Right: a zoomed-in 3D visualization of adjacent electrode digits (not to scale).

The surface of the IDEs is chemically modified with MREs which bind to a biomolecule of interest in a biological sample (blood, urine, etc.). This binding facilitates the binding of modified GNPs, either through the use of a secondary MRE, or other various methods. The presence of the nanoparticles on the surface changes the electrical characteristics of the system. The electrical impedance of the electrodes is measured before and after binding. The change in the impedance relates directly to the number of bound nanoparticles, which relates directly to the concentration of the target biomolecule. The exact detection principle, particulars of electrode design, details on chemical modifications, impedance measurements, and testing are described in detail through the rest of this thesis.

1.4. Non-Faradaic Biosensors

The best classification for the designed biosensor is a non-faradaic electrical sensor. Electrical biosensors can be generally classified as either faradaic or non-faradaic [39]. Faradaic biosensors rely on electrochemical reactions on electrodes to create a detectable signal. There are many examples of faradaic sensors that use various reactions [40], [41], or electrochemically active redox labels [42]–[45] for detection. Non-faradaic sensors do not rely on electrochemical reactions, but rather measure changes in the electrical properties of electrodes based on small-signal electrochemical measurements caused by interactions with target biomolecules. While faradaic sensors can be more sensitive than non-faradaic, they are also more complicated, requiring a reference electrode and specific electrochemical reactions [46].

To understand the various ways non-faradaic sensors can affect the electrical properties of an electrode, an equivalent circuit model of a two-electrode system can be investigated. The biosensor designed in this research is also a two-electrode system, but for the sake of simplicity, a single pair of electrode digits (two adjacent digits, one from each electrode) will be considered.

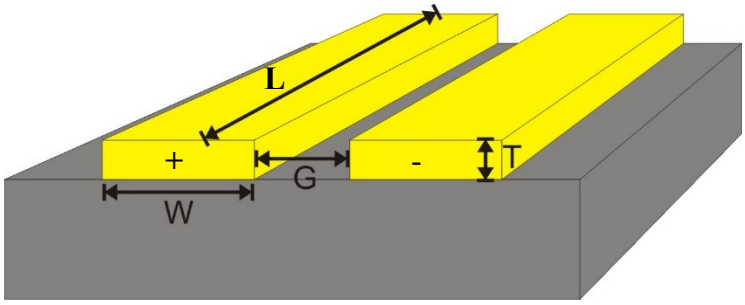

Figure 1.2: Basic setup of a two-electrode sensor system with the various geometric dimensions labeled. This can represent an entire system, or two adjacent digits of an IDE.

One basic equivalent circuit for such a two-electrode system is shown in Figure 1.3. This combination of resistors and capacitors is a representation of both the physical geometry of the two electrodes and the result of the buffer solution around it [39], [47]. The top capacitor, C_g, is the geometric capacitance of the electrode itself, determined by the dimensions of the electrodes (thickness, gap between them, etc.) and the dielectric of the surrounding solution. The two capacitances, C_{dl}, are the double layer capacitances of the two electrodes. Double layer capacitances are caused by the charged ions in the buffer solution and the surface charge on the electrodes. They interact to form a separated layer of charges that act as capacitors surrounding the electrodes (more on double layers in Chapter 3). The final component in this equivalent circuit, R_s, is the resistance of the buffer solution between the two electrodes. This obviously changes based on the buffer solution, with higher ionic concentrations leading to higher conductivity, and a lower resistance. This is also dependant on the space filled by the buffer, so it depends also on the length of the electrodes and the size of the gap between them.

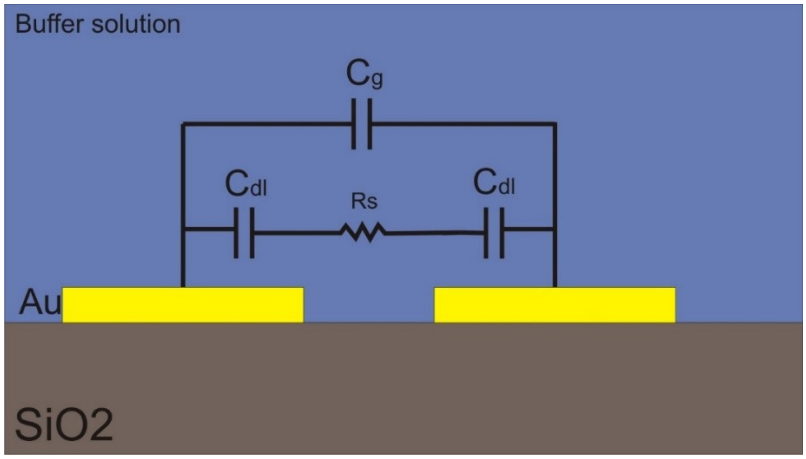

Figure 1.3: Basic equivalent circuit for a two-electrode sensor submerged in a buffer solution.

This is of course just one of many possible equivalent circuits for this system. More complex circuits, which include charge transfer resistances, and Warburg impedances (caused by the diffusion of species in the solution) [48], [49] can also be considered. However, these components can be ignored for non-faradaic applications as there are no redox reactions or charge transfer to the electrodes. One factor that is ignored here but could be present is parasitic impedance. This is caused by the resistivity and capacitance of the substrate the electrodes are on. While parasitic impedances are not considered in this initial circuit analysis or the electrode simulations presented in chapter 3, it is an important aspect to remember for interpreting and explaining measurements on actual electrodes and how they differ from the ideal case.

From the equivalent circuit, the total impedance of the two-electrode sensor is:

$$Z_{tot} = \left(R_s + \frac{2}{j\omega C_{dl}}\right) \parallel \frac{1}{j\omega C_g} \tag{1.1}$$

In this equation, in addition to the previously defined parameters in the equivalent circuit, Z_{tot} is the total electrical impedance, ω is the angular frequency, and j is the imaginary number. This impedance leads to the general frequency response shown in Figure 1.4, with three distinct areas of impedance magnitude and a parabolic phase. The three sections are divided by two cut off frequencies, f_L and f_H. The first section, between 0 Hz and f_L, has linearly decreasing impedance magnitude. This section is dominated by the double layer capacitance around the electrodes [39]. The lower cut off frequency is defined by:

$$f_L = \frac{1}{\pi R_s C_{dl}} \tag{1.2}$$

The second section, between f_L and f_H, is dominated by the resistance of the solution, R_S, and thus is constant and not frequency dependant, leading to a flat section in the impedance magnitude graph. The peak of the phase is also in this frequency range. The third section, defined by frequencies above f_H, is dominated by the geometric capacitance of the electrodes. The higher cut off frequency is defined by:

$$f_H = \frac{1}{2\pi R_s C_g} \tag{1.3}$$

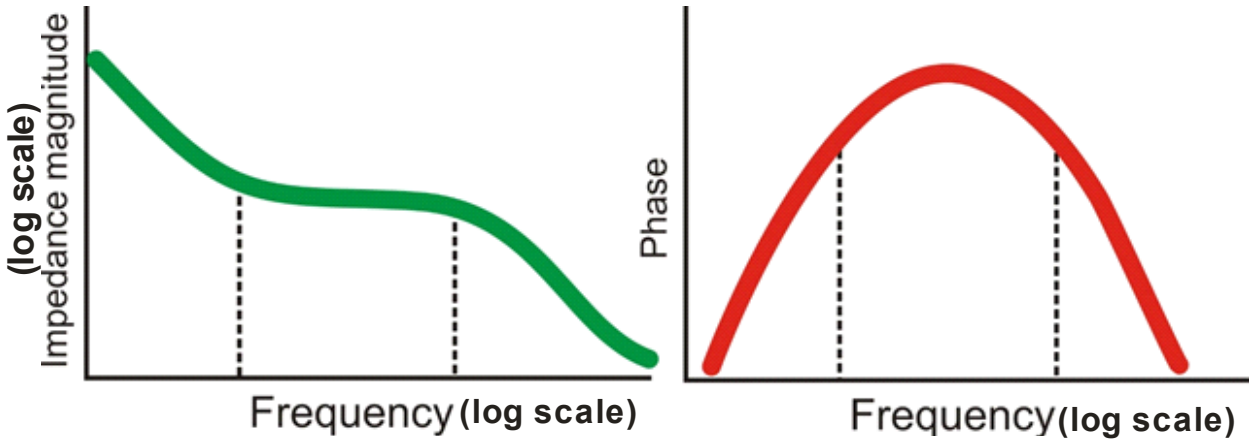

Figure 1.4: General impedance magnitude and phase shapes for the two-electrode sensor equivalent circuit.

The main principle behind any non-faradaic sensor is to manipulate or modify one of these aspects of the equivalent circuit. Depending on the part being modified, the resulting change in impedance will reflect the modified section, resulting in a change in the corresponding frequency section. Some sensor designs bind analytes directly to the electrode surfaces, and the interaction of the bound molecules on the electrode surface disrupts and changes the capacitance of the double layer [50]. Other systems, such as ones which detect attached cells or bacteria [51], bind targets between electrodes, and depending on the properties of the targets, change either the resistivity between the electrodes, or the dielectric properties between electrodes, changing the geometric

capacitance. Therefore, depending on the detection method used, one or more of the three frequency regions of the impedance can be changed.

1.5. Biosensor Detection Using GNPs.

As stated previously, the biosensor designed in this thesis is non-faradaic and uses bound GNPs to affect the impedance of the electrodes to cause measurable detection. However, there is more than one way to accomplish this. During the course of this research, two primary methods were investigated: one with GNPs bound directly to the electrode digits, and the other with GNPs bound to the gaps between electrode digits.

1.5.1. GNPs Bound to Electrode Digits

The first method investigated for detection was binding GNPs directly onto the electrode digits. With this method, the metal surfaces of the electrode digits are modified with MREs to bind target biomolecules and GNPs for detection amplification.

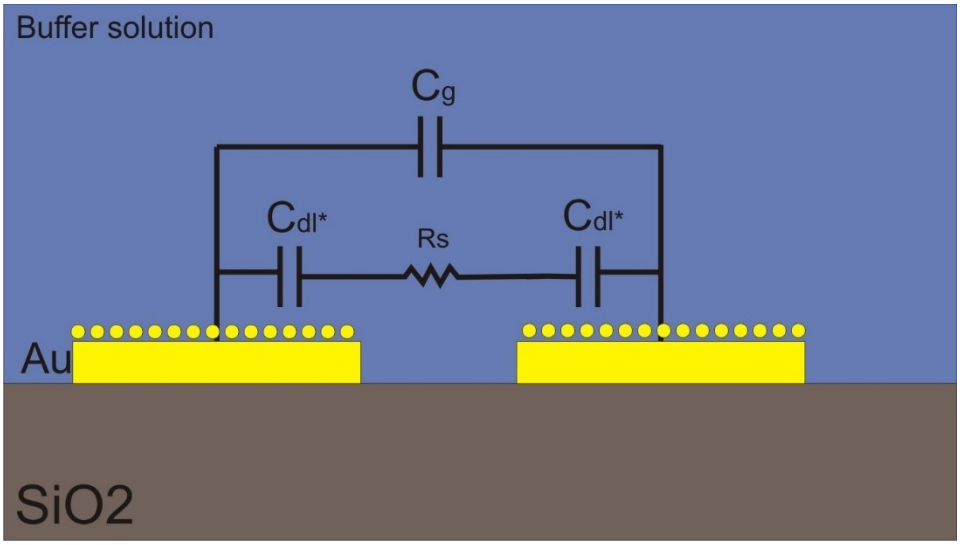

Figure 1.5: Electrode layout and new equivalent circuit with GNPs bound to the electrode digits.

With this method, the primary effect caused by the GNPs is to the double layer capacitance. GNPs bound to the electrode digits disrupts the formation of the double layer around the electrodes, thus changing the double layer capacitance.

1.5.2. GNPs Bound Between Electrode Digits

The second method that was investigated was binding GNPs directly between electrode digits, with molecular recognition elements (MREs) bound to the silicon dioxide substrate. In this case, the GNPs affect the impedance between electrode digits, introducing their own resistivity and double layer capacitances to the gaps [52] (labeled Z in Figure 1.6).

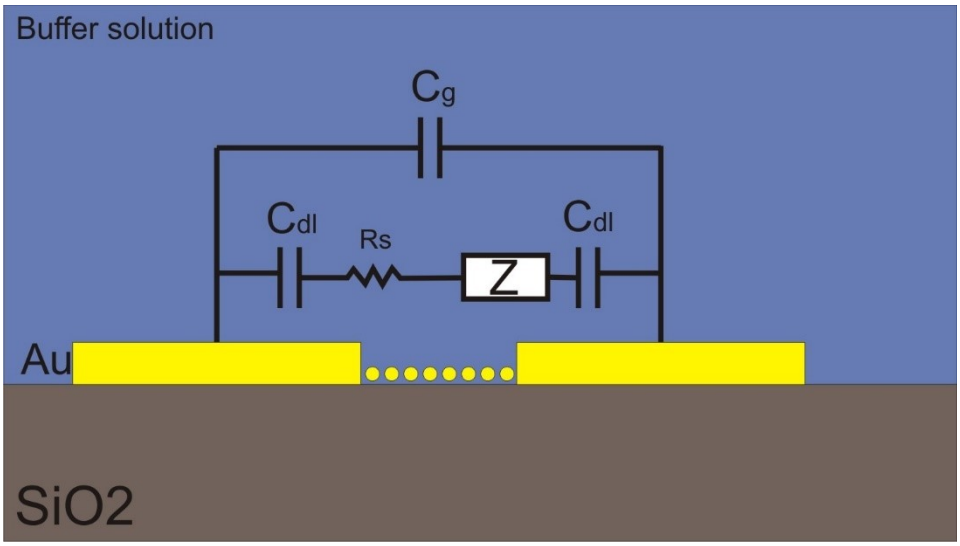

Figure 1.6: Electrode layout and new equivalent circuit with GNPs bound between electrode digits.

1.6. Goals

The primary goal of this thesis research is to create a versatile, portable, inexpensive, easy-to-use, biosensor platform for detecting multiple biomarkers and metabolites. At the outset of the project, the initial goal was to create a portable system that could measure a combination of the metabolites shown in Table 1.1. Since then the scope of the research in some ways narrowed and widened in other ways. The specific goal became focused not on detecting specific metabolites or biomarkers, but rather developing the techniques and tools to do so in an inexpensive, portable system for a much wider array of applications than just metabolite sensing. This understandably involves research and experimentation crossing many different disciplines including chemistry, biochemistry, microfabrication and design, and circuit design among others.

More specifically, the goals for this research include: proving the detection concept, designing interdigitated electrodes for the system, developing and refining surface modification for the electrodes and signal enhancing nanoparticles, binding gold nanoparticles to electrodes and

measuring the resulting change in electrical impedance, and developing sensor hardware including impedance measuring circuitry.

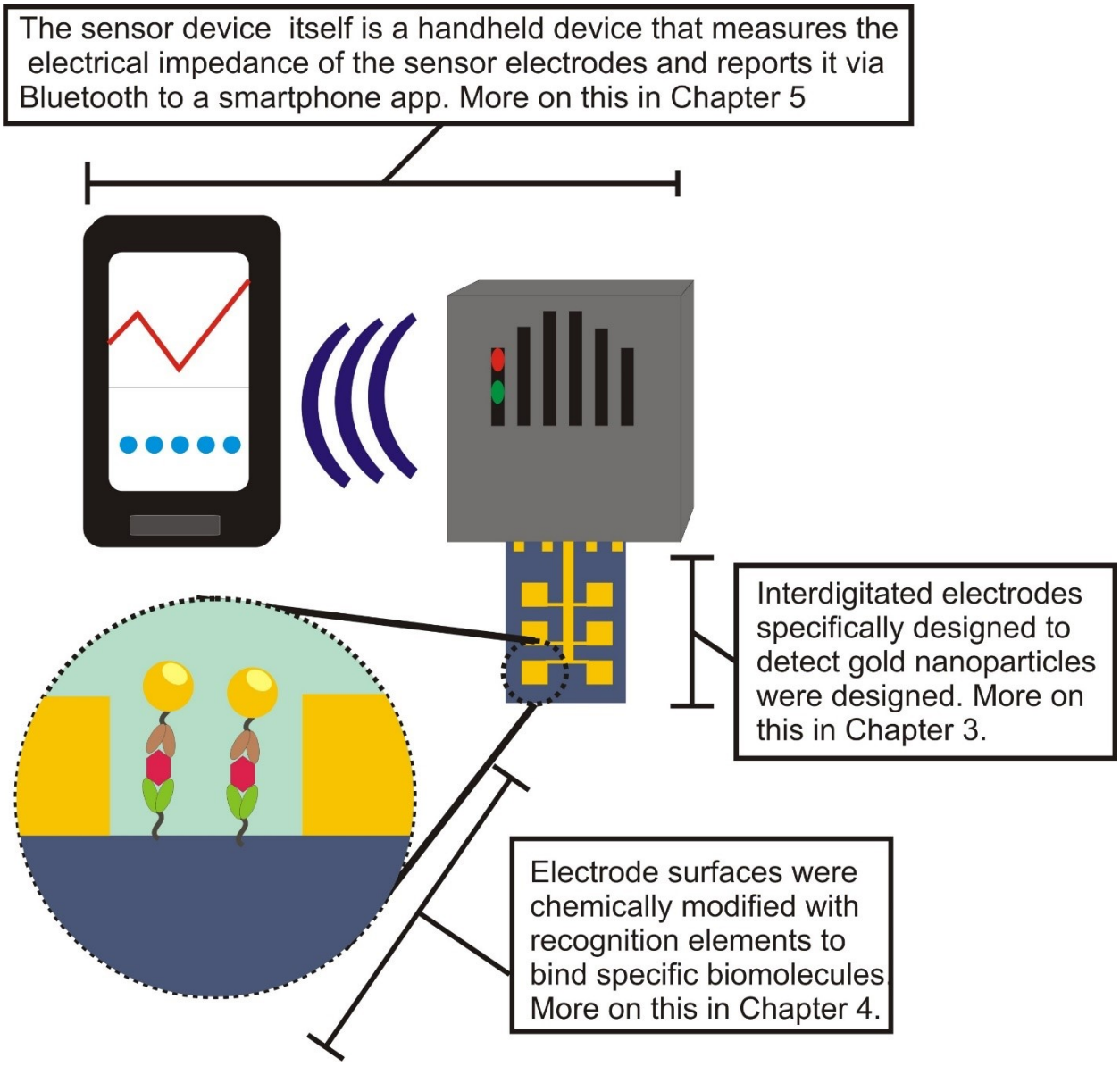

Figure 1.7: General overview of the entire biosensor system. The handheld impedance sensing device monitors the electrical impedance of gold interdigitated electrodes on the electrode chip (top right). The results are sent via Bluetooth to a smartphone app (top left).

1.7. Thesis Outline

This thesis is organized in such a way as to show the design process in creating this biosensor device, from its conceptual origins, to designing the various necessary components to bringing these all together in a single device, and the many iterations of these along the way. An overview of the different components of this device (and subsequently the research that designed it) is shown in Figure 1.7. Chapter 2 describes original basis for the overall design, early proof-of-concept results and simulations, and the overall design strategy employed for the biosensor system. Chapter 3 covers the design of the electrodes used with the biosensor. This includes the rationale behind the various designs, simulations used to determine optimal electrode parameters, and the fabrication processes. Chapter 4 delves into the chemistry involved in the biosensor design. This includes the gold nanoparticles used, chemical modifications to nanoparticles and molecular recognition elements, and modifying and binding elements to the biosensor electrodes. Chapter 5 outlines the actual device and circuitry design, from early concept stages to an inexpensive, handheld circuit board for measuring electrode impedance. Finally, Chapter 6 covers ongoing and future work, including fluidics for transporting biofluids and buffers over the electrodes for measurements, and ongoing testing for multiple applications.

Chapter 2 : Proof of Concept

2.1. Introduction

With the goal established by the Tricorder project of making a portable, inexpensive biosensor for detecting multiple metabolites, the first step was to decide on the detection approach. While optical approaches, such as surface plasmon resonance (SPR) for detection, can be effective and accurate, they also involve large and expensive equipment for detection. Instead, an impedance-based approach was chosen as the components required can be made relatively inexpensively and compactly. Even narrowing down this design decision, there are still many different approaches to take with impedance-based detection. These range from basic capacitive measurements [53], [54] and changes in conductivity with basic electrodes [55], all the way up to more complex systems with multi-probe electrodes [56] and involved data processing of ranges of electrochemical impedance spectroscopy (EIS) data [57].

Inspiration for the way to approach impedance-based detection with this design came in the form of the RT-CES cell counting system (made by ACEA Biosciences Inc. San Diego, US), also known as the “Real Time Cell Electric Sensing system”. This device monitors the growth of cells as they are cultured on specially designed electrodes. These electrodes are essentially interdigitated capacitors made of gold patterned on glass. When an AC voltage is applied to the electrodes, an electric field forms between adjacent digits (as it should in any capacitor) and the resulting impedance is measured based on the capacitance and conductivity of the space between the digits. As cells grow on the electrodes, they disrupt the electric field between the electrode digits, changing the measured electrical impedance. More cells equates to a larger change in impedance, so by measuring the impedance over time, the number of cells can be tracked. The design of the metabolomics biosensor borrowed this same concept. If disruptions of the electric field in interdigitated electrodes caused by cells can result in a measurable impedance change, then perhaps the same could be true for metabolites bound to the surface using molecular recognition elements. The first big challenge with doing this is metabolites are not cells. They are significantly smaller. They do not naturally stick to surfaces. They do not significantly disrupt electric fields. These disparities have to be addressed in order to implement this application to a metabolomic biosensor.

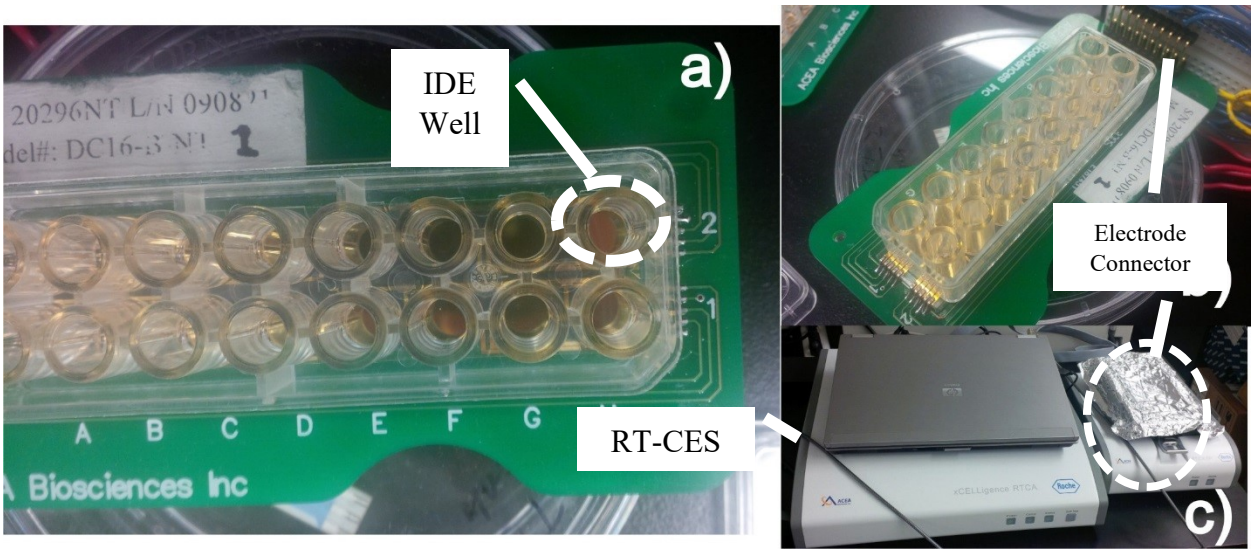

Figure 2.1: a) and b) The 16 well e-plate that is used with the RT-CES device. Each well contains a gold interdigitated electrode specially treated for cell growth. c) The RT-CES device itself. It is a tabletop device with a separate unit for the e-plate (which can be put in an incubator for cell growth). The separate unit (labeled "electrode connector") connects to the e-plate to measure each electrode's impedance. An external laptop is used to control the system and to record measurements.

Firstly, to detect metabolites there needs to be a way for the metabolites to interact with the sensor electrodes. Unlike cells which can grow and naturally stick to the electrode surface, methods needed to be designed to attach metabolites to electrodes. Additionally, it is not enough to just make the electrodes "sticky", but rather there needs to be specific binding that captures only the target metabolite in the tested sample while leaving out other components. There are several well established ways to accomplish this. The term "molecular recognition element" (MRE) refers to elements which bind to specific molecules. They can be incredibly diverse and can include single-stranded DNA made to bind to their complement [18], to more complex structures like binding proteins, which facilitate transport of molecules in cells [17], to antibodies which bind to specific antigens as part of the immune system [13], to aptamers which are specifically designed to bind to particular molecules [21], [58], [59]. All of these could potentially be used to bind metabolites, given that an MRE which binds that specific metabolite can be found or made.

Just because specific, targeted biomolecules can be bound to the RT-CES electrodes, it does not necessarily mean that the system can detect them. As an impedance-based measuring

system, any change to the electrode surface must cause a change in the impedance of the electrode that is significant enough to be measured. There are several factors which can influence this. First, the impedance measurement equipment itself must be sensitive enough to detect small enough changes in electrical impedance, as well as measure impedance at the optimal electrical frequency or frequencies, which can vary depending on the electrodes and type of detection [57], [60]. Second, the electrode dimensions can have a major impact on their sensitivity and suitability for detecting bound materials. Third, the nature of the bound material, which would include anything that would influence the impedance (or electric field) of the electrodes. This can include the size of the bound material and the electrical properties like conductivity, capacitance, or charge. In the case of the RT-CES setup that was used for proof-of-concept testing, most of these factors were fixed. The measurement equipment is very much a "black box", with set measurement ranges, input frequencies, and even proprietary output units, which perform post-processing on measured impedance to reflect cell growth, with no access to raw measured impedance values. While, at this early stage, these factors were out of direct control, what could be controlled is what was bound to the electrodes. Obviously, this system was designed with measuring cell growth in mind, and also obviously, cells are much larger, and therefore have a much large impact on an electrode's impedance, than biomolecules. However, in addition to bound biomolecules, a setup could be designed to additionally bind signal enhancing materials along with the biomolecules which would have a much larger impact on the impedance of the electrodes. In this case, signal enhancing gold nanoparticles were chosen that could bind to the electrodes along with the target biomolecules. Gold nanoparticles are widely used in biomedical applications and research [26], [61]–[69]. They are favored for their stability, low reactivity, biocompatibility [70], and the many options available for modification [69]. Gold easily makes strong thiol bonds, meaning that thiol-linkers and thiol-modified tags, like MREs or biomolecules, can be covalently attached to gold nanoparticles [69], [71], [72].

2.2. Proof-of-Concept Experiments with the RT-CES Cell Counting System

2.2.1. DNA Bound Gold Nanoparticles

The RT-CES cell counting system was used for proof-of-concept experiments to test the viability of detecting the presence of gold nanoparticles, and, more importantly, small biomolecules on IDEs using electrical impedance measurements. In the first experiment, gold

nanoparticles were bound to the gold digits of the RT-CES electrode. This was accomplished using short complementary strands of DNA. Thiol-modified single stranded DNA (ssDNA) was purchased from Integrated DNA Technologies (www.idtdna.com):

Poly T: 5′ Thiol-CCCCCCCCCCTTTTTTTTTTTTTTTTTT 3′

Poly A: 5′Thiol-CCCCCCCCCCCCCCCCCCCCCCCCCCAAAAAAAAAAAAAAAAAA 3′

The first strand, named "Poly T" for its long sequence of thymine bases, has a thiol modifier at it 5' end, and a string of cysteine bases that act as a neutral spacer. "Poly A" is similar, but with a longer cysteine spacer and a chain of adenine. Thiol groups (HS-) contain sulfur, which readily bonds to gold, forming a thiol bond (Au-S-DNA) [69]. Taking advantage of this, DNA with attached thiol groups can easily be attached to the gold surfaces of the electrode, or to gold nanoparticles (for more information on this, refer to Chapter 4). For this experiment, Poly T strands were attached to the gold digits of the RT-CES electrodes, using tris(2-carboxyethyl)phosphine (TCEP), a reducing agent, to reduce the thiol group on the DNA to allow for the gold-sulfur bond to form. Next, 30 nm diameter gold nanoparticles (GNPs), purchased from Cytodiagnositcs (www.cytodiagnostics.com), were modified using the Poly A strands and stabilized with polyethylene glycol (PEG). The GNPs were citrate stabilized initially, suspended in a sodium citrate solution to keep GNPs from aggregating. However, the high ion content of this buffer interferes with impedance measurements, so it had to be removed and replaced with another buffer for measurements. PEG is a long polymer chain which surrounds nanoparticles and prevents them from aggregating together in solution. To create modified nanoparticles, an excess of Poly A, PEG, and TCEP were added to GNPs in solution. Like the electrode surface, the TCEP reduced the thiol modifier on the DNA (and the PEG) to facilitate binding with the gold of the nanoparticles. After binding, the excess unbound DNA and the citrate buffer were removed using centrifugation. The fully modified nanoparticles were resuspended in pH 8.0 phosphate buffered saline (PBS) for measurements using the RT-CES system.

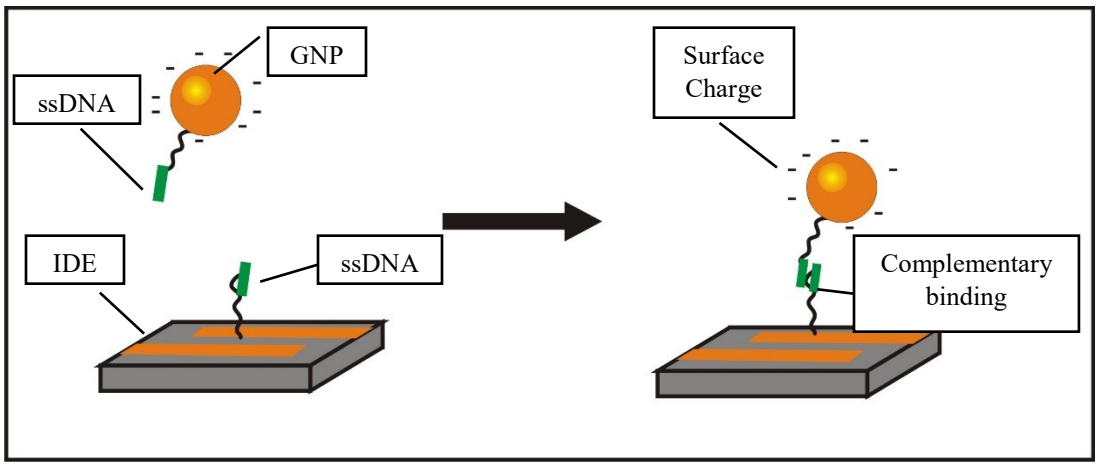

Figure 2.2: Experimental setup of the initial DNA binding experiment. DNA modified gold nanoparticles are attached via short complementary single stranded DNA onto interdigitated electrodes. The electrical impedance of the electrodes was measured using the RT-CES system before and after the addition of gold nanoparticles. A surface charge is added to nanoparticles to enhance detection.

Impedance measurements were taken using the RT-CES system by first measuring the impedance of DNA modified electrodes in PBS buffer (the same buffer the nanoparticles were suspended in) to establish a baseline value. Once this baseline was established, different concentrations of modified GNPs were added to the electrodes as the impedance was monitored by the system. Measurements were taken continuously until the new measurements stabilized. The solution on the electrodes was then removed to remove any unbound nanoparticles, and clean PBS buffer was added in its place. Measurements were taken again until stable and the final value was compared to the baseline for a relative impedance measurement.

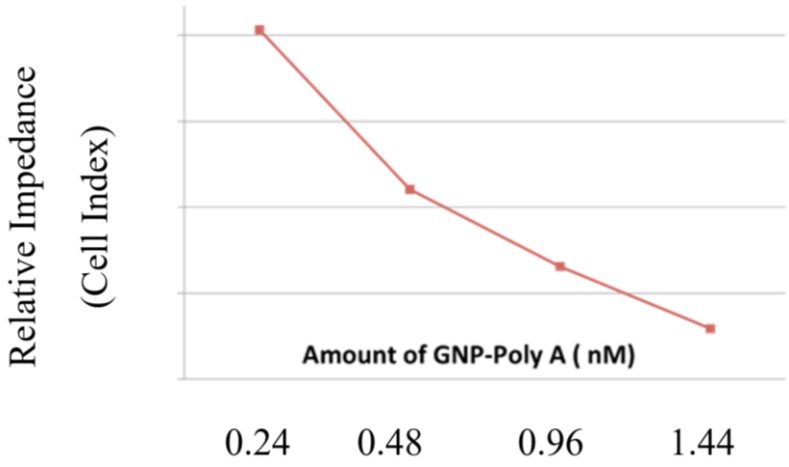

Figure 2.3: Results of the initial DNA-GNP RT-CES proof-of-concept experiment. Here the "relative impedance" refers to the calculated relative impedance reading from a change of the electrode modified with DNA without GNPs added and with GNPs. Here, "cell index" are the units given by the RT-CES system. This is a relative measure of impedance is normally used for cell counting (thus the name cell index), but is used here for GNP detection. As the amount of GNPs increases, there is a greater decrease in the relative impedance.

The results of this initial experiment show that there is not only a measurable change in impedance caused by bound gold nanoparticles on the interdigitated electrodes, but that the detection can also be quantitatively modeled. This means that the change in impedance measured by the RT-CES system is greater if more GNPs are present, which in an actual biosensor application would correlate to a larger number of analytes in a sample. (Note: these results, shown in Figure 2.3 are from very early proof of concept experiments performed in the lab, thus there is no available data for statistical analysis for this result)

2.2.2. Metabolite Assays

With this initial success as a basic proof-of-concept for the impedance-based biosensor design, the next experiments with the RT-CES system were designed to test for detection of certain metabolites. For these initial proof-of concept experiments, two representative metabolites were chosen: cysteine and tetrahydrofolic acid (THF). While these metabolites are not on the established CRIO program list (Table 1.1), they exhibit structural similarities to many of them with cysteine

being an amino acid and THF a small biomolecule. These metabolites also have well established and stable molecular recognition elements (MREs) in the form of a common antibody that binds to cysteine and a DNA aptamer that binds to THF [73].

The basis of detection with this system, regardless of metabolite, is in the change in impedance caused by adding or removing gold nanoparticles from the electrodes. Therefore, there are many possible ways that metabolite detection can be done. For these proof-of-concept experiments, competitive assays were chosen as the best method for detecting metabolites. In a competitive assay, simply put, metabolites and modified GNPs actively compete for available binding sites. Nanoparticles are modified by directly attaching metabolites, which in turn can bind with the MREs bound to the electrode. However, due to the (relatively) large bound nanoparticle, the binding between the attached metabolite and MRE is weakened. Therefore, free metabolites have a higher binding affinity for the MRE than the bound metabolites and free metabolites can "outcompete" and displace the nanoparticles from the electrode, thus changing the impedance. (more information on the binding chemistry can be found in Chapter 4)

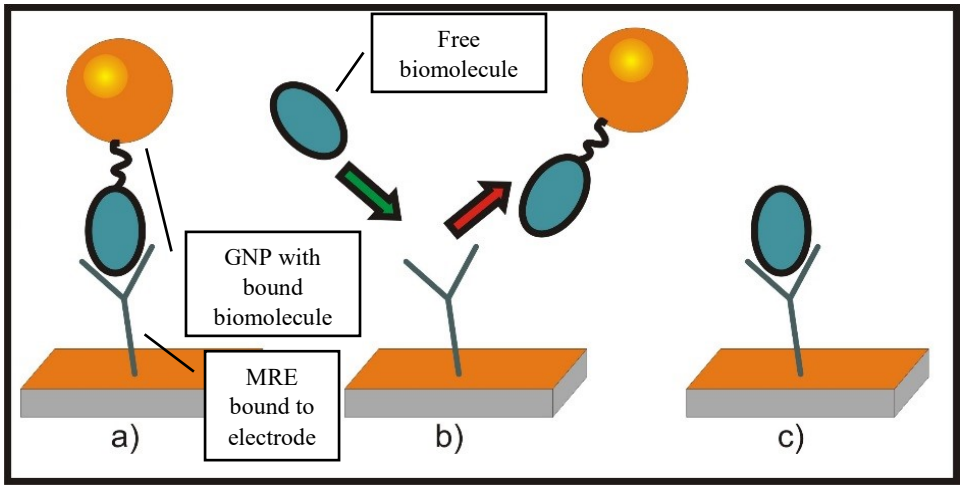

Figure 2.4: The basic concept behind competitive assays. a) Initially, copies of the target biomolecule which are attached to gold nanoparticles bind to recognition elements on the sensor surface. b) When free copies of the target biomolecule are present (i.e. from a tested sample) they have a higher binding affinity than those bound to the gold nanoparticles. c) The gold nanoparticle/biomolecule probes are removed in favor of the free biomolecules and the absence of the nanoparticles causes a detectible change in the measured electrical impedance.

The cysteine detection competitive assay was carried out by first modifying the gold electrodes with thiol-modified PEG, then attaching cysteine antibodies to the –COOH group on the end of the attached PEG. These antibodies bind strongly and specifically to cysteine. As a baseline an impedance reading of the antibody-modified electrode was taken ("control" in Figure 2.6). Next, cysteine modified GNPs were added to electrodes followed by a buffer wash to remove GNPs not bound to antibodies, and a second impedance measurement was taken (in a much similar way to the previous proof-of-concept experiment). Finally, a pure sample of cysteine (approximately 1nM solution) was added to the electrodes and allowed to replace the nanoparticles and the electrodes were washed a final time to remove unbound nanoparticles before a final impedance measurement.

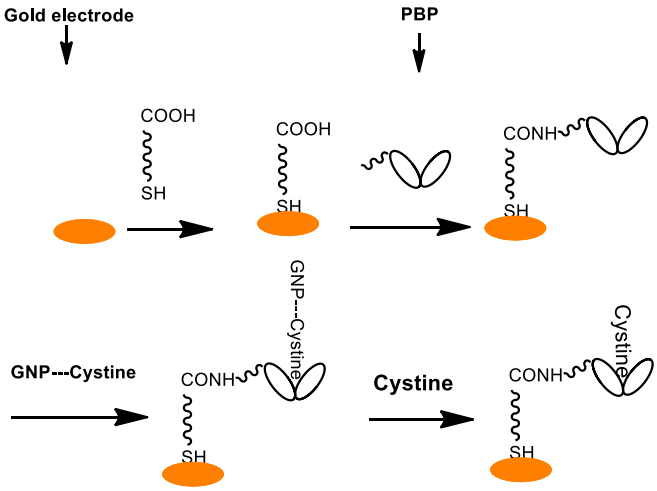

Figure 2.5: Experiment overview for detecting cystine. First gold on IDEs is modified with -COOH functional groups using thiol binding. Next, a periplasmic binding protein that acts as an MRE for cystine is bound to the modified electrodes. Impedance measurements were taken at this step for the "control" measurement. GNPs bound to cystine were then added (which should bind to the MREs) and measurements were taken again. Finally free cystine was added to "knock out" the GNPs and a final measurement was taken.

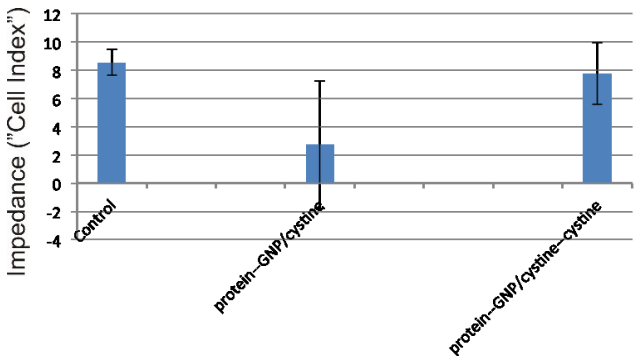

Figure 2.6: RT-CES results for detecting cystine. “Control” refers to measurements after the electrodes were modified with antibodies. “Protein-GNP/cystine” refers to measurements after the addition of GNPs modified with cystine. “Protein-GNP/cystine-cystine” refers to the last step where pure, free cystine is added.

The results of this experiment are shown in Figure 2.6. As with the first proof-of-concept experiment, there was a statistically significant decrease in relative impedance for the electrode with bound nanoparticles compared to without nanoparticles, showing that the cysteine modified nanoparticles did bind to the antibodies on the electrode surface. When the free cysteine was added, the average relative impedance increased again, however the larger variation in both this and the previous measurement means there is no statistical change in this case. Meaning that more sensitivity and better repeatability are required for competitive assay detection.

For the second metabolite, THF, the experiment was mostly the same as for cysteine, with a few key differences. First, instead of an antibody MRE, a THF DNA aptamer was used. Aptamers are generally much smaller than antibodies and much more robust, and can have comparable selectivity and sensitivity [21], [74]. The other main difference is that several different control cases were tested, including an alternate metabolite to test for binding specificity, an important factor for testing complex biological samples.

Modifying the electrode surface with the THF aptamer was accomplished by taking advantage of the DNA structure of the aptamer. Since the aptamer is simply a specific sequence of single stranded DNA (which due to self-folding forms the 3D structure required for metabolite binding), it was a simple process to acquire that aptamer sequence with a specific binding sequence on one end. This DNA “tail” was designed to have no effect on the aptamer itself, but it could bind

to a linking strand of thiol-DNA attached to the electrode, in much the same way DNA-modified nanoparticles were attached to the electrodes in the first proof-of-concept experiment. Once the aptamer was bound to the electrode, this experiment proceeded in much the same way as the previous one. Here, THF-modified nanoparticles were used and were displaced by free THF. In addition to these nanoparticles, GNPs modified with taurine (another metabolite), were also added to THF/aptamer-modified electrodes as a control. As an additional control, impedance was measured with the linker and THF-modified GNPs, but without the THF aptamer to confirm aptamer binding.[2]

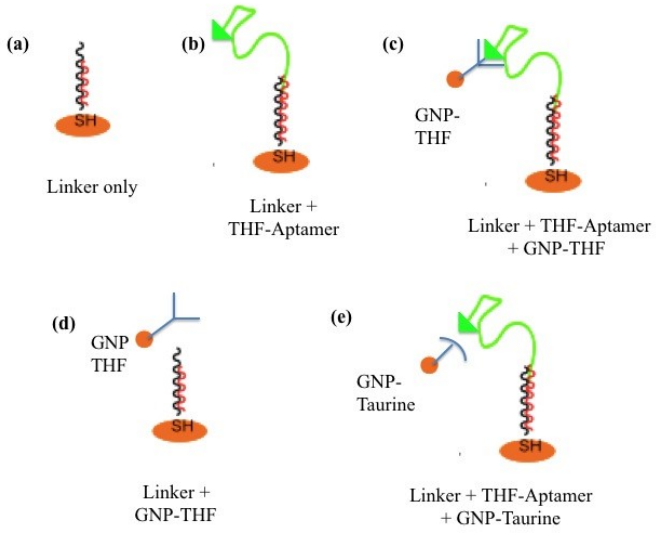

Figure 2.7: The different cases measured for the THF aptamer experiment. a) The electrode with the DNA linker only. b) The electrode with the linker and THF aptamer. c) The electrode modified with THF aptamers with THF-modified nanoparticles. d) Control case without THF aptamers. e) Control case with taurine-modified nanoparticles instead of THF nanoparticles. Each case other than case C should not have any bound GNPs ant thus should have no impedance change.

[2] I would very much like to thank and acknowledge Xiaoyan Yang and Yollanda Hao for their work with these proof-of-concept experiments. They started testing with the RT-CES system before I joined the project and were responsible for most of the chemistry for the proof-of-concept testing.

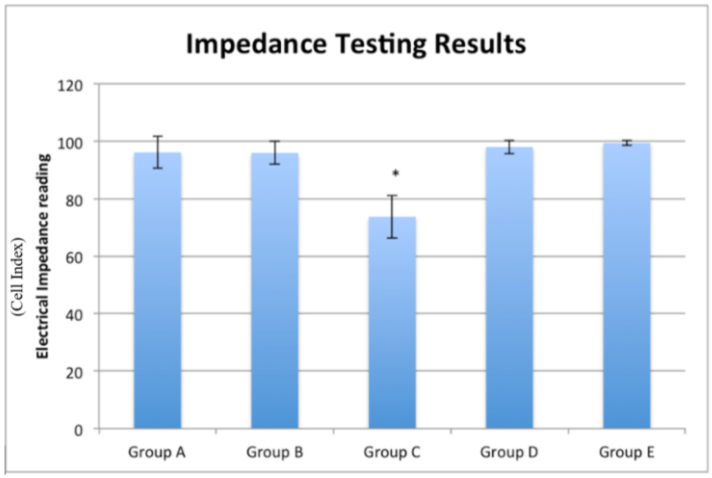

Group A	Linker only
Group B	Linker +THF-Aptamer
Group C	Linker +THF-Aptamer + GNP-THF
Group D	Linker +GNP-THF
Group E	Linker + THF-Aptamer + GNP-Taurine

Figure 2.8: Relative impedance measurements from the RT-CES system for the THF aptamer experiment. The different cases correspond to those in Figure 2.7. The "*" above the Group C results denote that that is the one case where there should be bound gold nanoparticles, and thus a change in impedance, which there was. There is no statistical difference between Groups A, B, D, and E, each being negative control cases.

The results of this experiment show again that gold nanoparticles bound to the RT-CES electrodes cause a measurable change in impedance. Additionally, this experiment shows that the THF aptamer is effective at binding THF-modified nanoparticles (as shown by group C and D), and binding them specifically (shown by group E). The similar metabolite, taurine, on nanoparticles did not change the impedance, indicating that the THF aptamer did not bind the nanoparticles. The only statistical difference in impedance is with Group C, the only case where GNPs should be bound to the electrodes. In this experiment, the "relative impedance" is a reflection of a change in the "cell index" measured by the RT-CES. This value is a proprietary measurement used by the system, and is directly related to changes in impedance.

2.2.3. RT-CES Experiment Discussion

It is clear from the proof-of-concept experiments that the RT-CES, a system designed for detecting cell growth, is capable of also detecting metabolites using gold nanoparticles for signal enhancement. Indeed, this system was invaluable in laying the groundwork for an impedance-based biosensor. However, the RT-CES has many shortcomings in this regard as well, making it well suited for these early stage tests, but not much else when it comes to this type of biosensor application. First and most obvious is the size of the system. The guidelines outlined in the CRIO project are for a biosensor that is portable and affordable, the RT-CES is neither. The system itself is a large box controlled by a separate laptop computer, with a total cost of well over $10000, not including the cost of the gold electrodes it uses [75]. The goal for this project is to create a handheld device with an approximate cost on the order of $500, or lower. The second major problem with using the RT-CES for these applications is that the system is very much a “black box”. That is, there is very little room for customizing the system. The electrodes used for the system are all the same. Other than the amount of time something is measured for, there is no real way to change how the system measures samples (input voltage, frequency etc.). The results it produces are all in terms of a value called “cell index”, which is a function of changes in impedance the system measures. This is why the results shown for the experiments done with the RT-CES are in terms of relative changes in impedance based on a baseline value. There is no way to extract the actual raw impedance values from the system, or even exactly how it measures these values. For these reasons, while the RT-CES is very well suited for its original purpose of monitoring cell growth, and was useful in proof-of-concept experiments, it is definitely not well suited as an impedance based biosensor, and therefore a new, better suited device must be designed.

2.3. LCR Meter Experiments

In order to have more control over measurement parameters for early stage testing an LCR meter (the U1733C from Aglient Technologies) was purchased. This LCR meter is capable of making precise impedance measurements over a wide range and is capable of taking measurements at multiple discrete frequencies (ranging from DC to 100 kHz). These features make this meter, although not as robust as more sophisticated systems, useful for early testing and refinement.

Figure 2.9: The LCR meter used for early experiments. The U1733C LCR meter from Aglient Technologies was used to measure the impedances of IDEs. The LCR measures impedance magnitude and phase (as well as resistances, capacitances, and inductances) at several set frequencies. While the RT-CES does automatically measure impedance over a range of frequencies, the LCR offers more control over the measurements; it displays exact impedance information rather than just a relative value (the RT-CES "cell index" measurement.

The LCR meter presented the opportunity to better characterize the impedance of the RT-CES electrodes, measuring their impedance at different frequencies, in different buffers, and recording actual impedance magnitudes and phases. Using the LCR also meant that completely different electrodes could be tested. The electrodes for the RT-CES are designed for the sole purpose of growing and detecting cells, with materials and dimensions suited specifically for this end. As a first alternative to the RT-CES electrodes, individual interdigitated gold electrodes (purchased from BVT Biosciences) were tested. Originally made for measuring conductivity of solutions, these electrodes have much wider electrode digits and gap spacing than the RT-CES IDEs, and also therefore less digit pairs. They are thick film printed gold electrodes printed on a water-safe paper substrate. One main advantage of these for testing is that the gold and substrate for the electrodes are bare, unlike the RT-CES electrodes which are specially treated so cells will adhere to them while growing.

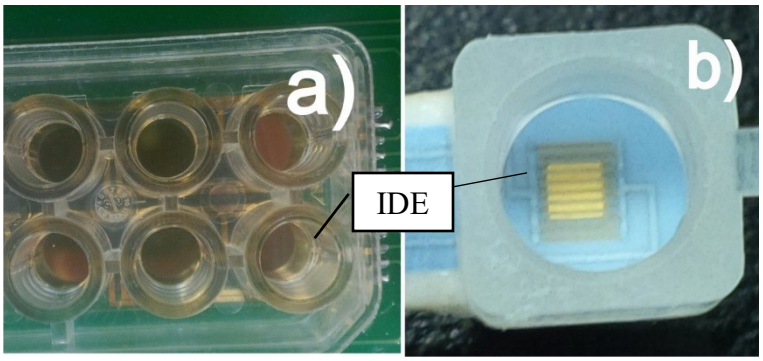

Figure 2.10: A comparison between the IDEs from the RT-CES e-plate (a) and the BVT conductivity sensor (b). While the size of the sample wells is about the same for both, the dimensions of the electrodes are clearly quite different. The e-plate electrodes (a) have much smaller dimensions (not even visible in this picture) and more gold coverage. The individual gold digits are visible on the BVT electrode (b).

With greater freedom with what to measure, as well as new different electrodes to test, the same proof-of-concept DNA GNP binding experiments were done again. With the LCR meter, greater insight could be extracted as to the exact impedance values that change due to bound GNPs, the exact sensitivity of the electrodes to bound GNPs, and the most effective frequencies for the sensor to test.

In addition to basic measurement and characterization of electrodes with the LCR meter, the same Poly A/Poly T experiments that were carried out with the RT-CES were done with the LCR meter. For these experiments, first the nanoparticle probes were synthesized (as described previously) and the thiol-modified Poly T DNA strands were attached to the gold electrodes. After the Poly T was given time to attach, the excess solution is removed from the electrodes and some of the prepared nanoparticle probes were added. A number of control electrodes were also tested, usually either without the attached Poly T strands or without adding nanoparticle probes. Thus the control samples should not have any bound nanoparticles.

After the excess nanoparticles were removed, a PBS buffer with a pH of 8.0 was used to add a charge to the PEG on the modified nanoparticles; however, the conductivity of this buffer is so high that it overwhelms any change due to the nanoparticles. To remove this effect, the

electrodes are washed with water (usually twice) so that a difference can be seen between the tested electrodes and the controls. Measurements were taken on the single BVT electrodes, with each test repeated in triplicate. Impedance values were taken at a single 10 kHz frequency and results were normalized to show differences in the results. Other frequencies used by the LCR meter were investigated, with some similar behaviour to the results shown in Figure 2.11, but the best results were at this frequency. The effects of measurements at a range of frequencies are investigated in future chapters.

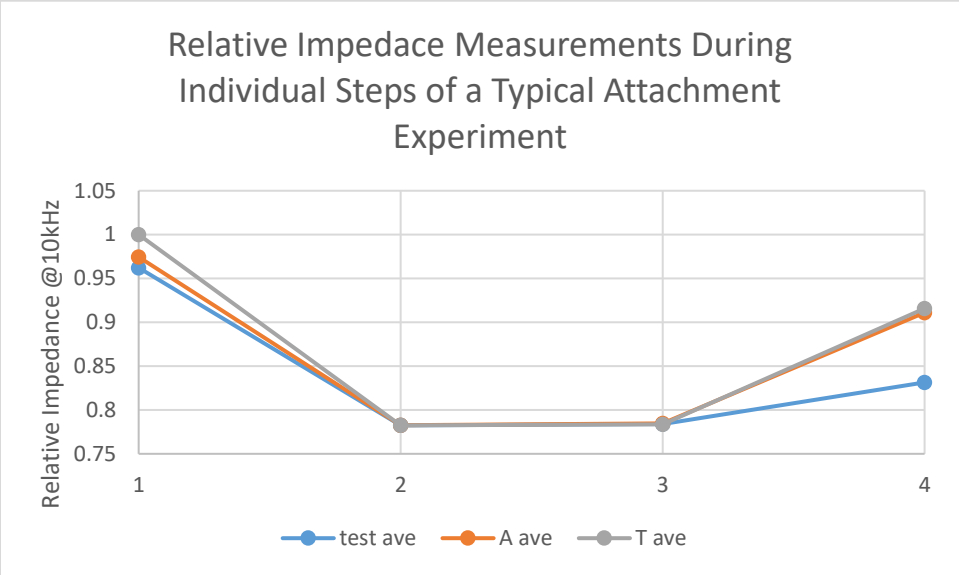

Figure 2.11: LCR experiment with BVT conductivity sensors used along with 30nm gold nanoparticle probes. Measurements were taken at 10 kHz input frequency. The blue line "test ave" is the average of three tested sensors whereas "A ave" and "T ave" are two different control cases. Point 1 is an initial measurement with the nanoparticle probes in the sensor wells, 2 is when pH 8.0 PBS is added, and 3 and 4 are subsequent washes with distilled water. Here it is shown that there is no significant difference until the second wash due to the PBS overwhelming the measurement. Here, impedance data is represented by a relative impedance, normalizing all values to the initial value of "T ave".

As with the RT-CES there is a measurable change in impedance for bound nanoparticles compared to the control cases. This shows that the much larger BVT electrodes can be used for this application, and the much less expensive LCR meter is capable of measuring these changes (this time with known set input frequencies and actual impedance values). However, there are

definitely still many issues with this approach. The high pH PBS buffer used contains a high concentration of mobile ions, leading to high conductivity overshadowing any effects of the nanoparticles, thus requiring several washes with pure water to remove the effect of the buffer. This is a fickle process. Excessive washing removes the effect entirely, while washing inconsistently causes inconsistent results. Although this experiment does show results and is an effective proof-of-concept, refinement is required for a functional device.

A separate mechanism for detection is that the presence of the gold nanoparticles themselves is able to sufficiently increase the conductivity of the sensor for detection. Instead of adding a high pH buffer, a low ion concentration neutral background buffer is used for measurements after nanoparticle probe attachment. A low ion concentration buffer is used rather than distilled water because it is necessary to facilitate some charge transfer for these conductivity measurements and for there to be enough electrical screening (more on electrical screening and its effects on the sensor in Chapter 3).

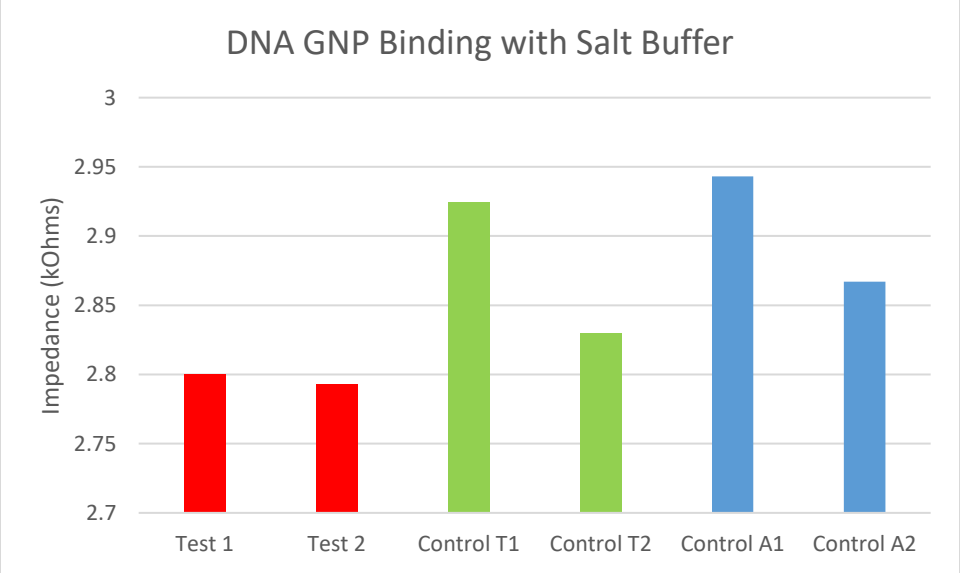

Figure 2.12: Results of impedance measurements with a low concentration salt solution buffer. The two “Test” bars refer to the full sensor experiment with DNA attached to the electrodes and the nanoparticle probes. “Control T” are sensors with DNA attached to the electrodes, but without nanoparticle probes. “Control A” are sensors with nanoparticle probes, but without electrode bound DNA. Measurements were taken in a low ion concentration neutral pH buffer (150 µM

KCL) with 60nm gold nanoparticle probes used and an input frequency of 10 kHz from the LCR meter. Measurements were taken on RT-CES electrodes.

Both of these procedures have yielded insightful results to some degree during experiments. Overall, the results from the low concentration buffer are more consistent than the high pH method due to the fewer washing steps involved. The fact that both of these techniques produced similar results suggests that the prevalent mechanism for impedance change is the gold nanoparticles themselves and not a fixed charge on them.

2.4. Influences

A variety of different biosensor designs has been discussed in the previous chapter, with different ways to detect and report biomolecules depending on the specific application, and one of these ways being interdigitated electrode impedance-based electrical detection. But even within this subsection of a subsection of biosensor design, there are still many variations on this one theme. By investigating the reasoning behind these variations in designs, it was then possible to get a better picture of how to best improve my own design. There is no one single best design for all purposes and applications. There are designs for highly sensitive detection of very specific molecules, and designs for rough estimates of large cells (like the RT-CES). But an understanding of the underlining mechanisms, similarities, and differences between designs can lead to better insight into my own design.

The monitoring of cellular growth is a popular application of IDE sensors. Systems like the RT-CES are made specifically for that purpose. Researchers such as Ehret et al. [76], [77] and Radke et al. [51] have studied the design, mechanism, and optimization of these types of sensors. They use equivalent circuits to model the electrodes, surrounding buffer fluid and attached cells [51], [76].

There are multiple valid equivalent circuits, but all account for the capacitance of the interdigitated electrode (which is itself just a capacitor), the resistance of the surrounding solution, and the electrical impedance of attached cells, usually including capacitances from cell membranes and resistances from the cells themselves [51], [76]. Using these circuits, the impedance of the system can be simulated, which further informs the design and the expected values that need to be

measured for an effective sensor. While my own sensor design is not for measuring cells, the same equivalent circuit technique can be applied, replacing the cells with signal enhancing gold nanoparticles (more on this in Chapter 3). In addition to equivalent circuit models, Radke et al. also simulates the electric field surrounding IDEs in a buffer solution [51]. The purpose of this is to show the electrical screening around the electrodes. Briefly, free charges form the ions in the buffer solution neutralize and screen out the electric field above the IDE. Depending on the applied voltage and the buffer, this screening limits the electric field to a small area above the electrodes and thus disruptions to this electric field caused by bound cells can have a greater effect [51] (for a more detailed description of electric screening see Chapter 3).

It's not just cells that are detected with IDE sensors. Designs have been proposed by groups for detecting small molecules such as toxins, biomolecules, and DNA [63], [78]–[80]. Detecting such small molecules can provide new challenges not present when detecting large cells which easily disrupt the electric field around electrodes. Smaller analytes in small concentrations have smaller impacts on electrical impedance. This is something that has to be considered and accounted for in such designs, including my own. There are three main ways IDE sensor designs can adapt to detecting small molecules: more sensitive and detailed measurements, more sophisticated electrode design, and signal enhancing tags.

The changes in impedance caused when detecting smaller analytes can be small and subtle. To see these changes, it is often necessary to use more sophisticated impedance detection. Rather than simple impedance measurements, techniques like electrochemical impedance spectroscopy (EIS) are used to analyse electrodes' impedance, both real and imaginary, over a large range of frequencies [46], [57], [65], [81]–[86].

Second, for smaller analytes, generally, IDEs with smaller dimensions are required. As the size of the target analyte decreases, the area of the electrodes, width of the IDE digits, and the spacing between digits must be decreased accordingly. In general, the smaller the spacing between electrode digits, the more sensitive the resulting electrode will be. Where larger electrodes (such as ones for measuring cell growth) have spacing with 10's or 100's of microns [51], [76], [77], sensors that can detect DNA for example have spacing that is less than half a micron [63], [80]. Putting the dimensions of the electrodes at the same scale as the target means that bound targets

can have more of an overall effect. There are trade-offs for having such small dimensions though, as smaller dimensions mean more complex fabrication techniques and increased cost.

The third commonly used technique for detecting smaller analytes is to amplify the impedance changing effect with an enhancing tag. These range from simple metal tags, to more complex chemical processes. The most common of these is to use signal enhancing gold nanoparticle tags [87]. These can be modified with additional recognition elements [88], directly modified with the target analyte, or used as a platform for attaching further signal enhancing molecules [66], [89]. Ahn et al. designed a technique that uses bound gold nanoparticles as "seeds" to use a chemical reaction, reacting $HAuCl_4$ and hydroxylamine to "grow" gold on the nanoparticles, enough to even bridge the spacing between IDE digits [63].

2.5. Conclusion

Proof-of-concept experiments have shown that an impedance based, gold nanoparticle enhanced, interdigitated biosensor system is feasible for detecting metabolites. This establishes confidence to continue development. However, these experiments were very basic, and a far cry from the sensitive, portable, inexpensive biosensor that is the goal of this research. Inspired by similar work in similar designs, but focused on our own specific design, the next major goals are to improve upon the sensor. There are several ways which this is accomplished and they are presented here in several distinct parts. First, in the next chapter, the design, testing and optimization of interdigitated electrodes is discussed. Next, the binding chemistry and sensing conditions are tested. And finally, the electronics involved in impedance measurement and the conditions for impedance measurements are designed. Although these are all presented separately, they are indeed not truly independent of one another. Each of these design elements influences each other. For example, the buffer used for measurement changes the impedance range that needs to be measured by the device. Changing the dimensions of the electrode may increase the sensitivity, but change the best measurement frequency. So, although each aspect is addressed separately here, all aspects of this biosensor design are intimately connected.

Chapter 3 : Electrode Design

3.1.Introduction

The material, dimensions and overall design of interdigitated electrodes are very important to consider when designing an IDE biosensor. Throughout the testing of this biosensor system, there have been many iterations of electrode designs as shown in Figure 3.1.

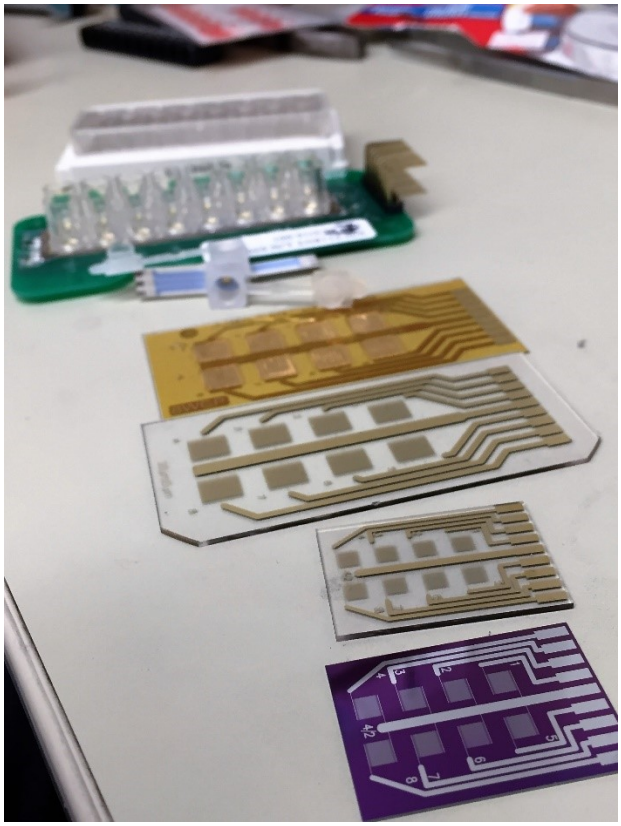

Figure 3.1: Just some of the different iterations of IDEs tested during the course of the biosensor research. From the top: the RT-CES cell counting electrodes, to the BVT IDE conductivity sensors, plastic IDE cell counting electrode, to custom made electrodes, both larger ones and smaller ones made from glass, and finally small aluminum IDEs.

Many sources have shown interdigitated electrodes to be an effective platform on which to base biosensor designs [15], [57], [63], [76], [79], [80], [90]–[93]. However, as discussed previously, the actual designs of the IDEs used can vary widely depending on the target analyte, exact detection method and proposed application. An IDE ideal for measuring cell growth would be far less effective in detecting DNA, and an IDE made for highly sensitive detection may be far too expensive to fabricate for some practical purposes. It therefore became necessary to find the exact IDE design that would be ideal for the purposes of this metabolomic biosensor. It would have to be sensitive enough to detect low concentrations of metabolites (with signal enhancing gold nanoparticles), while still relatively inexpensive enough for use as disposable chips for a point-of-care biosensor. The original goal of the project was to have each test for a metabolite cost $10 Canadian or less, which would include the electrodes, any fluidics for sample handling, buffers used in each test, and nanoparticles and binding agents used for detection.

Initially, as described in Chapter 2, IDEs were adopted from other applications for proof-of-concept experiments. Cell-detecting electrodes, conductivity electrodes, screen printed electrodes were all tested first. Although proof-of-concept experiments were successful in showing the biosensor design can work, there was a lot of room for improvement. Therefore, custom made electrodes were designed based on these proof-of-concept electrodes and similar reported designs [57], [76], [80], [90], [94]. Electrodes designed for detecting small molecules generally have much smaller dimensions then ones that detect cells. Smaller electrode digit widths and, more importantly, spacing between electrode digits lead to higher sensitivity to bound analytes [51]. Different materials have also been employed for IDEs, including different insulating substrates, like plastic, glass and silicon dioxide (SiO_2). Although gold is the most popular material for IDEs due to its biocompatibility, other metals, like aluminum have been used [95]. Based on the insight gained by studying these different designs, the next task was to design IDEs optimized for this specific biosensor application. Even with enough research to make an “educated guess” as to the best electrode design, still a large number of combinations of design factors would need to be tested to fins the optimal design. Therefore, to save on the excessive time, effort, and money a series of simulations were carried out to further narrow down the optimal design. Once simulations were completed, electrodes were made based on simulation results.

3.2. Simulations of IDEs

Finite element analysis simulations were carried out using COMSOL Multiphysics software (www.comsol.com). This software simulates the exact testing conditions, electrode materials, and electrode dimensions, and can display visual representations of electrical properties around electrodes, as well as predict exact impedance values for all such cases. This software became an incredibly useful tool not only in designing electrodes, but also for determining and displaying the mechanism by which gold nanoparticles bound to the electrodes could change the electrode's measured electrical impedance. Other factors that could be tested for were the effects of different measurement buffers, different binding chemistries, different kinds of nanoparticles, and impedance measurements at varying frequency ranges.

Through the course of simulating and designing biosensors designs, two main detection methods were studied, that is, there were two different ways investigated here in which, depending on the design, chemically bound gold nanoparticles could change the impedance of an IDE. The method initially used by the proof-of-concept experiments was attaching MREs directly to the metal of the electrodes themselves, then binding nanoparticles to the electrode digits (in the presence of the target analyte). This results in the bound nanoparticles essentially "thickening" the electrode digits, changing the properties of the electrodes and causing a decrease in the overall measured impedance. This decrease in impedance can be seen in the results of early proof-of-concept experiments (see Chapter 2). The second method deploys the MREs in the space between electrode digits, resulting in bound nanoparticles filling the space when target analytes are present. In this case, as simulations show, the position of the nanoparticles actually causes an increase in impedance, rather than a decrease as in the first case.

Though the two methods have many differences between them in terms of their simulations, practicalities, and resulting impedance changes, there are several key similarities in how these simulations are considered. In a general sense the setup for both simulations are the same. By taking advantage of the symmetrical layout of IDEs simulation complexity could be cut down by essentially making the simulations in 2D. By taking a side view cutting across the direction of the electrode digits and then extending that slightly, small "slices" of the electrode area could be simulated. Then, by adding up the effects of multiple areas, the behaviour of the entire electrode could be simulated. This saved the extra time and complex computations that

would be required to simulate the entire electrode area in 3D. The second similarity between the two approaches is the importance of electrical screening.

Electrical screening, also called Debye screening is an important phenomenon in microfluidic design [96] and an important consideration in many aspects of electrochemical research [46], [97], [98]. Simply put, electrical screening occurs when large numbers of free charges in a solution (like positive and negative ions in a solution), gather around fixed charges (such as charges on the surface of the electrodes in these simulations). The electrical potential of the fixed charges affects the charge distribution of the free charges such that the free charges cancel out (or screen) the potential of the fixed charges. So, after a set distance away from the fixed charge, characterized by a property called the Debye length, the potential from the fixed charged is effectively screened out completely.

To understand better how this electrical screening effect can be controlled and even turned to the advantage of this biosensor design, a quick derivation is necessary. First, consider, for the sake of simplicity, instead of the full electrode, just a glass surface covered in a salt solution as shown in Figure 3.2. In a solution, the surface of the glass naturally forms a negative surface charge. The surrounding solution has a combination of singly charged ions, but is overall electrically neutral.

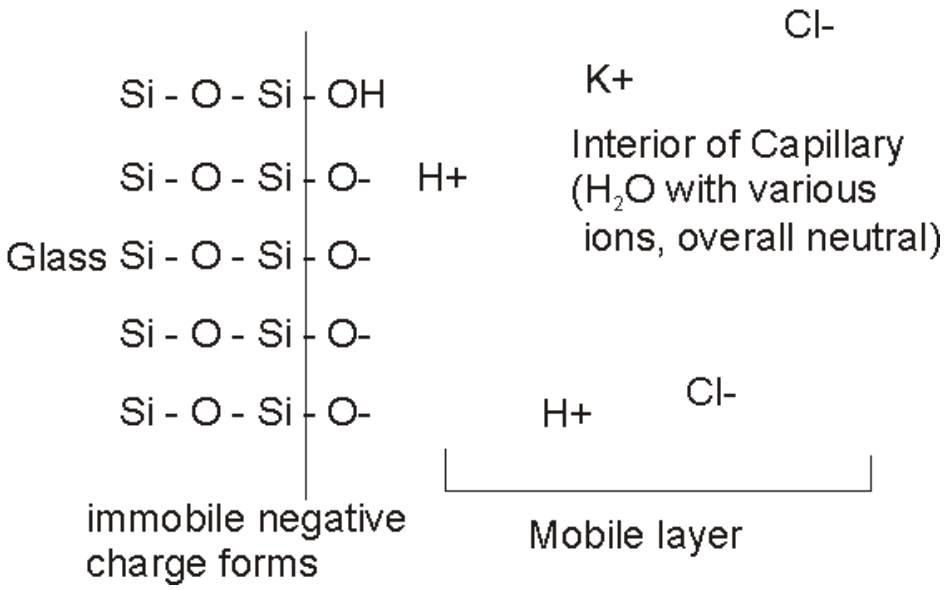

Figure 3.2: Initial setup of the derivation of electrical screening on a charged surface. Here, a glass surface is surrounded by a solution with singly charged ions (with the total charge of the solution

being neutral). In this solution, the surface of the glass forms a negative surface charge (the immobile layer). The interaction between the mobile and immobile layers form the electric double layer.

The relationship between the charge distribution of the free charges and the potential of the system is described by Poisson's equation:

$$\nabla^2\psi = \frac{-\rho}{\varepsilon} \tag{3.1}$$

Here ψ is the potential, and ρ is the charge density. This equation can be expanded upon given that the charge density is just a summation of the different charged entities in solution, each described by a Boltzmann distribution.

$$\nabla^2\psi = \frac{-1}{\varepsilon}\sum_i n_i e z_i \exp(\frac{-z_i e\psi}{k_B T}) \tag{3.2}$$

This can be even further simplified assuming that the solution is overall electrically neutral and all of the entities are singly charged. In this case, there are two entities (n_1 and n_2) with the same properties but oppositely charged, reducing the sum to two terms.

$$\nabla^2\psi = \frac{en_0}{\varepsilon}\left[\exp\left(\frac{e\psi}{k_B T}\right) - \exp(\frac{-e\psi}{k_B T})\right] \tag{3.3}$$

Using some simplifying assumptions this reduces to:

$$\nabla^2\psi = \frac{2en_0}{\varepsilon}(\frac{e\psi}{k_B T}) \tag{3.4}$$

This equation can be solved for the potential as a function of the distance away from the fixed charge surface (y).

$$\psi = \psi_0 \exp\left(\frac{-y}{\lambda_D}\right) \tag{3.5}$$

Here, ψ_0 is the electrical potential at the charged surface, and λ_D is the Debye length, defined by:

$$\lambda_D = \sqrt{\frac{\varepsilon k_B T}{2n_0 e^2}} \tag{3.6}$$

There are a few key observations to be made here. First, the potential with screening is the same as the potential without screening, except with exponential decay as distance from the surface

increases. There is a critical distance from the surface where the potential drops to negligible levels, which is characterized by the Debye length. The smaller the Debye length, the smaller the distance until the potential is screened out. The Debye length itself can be controlled. It is inversely proportional to the concentration of free charges in solution.

With this understanding of electrical screening and how it relates to electrodes for this biosensor application, it is possible to not only account for the effects of screening, but to take advantage of them. There are several ways this is possible. First, electrical screening limits the electrical potential of the electrodes to a certain distance, and since detection with this biosensor design depends entirely on manipulating this potential, screening also limits the area where detection can take place. Essentially the biosensor electrodes cannot detect anything past the screening length. This property can be leveraged to adjust the area of interest above the electrodes. Designing larger screening distances enables detection of larger analytes, or while decreasing the screening distance limits detection to areas directly at the surface of the electrodes [51], [97]. With the proper electrical screening for example, only closely bound nanoparticles can change the impedance of the electrodes, and unbound nanoparticles can have a significantly reduced effect. The second way that screening can be used directly relates to the second detection method simulated, where nanoparticles are bound between electrode digits. Screening occurs around all charged surfaces in the biosensor system, including on the surface of the gold nanoparticles. Electrical screening creates a separation of charges between the fixed charge layer and the free charges past the Debye length, essentially creating a capacitor around all charged surfaces. This is how nanoparticles bound between electrode digits can act as additional capacitances in the system and cause an increase in impedance.

3.3. COMSOL Simulations of Gold Nanoparticles on Electrode Digits

For the first method of detection, COMSOL simulations were carried out to test multiple factors associated with the electrical properties of the designed electrodes. The simulations were set up with the model described previously: two dimensional cross-sections of electrode digits that are extended to create a three dimensional representation. Results for this method of simulation are displayed in terms of either electrical potential or electric field magnitude, with changes in electric field magnitude directly relating to the final measured impedance of the electrodes.

Simulations for this case were based on a Nernst-Poisson simulation method [99]. The overall charge distribution of the entire system is determined by the Poisson equation:

$$\nabla^2\phi = -\frac{eN_A}{\epsilon}\sum c_i z_i \tag{3.7}$$

where ϕ is the electrical potential of the system, ε is the electric permittivity of the solution, the concentration of each ion (c_i) refers to the concentration as a function of location in the system, e is the elementary charge, N_A is Avogadro's number and z_i is the charge number (e.g. +1 or −1 for singly charged ions). Although the initial condition is for a uniform distribution of ions, they drift due to the applied voltage and surface charges, causing variations in the overall concentration, in turn influencing the potential. These changes in the concentration (c_i) of the ions over time (t) is described by the Nernst-Planck equation:

$$\frac{\delta c_i}{\delta t} = \nabla\left[D_i\nabla c_i - uc_i + \frac{D_i z_i e}{k_B T}c_i\left(\nabla\phi + \frac{\delta A}{\delta t}\right)\right] \tag{3.8}$$

where D is the diffusivity of the ions, u is the fluid velocity, k_B is the Boltzmann constant, T is the temperature and A is the magnetic vector potential. This equation is simplified in this case as the fluid itself does not move ($u = 0$) and there are no magnetic fields ($A = 0$):

$$\frac{\delta c_i}{\delta t} = \nabla\left[D_i\nabla c_i + \frac{D_i z_i e}{k_B T}c_i\nabla\phi\right] \tag{3.9}$$

which accounts for both ion migration due to the applied voltage at electrodes ($\frac{D_i z_i e}{k_B T}c_i\nabla\phi$), and due to the concentration gradient created by this applied voltage ($D_i\nabla c_i$). Using these above equations, the COMSOL simulations are able to calculate the changes in concentrations of ions in IDE systems over time, as well as the resulting changes in electric field and electric potential distributions.

The first simulations using this method were done to demonstrate the migration of ions in solution over IDEs during measurements as well as show the formation of electrical screening layers over those IDEs. The electric potential of an IDE was simulated using three representative gold digits, each 5 μm wide with 2.5 μm between them with a 0.1V DC voltage applied to the electrodes (alternating positive and negative). For the surrounding background material water was used, including all relevant physical and electrical properties. In addition to this 150 μM KCL solution was simulated by adding an initially uniform concentration of positive and negative ions,

each with their respective diffusion constants and charges. The results of the simulation were taken at different times after the initial conditions were set. The results show that over time, the movement of the ions decreases the potential above the electrodes, showing both the formation of electrical screening and how it effects the electrodes.

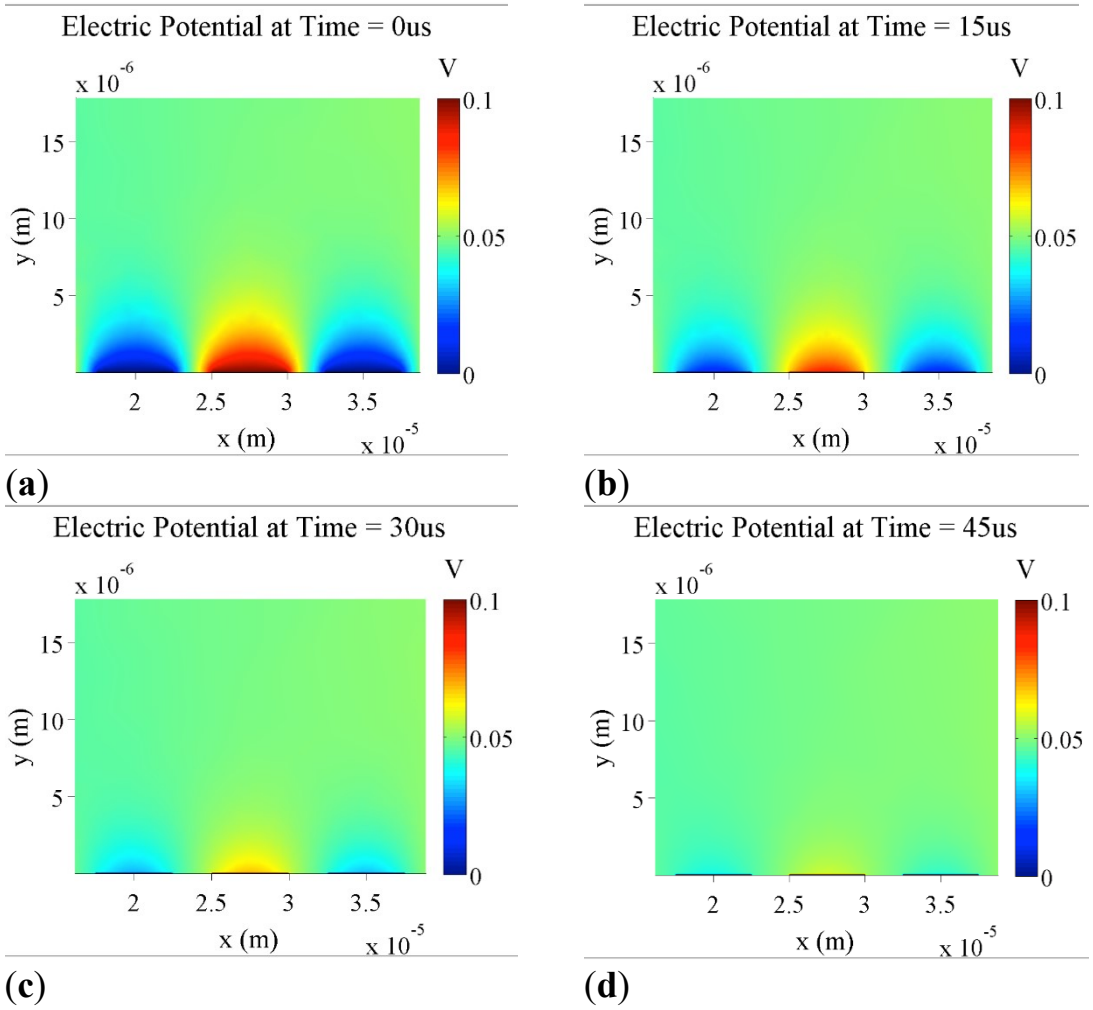

Figure 3.3: Simulation of the formation of electrical screening layers over time. Plots show the electric potential of IDEs (5 µm digit width and 2.5 µm spacing) with 0.1 V DC applied with a background KCl concentration of 150 µM. Plots are taken at five different time points: (**a**) $t = 0$ s; (**b**) $t = 15$ µs; (**c**) $t = 30$ µs; (**d**) $t = 45$ µs.

While these simulation results are useful in showing the process of electrical screening as it pertains to the electrode system, and help show the validity of the simulations, they are just simulations of well-known processes and phenomena. The real useful results come from showing

the effects of gold nanoparticles on the electrodes. Nanoparticles bound to the gold digits of the electrodes were modeled as gold circles, extended along with the rest of the two dimensional structure (effectively creating "nano-cylinders" that approximate nanoparticles) as shown in Figure 3.4. Here, the nanoparticles are set 20 nm above the surface of the electrodes to account for the spacing from connecting binding elements between the two.

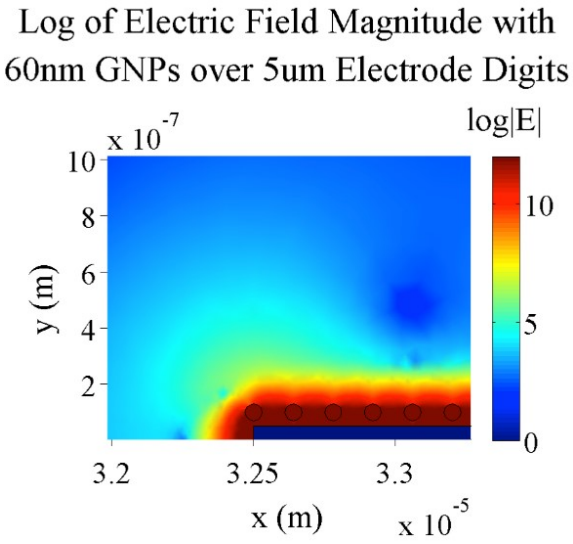

Figure 3.4: Electric field magnitude of a 5 µm gold electrode with 60 nm GNPs placed 20 nm above the electrode. A voltage of 0.1 V is applied to the electrode here and the field is in the presence of a 150 µM KCl buffer solution.

The effect of the nanoparticles on the electrodes can be seen in the magnitude of the electric field with and without bound GNPs. This difference was shown in the simulation by graphing the electric field magnitude directly between two adjacent electrode digits.

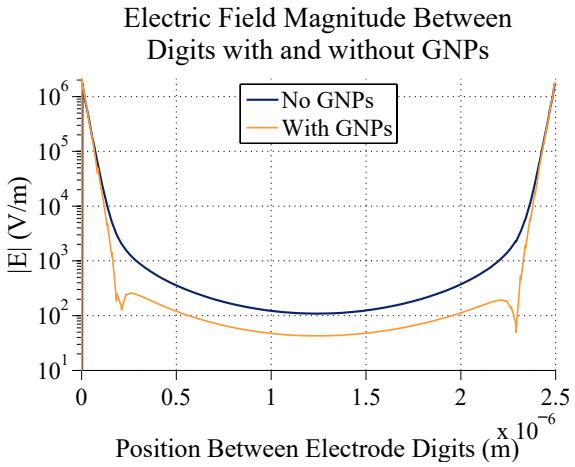

Figure 3.5: A graph comparing the electric field magnitude between 5 µm digits with 2.5 µm spacing with and without 60 nm gold nanoparticles 20 nm above the electrodes.

These simulation results show that there is a decrease in the electric field magnitude between electrode digits caused by gold nanoparticles bound to the electrode digits. This trend is in line with the early proof-of-concept results for this sensing technique. Next, these simulations could be used to change conditions as to maximize this change in electric field magnitude. There are many factors that can be adjusted, and using simulations affords much more flexibility in trying different conditions. For these simulations, conditions included changing the ion concentration of the measurement buffer, changing the dimensions of the electrodes, and changing the size and placement of the gold nanoparticles. The sensitivity of the electrodes increased in simulations as a result of higher background ion concentration and as a result of a smaller gap between electrode digits, as shown in Figure 3.6.

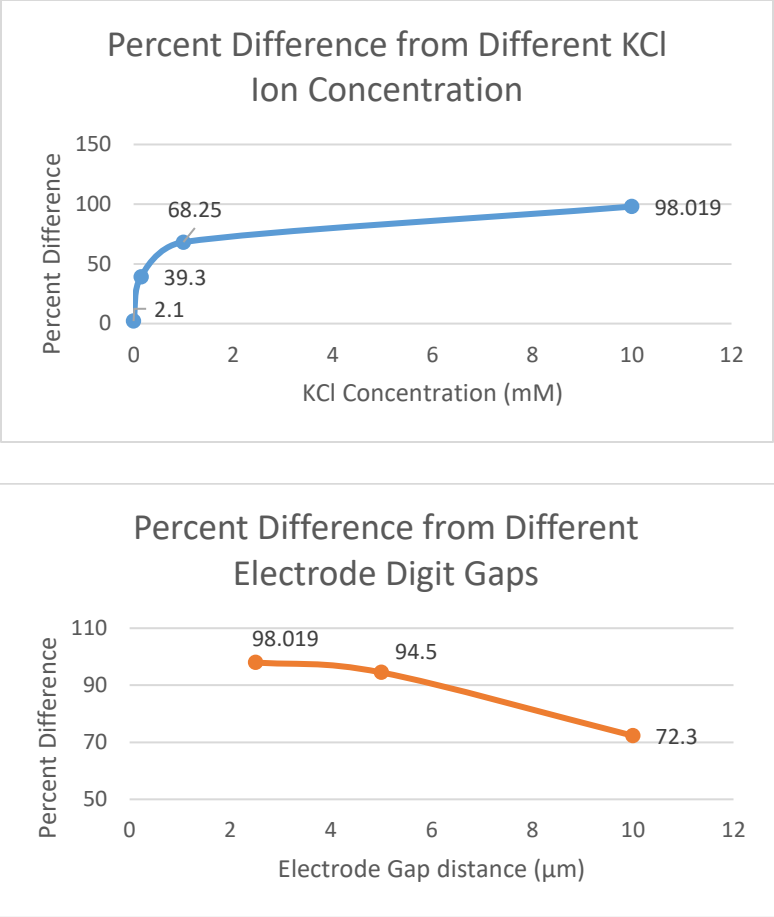

Figure 3.6: Simulation results of the percent difference in the electric field magnitude at the center of the gap between electrodes digits with and without 60 nm GNPs bound to the surface of the electrodes. GNPs are 20 nm above electrodes, 10 mM KCl concentration and 0.1 V DC applied to the electrodes. Top: the effect of different ion concentrations. Bottom: the effect of different gap sizes.

While maximizing the ion concentration would seem to be the best way to maximize sensitivity (as seen in Figure 3.6), there are practical limits to this. Increasing the concentration too much "washes out" any sensitivity, the conductivity of the ions dominates the measurements. The results of the changes in electrode gap size are consistent with many reported designs [51], [80], where the gaps between digits are as small as possible to increase sensitivity. There are diminishing returns however, with a change from 10 µm to 5 µm resulting in a change of around 30%, and a change of 5 µm to 2.5 µm only resulting in a change of around 4%. There are also practical limitations here as well. As the dimensions get smaller, more precise, and expensive,

fabrication techniques must be used. With these examples, it can be seen that these COMSOL simulations not only show this mechanism of detection, but also the simulations' usefulness in designing electrodes.

Simulations of this initially proposed detection method did show the establishment of electrical screening, the electric field profile surrounding IDEs, that gold nanoparticles bound to the electrode digits decrease the electric field magnitude between electrode digits, and the effect of different design conditions on the effect of nanoparticles. However, the simulations do not directly address why exactly the addition of nanoparticles changes the electrode impedance. As seen in the original proof-of-concept experiments, the addition of gold nanoparticles decreases the impedance of IDEs and simulations showed a decrease in electric field. Together, these indicate that the nanoparticles have an effect on the capacitance of the electrodes. IDEs are primarily just interdigitated capacitors [100]. Each adjacent pair of electrode digits can be thought of as parallel plate capacitors with the gap distance being the distance between two adjacent plates and the area of the plates being the length of digit overlap multiplied by the thickness of the electrode metal. In simple terms, the impedance magnitude is just:

$$|Z| = \sqrt{Z_{real}^2 + Z_{imaginary}^2} = \sqrt{R^2 + \left(\frac{1}{\omega C}\right)^2} \tag{3.10}$$

This impedance magnitude is a combination of the resistance (R) which is the contribution of conduction between electrode digits caused by free charges (like ions) in the buffer solution and the reactance which depends on the angular frequency (ω) and the capacitance (C). Although the actual capacitance of the IDEs is more complex [100], simplifying things as a parallel addition of a number of parallel plate capacitors shows how the capacitance is proportional to the thickness of the metal layer. The addition of gold nanoparticles essentially increases the height of the section of the digit they attach to, which in turn has the effect of increasing the capacitance of the electrode, thus decreasing the impedance magnitude.

Both simulations and early results show that this "first technique" of chemically attaching gold nanoparticles directly to electrode digits can cause measurable impedance changes, making it seemingly a viable technique for a biosensor platform. So, one may ask then what the necessity is for having a second technique. Despite the early success with the first technique there are a few key issues. These issues will be elaborated upon in future chapters, but in short, it is a problem of

sensitivity. It just takes too many bound nanoparticles in order cause a measurable impedance change. In order to be an effective quantitative biosensor, a biosensor must be able to discern between small changes in analyte concentrations. However, because the mechanism behind the first detection technique relies on bound nanoparticles having the bulk effect of changing the thickness of electrode digits, this effect does not change greatly with the addition or removal of a small number of nanoparticles. While this technique would work for qualitative detection (all or nothing results), or for large changes in concentration, it would most definitely not be suitable for the desired metabolomic applications.

3.4. COMSOL Simulations of Gold Nanoparticles Between Electrode Digits[3]

After the first technique was found to be lacking in terms of sensitivity, a new method of detecting nanoparticles using impedance. After some research and investigation, it was decided that it would be much more effective to attach nanoparticles between electrode digits rather than on top of them [94]. This seemingly minor change to the design actually can have a large impact on its performance and even fundamentally changes the mechanisms involved in changing an electrode's impedance.

To investigate this new technique, more complex COMSOL simulations were carried out. The previous simulations only considered the effect of a small area of an electrode. These new simulations consider a much larger area and calculates an impedance value per unit area of an electrode. The limitations on the initial electrode simulations were largely due to the added complexity of the simulations calculating the movement of ions to create the electric screening layers around the electrodes. Therefore, to get around this extra calculation load, the electric screening in the system was predefined.

There are several methods that have been previously investigated for simulating electric screening layers [101], [102], ranging from very basic to complex. The most simple of these is the Helmholtz model [103]. In this model, a single layer of ions with the opposite charge of a planar charged surface form. This leads to a capacitance per unit area of:

[3] A huge amount of appreciation goes to Peter Hermansen for his work on these simulations. I worked closely with him to develop the design of the electrodes and these simulations. He did the majority of the work on simulating GNPs bound between electrode digits.

$$C_H = \frac{\epsilon}{H} \tag{3.11}$$

Where ϵ is the dielectric constant, and H is the solvated radius of the ions. While simple, this model does not take into account the Debye length, or movement of the diffuse layer of ions.

The Gouy [104] and Chapman [105] model expands on the basic Helmholtz model by adding Maxwell-Boltzmann statistics to account for the distribution of diffuse ions. In this case, the derived capacitance per unit area for this model is:

$$C_{GC} = \frac{\epsilon}{\lambda_D}\cosh\frac{e\Phi}{k_B T} \tag{3.12}$$

Where Φ is the electric potential, e is the elementary charge, k_B is the Boltzmann constant, T is the temperature in Kelvin, and $\lambda_D = \sqrt{\frac{\epsilon k_B T}{4\pi e^2 c_0}}$ is the Debye length (c_0 is the molar concentration of the electrolyte).

The Stern model combines these two, treating the Helmholtz and Gouy-Chapman capacitances like capacitors in series [106]. The region around the electrode now consists of both a stationary Helmholtz layer at the surface, and the diffuse layer of ions defined in the Gouy-Chapman model. The new capacitance per unit area is therefore:

$$\frac{1}{C_S} = \frac{1}{C_H} + \frac{1}{C_{GC}} \tag{3.13}$$

There are even more complex models as well, incorporating additional ion layers [107], however for the purposes of these simulations, this extra complexity is not necessary. The final model chosen to be used in these simulations is actually the Gouy-Chapman model. In real-world applications, there's a practical limit to the ion concentration that can be used when taking measurements. If the ion concentration is too high the conductivity of the solution overwhelms any impedance changes caused by gold nanoparticles in the system. This restricts the buffer ion concentrations to relatively low values. At low ion concentrations, the contribution of the Gouy-Chapman capacitance to the Stern capacitance is much greater than the Helmholtz capacitance so $\frac{1}{C_S} \approx \frac{1}{C_{GC}}$ and in this case just the Gouy-Chapman model of the electric double layer can be used.

Taking into account the specific conditions of these simulations, a further simplified version of the Gouy-Chapman model was used.

$$C = \frac{\epsilon}{4\pi\lambda_D}\cosh\left(\frac{\phi_0}{2}\right)\frac{\sqrt{2}\left|\sinh\frac{\phi_0}{2}\right|}{\cosh\phi_0\sqrt{\ln(\cosh\phi_0)}} \tag{3.14}$$

Here, $\phi_0 = \frac{e\Phi}{k_B T}$. To simulate this the double layer is treated a layer of thickness λ_D, the permittivity of the layer material is set to be $\epsilon_{DL} = C * \lambda_D$.

In addition to double layer simulations, the bulk properties of the surrounding environment had to be simulated. This region was treated as a homogeneous solution of completely dissociated potassium chloride dissolved in water at 25ºC. From this the molar conductivity of the solution can be calculated using the Debye-Hückel-Onsager equation and the effect of the salt concentration on the dielectric constant [108].

As with the previous simulations, only a small area of the total electrode was simulated and the properties of the electrode were extrapolated from there. In this case, a single electrode pair was simulated. It was assumed that the effect of other electrode digits was negligible compared to the effect of the immediately adjacent digits. Several additional simulations were carried out to test and prove this assumption.

A simplified diagram of the simulation setup is seen in **Error! Reference source not found.**. The simulation is generally similar to the setup of the previous COMSOL simulations, with a 2D plane extended into 3D space. Again, this takes advantage of the symmetry of the system to greatly simplify the simulation. For these simulations, once the 2D simulation is carried out, the parameters found can be used to find the impedance of a full 3D situation using the equation:

$$\mathrm{Z} = \frac{v_{app}}{(N_e - 1)L_e\sqrt{J_x^2 + J_y^2}} \tag{3.15}$$

Here N_e is the number of electrodes, L_e the length of the electrodes, v_{app} is the amplitude of applied voltage, J_x and J_y are the current densities in the simulation plane. This equation assumes that the current density is constant along the length on the electrodes. This is a good approximation to make as long as $L_e$is far greater than the width of the electrodes or the distance between them (w_e and d_e).

Table 3.1. Simulation parameters

Parameter	**Description**	**Value**
N_e	Number of electrode digits	561
L_e	Length of electrodes	3.034 mm
h_w	Height of well	0.1mm
h_{BS}	Thickness of glass	0.1mm
w_e	Width of electrode	0.25µm - 16µm
h_e	Height of electrode	50nm
d_e	Distance between electrodes	0.25µm - 16µm
r_{GNP}	Radius of gold nanoparticle	30nm
d_{GNP}	Distance of gold nanoparticle from electrode	Dependent on gap size
ϵ_{BS}	Relative permittivity of the borosilicate glass	4.6
σ_{BS}	Conductivity of the borosilicate glass	2.5nS/m

Table 3.1. shows a description of the dimensions in the simulation setup (as shown in **Error! Reference source not found.**) as well as the values for these dimensions that were used for these simulations. Some of these dimensions were fixed for all simulations such as the number of electrode digits, length of the electrode digits, electrode height, and nanoparticle radius. The value of these parameters would not have a significant effect on the overall function of the

electrode, and their values were set based on early stage designs, initial experiments, and fabrication limitations. The parameters that were changed, such as the electrode digit width, and the distance between digits have a much more significant impact on the sensitivity of the electrode. These initial parameters were taken from prototype electrodes (such as number of digits) and others are known material properties.

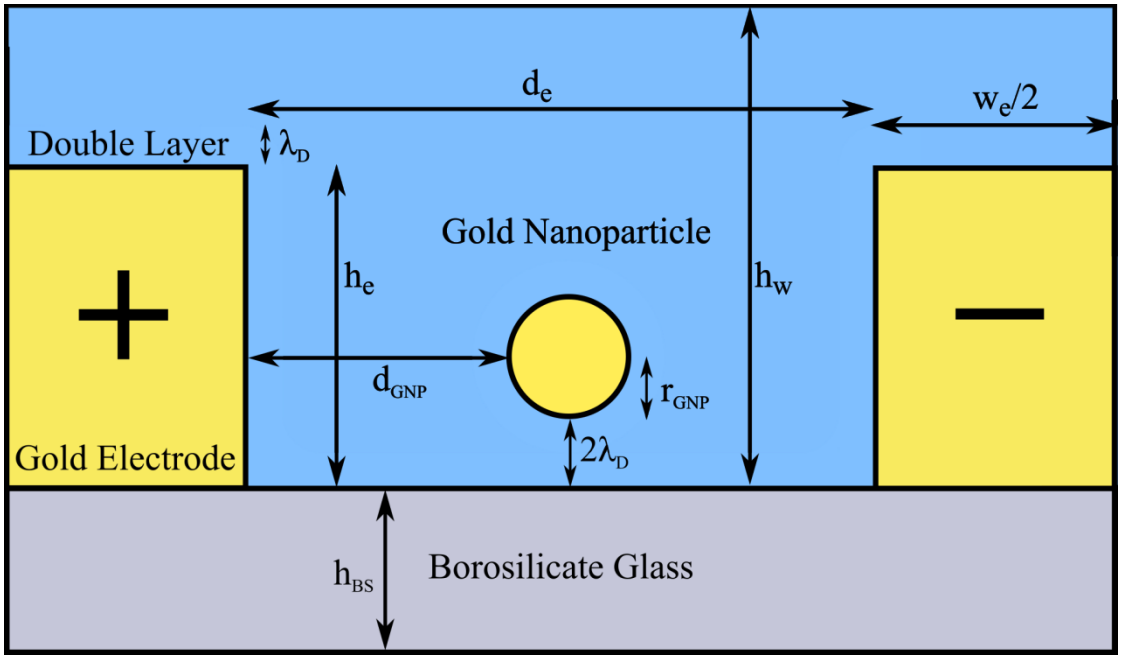

Figure 3.7: Basic diagram of the simulation setup, showing the electrode substrate, two adjacent electrode digits, a gold nanoparticle between those digits, and the electric double layer surrounding the system.

The value d_{GNP} describes the location of the gold nanoparticle between electrodes. Because the change in impedance is highly dependent on the location of the nanoparticle (the closer the nanoparticle is to the middle of the gap the less the change in impedance), all simulations were run 20 times with the gold nanoparticle in a different location each time. The equation used to describe this is:

$$d_{GNP} = 2 * \lambda_D + \frac{(n-1)(d_e - 2(r_{GNP} + \lambda_D) - \lambda_D)}{19} \tag{3.16}$$

Here *n* is a set of values ranging from 1 to 20. By running simulations for each value of n the system can be simulated with 20 different locations of the gold nanoparticle. This equation is set up such that the double layer formed on the electrodes does not overlap with the double layer on the nanoparticle.

With the simulation dimensions set and the electric screening layer defined, the next step was to define the physics that the Comsol simulation software would simulate. Using Comsol's electric currents module the electric field and electrical currents of the electrode system and the effects of nanoparticles on that system could be simulated. Comsol used three main equations to determine the current densities, electric displacement field, and electric field, all in the frequency domain. Boundary conditions were set such that all electrode digits only interact with adjacent digits (which has been shown to be a fair assumption). Frequency sweeps were based on limitations of existing equipment, ranging from 1Hz – 10MHz, with 20 frequencies simulated per decade.

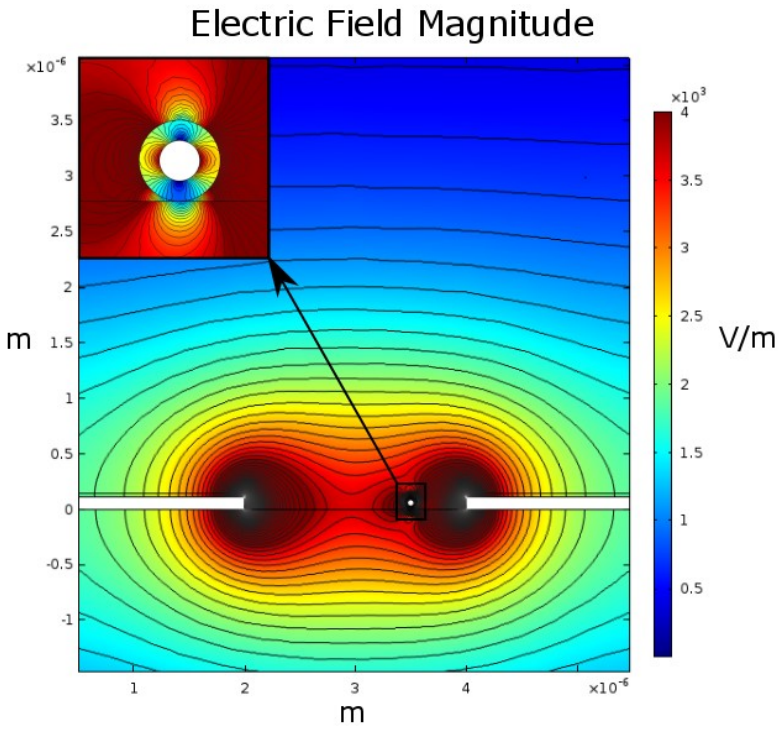

Figure 3.8: Surface plot electric field magnitude of electrodes with a gold nanoparticle.

Figure 3.8 shows simulation results of the electric field magnitude of two adjacent digits of an electrode with a bound gold nanoparticle between. The figure shows the areas where the

electric field is the strongest, how rapidly it dissipates away from the surface, and the disruption of this field caused by the nanoparticle.

The main purpose of these simulations is to weigh the effectiveness of different electrode configurations. This was done by evaluating the effect simulated nanoparticles had on the impedance response of electrodes. A value defined here as "responsiveness" was calculated as the percent difference in the impedance phase result between a bare simulated electrode and one with a bound gold nanoparticle.

$$R = \left|\frac{\theta_{no\ GNPs} - \theta_{GNPs}}{\theta_{no\ GNPs}}\right| * 100 \tag{3.17}$$

Where $\theta_{no\ GNPs}$ is the simulated impedance phase without gold nanoparticles present and $\theta_{GNPs}$is the impedance phase when gold nanoparticles are present. As seen in equation 3.17, this responsiveness value is directly related to the impedance effect that gold nanoparticles have on the electrode. The larger this value, the more sensitive the electrode is to changes caused by bound nanoparticles. It is important to note that these values are based on a simulation of a single nanoparticle, so they do not reflect any actual impedance values, but rather they serve as an indicator of electrode function (the intended purpose of these simulations).

3.4.1. Location of nanoparticle

The location of the bound gold nanoparticle relative to the electrode digits has an effect on the impedance change. A nanoparticle in the center of the gap between digits (and therefore the maximum distance away from the electrode) has a smaller effect on impedance than one right next to one of the digits. To demonstrate this effect, the simulation was run with a nanoparticle in 20 different positions between adjacent electrode digits and the responsiveness was calculated for each.

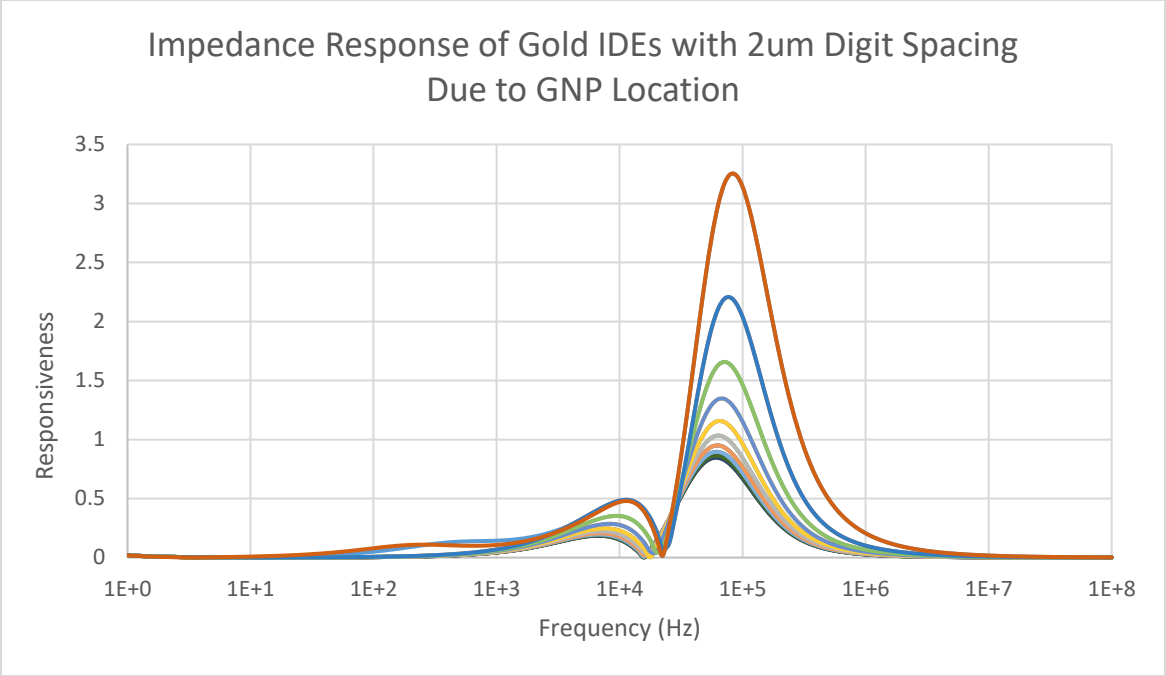

Figure 3.9: Impedance response depending on the location of the nanoparticles between electrode digits.

Figure 3.9 Shows the range of impedance response over the range of positions of a bound nanoparticle between electrode digits. There is a wide variation seen in impedance change based on the position. This could potentially be an issue if the system were to measure very small numbers of nanoparticles. If a single nanoparticle could contribute a range of impedance effects on an electrode, detecting sensitivity would suffer greatly. However, it is assumed that when many nanoparticles are bound to the surface, they will disperse evenly (i.e. no preferential binding across electrode gaps), resulting in an accumulated change at the average sensitivity value. It is also assumed that in this case nanoparticles would not aggregate together on the surface, but rather stay separate. Considering the intended application of this sensor system, and referring back to the list of metabolites in Table 1.1, for detecting small biological molecules, biologically relevant concentrations are generally in the range of μM, and changes in concentration that need to be detected are in the range of nM-μM. Assuming a 1nM concentration sensitivity is required, and assuming a relevant binding volume found by multiplying the surface area of an electrode (3mm x 3mm) by an approximate area over the electrode where metabolites in the sample will bind (around 10nm), an approximate minimum number of detectible GNPs can be calculated. Using these assumptions, a minimum of around 150000 GNPs would be the minimum detectible. Based

on the law of large numbers, given a random distribution and a sufficiently large sample size (150000 GNPs), the value converges on the mean. Therefore, though there is a large variation in the response caused by a single nanoparticle, a minimum measurable changes from the sensor will be consistent.

3.4.2. Impedance Response of Digit Gap Spacing

The next important factor to be considered is the size of the gap between adjacent electrode digits. Theoretically, the closer the gap size is to the detected element's size (e.g. several microns for detecting cells, or less than one micron for small molecules) the better the performance of the sensor. Therefore, the closer the gap size in this case is to the size of the nanoparticles, the better the performance should be. However, there are practical limitations to fabricating real electrodes with standard optical lithography techniques, limiting the minimum gap size. For simulating this, simulations were done for a range of gap sizes between 0.25 µm to 5.0 µm, all over a range of frequencies between 1Hz to 100MHz and for 20 different nanoparticle positions in the gap. In all cases the digit width to gap ratio was kept constant at 2:1, and an average nanoparticle coverage of 10% of the electrode area was used to adjust the impedance response.

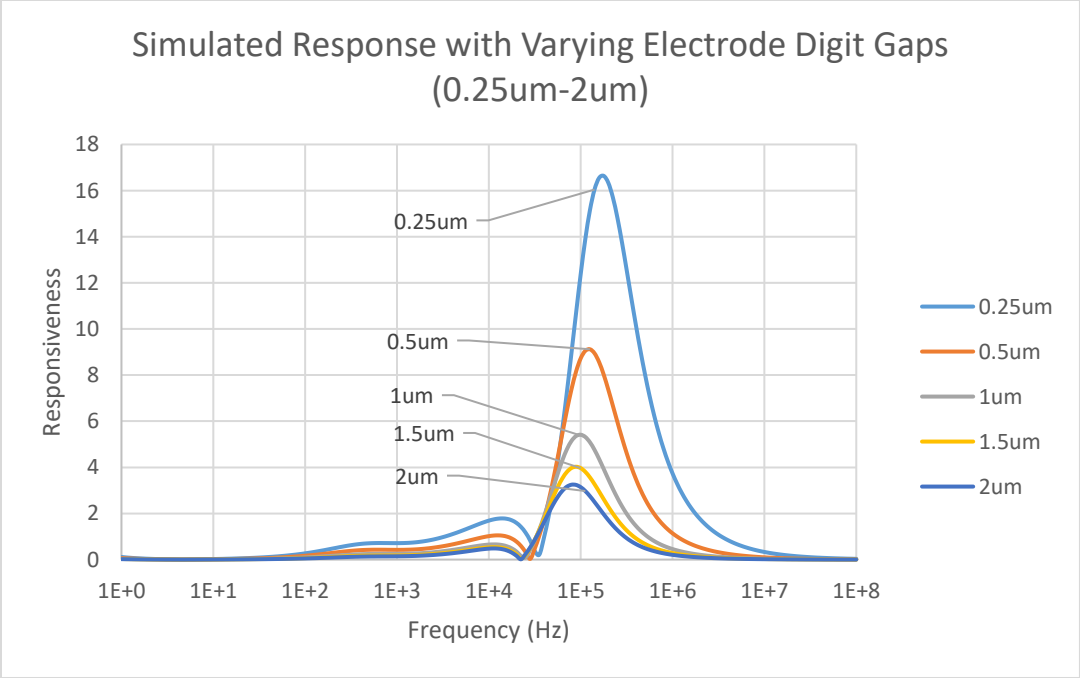

Figure 3.10: Plot of impedance response values over frequencies of 1Hz to 100MHz and electrode gap sizes ranging from 0.25 µm to 2 µm. The electrode digit width to gap ratio is kept at 2:1.

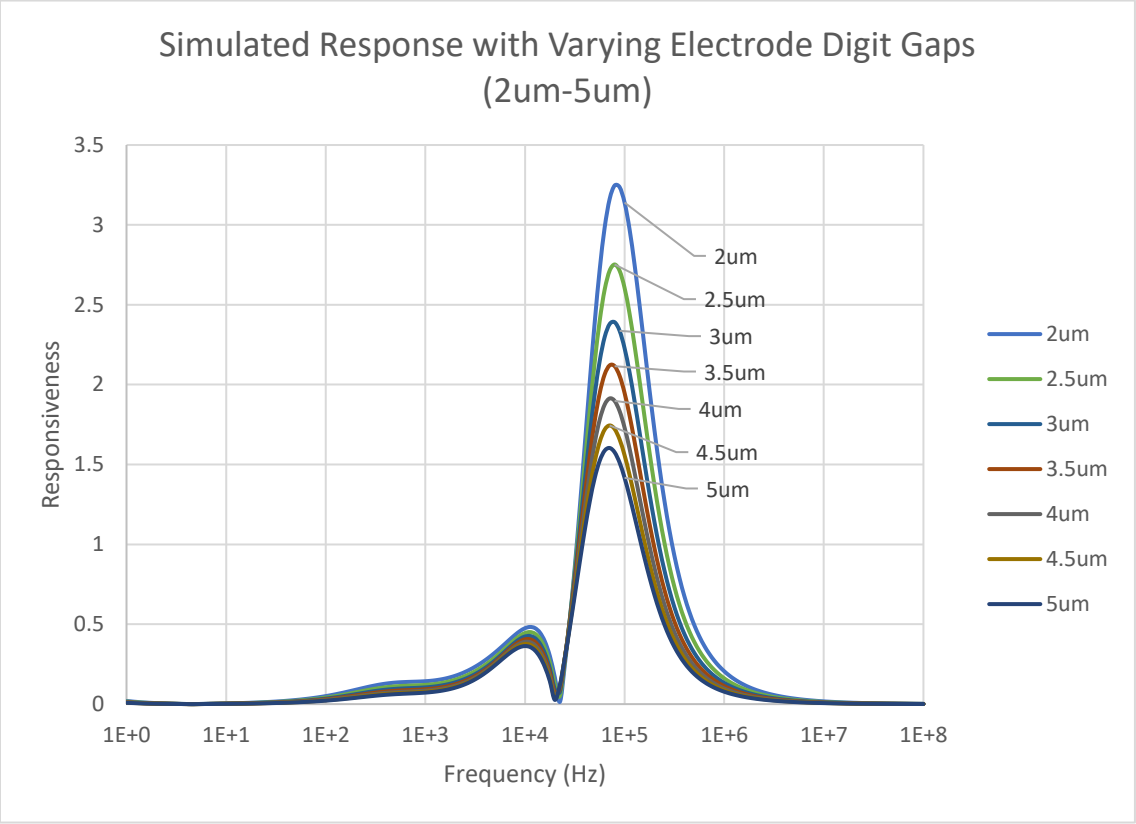

Figure 3.11: Plot of impedance response over frequencies of 1Hz to 100MHz and electrode gap sizes ranging from 2 µm to 5 µm. The electrode digit width to gap is kept at 2:1.

As predicted, the impedance response increases as gap size decreases. The frequency response is interesting as well. There is a consistent peak around 100 kHz.

3.4.3. Impedance Response of Gap to Digit Ratio

Next the effect of the gap to digit ratio was tested. In a similar way to the previous simulations with gap size, here simulations were done at a range of frequencies and nanoparticle positions, but this time keeping the gap size consistent at 2 µm and changing the ratio from 1:8 to 4:1.

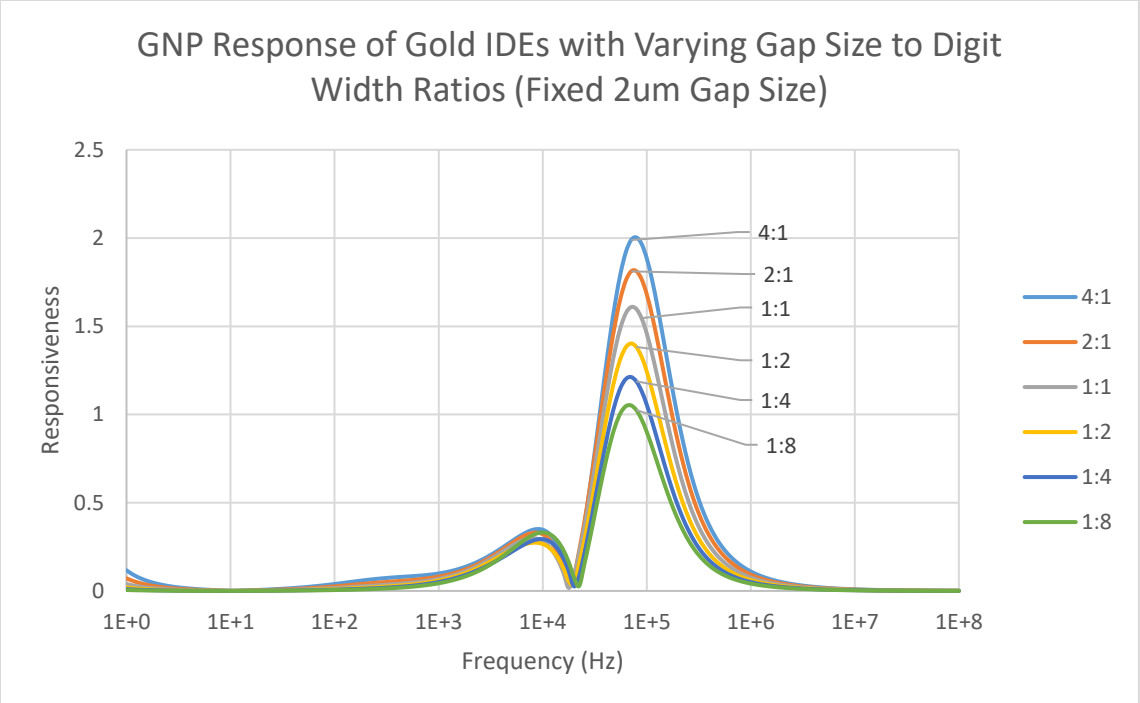

Figure 3.12: Impedance response of different gap to digit ratios with electrodes kept at a 2 µm gap size. There is one central peak in responsiveness centered around 100kHz for all gap sized, but overall the response increases as the gap size increases compared to the digit width.

Figure 3.12 shows that the peak frequency varies only slightly with varying gap to digit ratio. The impedance response does increase as the ratio increases. Putting this together with the gap size simulations, the ideal electrode dimensions would minimize the gap size, while keeping the digit width even smaller. Of course, with practical cost and fabrication constraints limiting the design parameters for the electrodes, these ideal characteristics have to be limited to what can be done affordably and reliably in making electrodes.

3.5. Considerations of Electrode Materials

All simulations so far have considered gold electrodes patterned on glass substrates. These are very common materials used for making biocompatible electrodes. Glass is electrically insulating, non-reactive, stable, and transparent (which is useful for characterization). Gold is famously biocompatible [69], [109], non-reactive so it doesn't oxidize or corrode easily, and can be easily modified using thiol chemistry [43], [71], [87], [110]–[112]. However, these materials

also present limitations and challenges. It can be difficult to pattern metals on glass, especially compared to other similar materials. Silicon dioxide grown on silicon wafers can be much easier to work with, and its structure can be easier to functionalize. And despite all the advantages of gold, its non-reactivity can make it difficult to pattern effectively while making electrodes, leading to more defects and forcing larger feature sizes. One alternative is aluminum, which is much easier to pattern using standard optical photolithography and wet etching techniques. Aluminum is more reactive than gold and forms a natural oxide layer on its surface, but this can actually be advantageous for this particular biosensor design. The changes in impedance for this design are largely from the capacitive contribution to the impedance, and the oxide layer around aluminum electrodes act as insulators blocking the resistive component (caused by conduction of ions in the surrounding buffer solution).

With these alternative materials in mind, further simulations were done comparing gold electrodes on glass substrates to aluminum electrodes on silicon dioxide. For simulations with aluminum electrodes, an extra layer of 1nm aluminum oxide was simulated on the surface of the aluminum, and a 0.5 μm thermally grown silicon oxide layer on a silicon substrate was used.

Table 3.2: Simulation parameters for aluminum electrodes on oxide

Property	**Description**	**Value**
ϵ_{Si}	Relative permittivity of silicon	11.68
σ_{Si}	Conductivity of silicon	435μS/m
ϵ_{SiO_2}	Relative permittivity of silicon dioxide	3.9
σ_{SiO_2}	Conductivity of silicon dioxide	10pS/m
$\epsilon_{Al_3O_2}$	Relative permittivity of aluminum (III) oxide	9.34
$\sigma_{Al_3O_2}$	Conductivity of aluminum (III) oxide	5pS/m

Table 3.2 describes the extra parameters associated with aluminum electrodes on silicon dioxide substrates. Simulations were done with 2 µm digit gap, a 1:2 gap to digit ratio, and 10% gold nanoparticle area coverage in the gap. Like other simulations, simulations were run for each frequency from 1Hz to 100MHz with twenty frequencies simulated per decade. For each frequency twenty different simulations were run corresponding to possible gold nanoparticle locations in the gap. These were carried out for both the original gold electrodes and with the new parameters of the aluminum electrodes. The impedance magnitude and phase for each were compared as well as their sensitivities to gold nanoparticles.

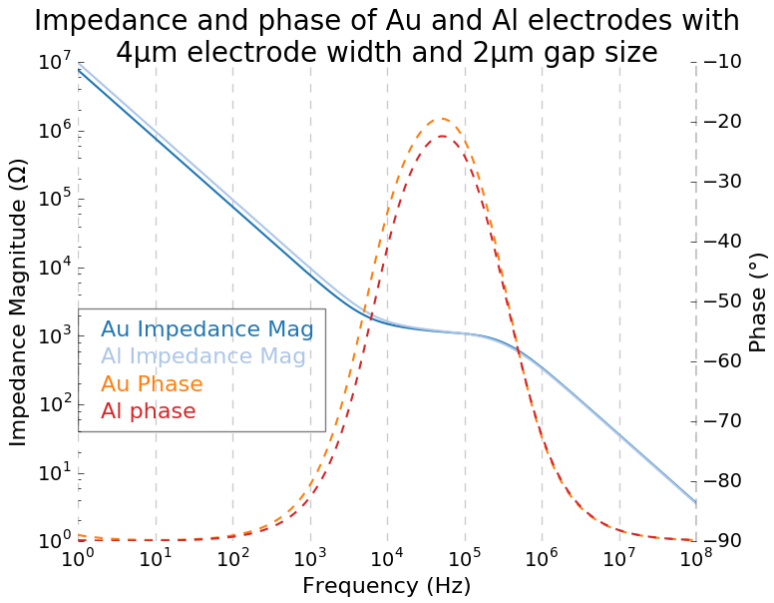

Figure 3.13: Simulated impedance phase and magnitude of aluminum and gold electrodes. This behaviour matches both the theoretical impedance curves for a non-faradaic two electrode system and for real measurements on IDEs.

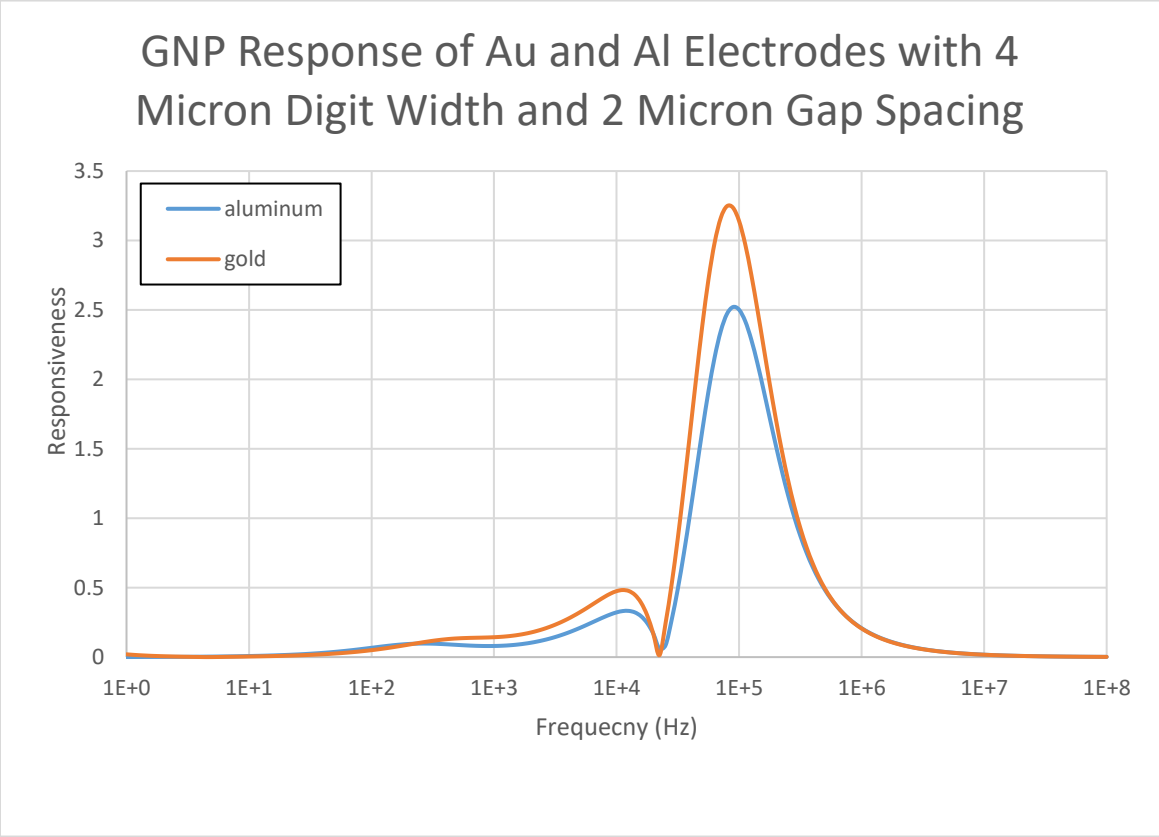

Figure 3.14: Simulated impedance response of aluminum and gold electrodes to bound gold nanoparticles. The general trend for both materials is the same with the same peak frequency, but the gold electrode has a higher response than the aluminum.

While there is a slightly greater response with the gold electrodes (peak response of 3.3% for gold versus % for aluminum), both simulations show that the electrodes behave very similarly. Therefore, practical fabrication considerations, as well as the best designs for accommodating biological and chemical components can be used when choosing the proper materials to use.

3.6. Electrode Fabrication

From early proof-of-concept experiments to a working biosensor device, there have been many iterations of electrodes used. These have included proprietary electrodes made for existing sensor systems, individual, single use conductivity sensors, screen-printed electrodes on plastic,

electrodes based on modifications made to existing designs, and finally completely original designs.

As discussed in previous chapters, initial experiments were done on the RT-CES cell counting system. This system comes complete with its own gold interdigitated electrodes, custom made for that device's intended application of counting cell growth. As such, these electrodes are gold interdigitated electrodes patterned on glass treated for adherent cell growth. The dimensions of the electrode gaps and digits are therefore appropriately sized for this application, meaning they are comparable in size to the cells they are designed to detect. These are much larger than ideal dimensions for detection gold nanoparticles, and although it has been shown that it is possible (as seen in Chapter 2) for these electrodes to detect bound nanoparticles, the setup is far from ideal.

The next two iterations of the electrodes were both interdigitated gold screen printed electrodes purchased from BVT Technologies and Applied Biophysics Incorporated. While their dimensions are both significantly larger than the RT-CES plates, their electrical connections and materials were easier to manage and control making them useful for early testing of impedance measurements and comparisons between impedance measurement systems (see Chapter 5 for more information on impedance measuring).

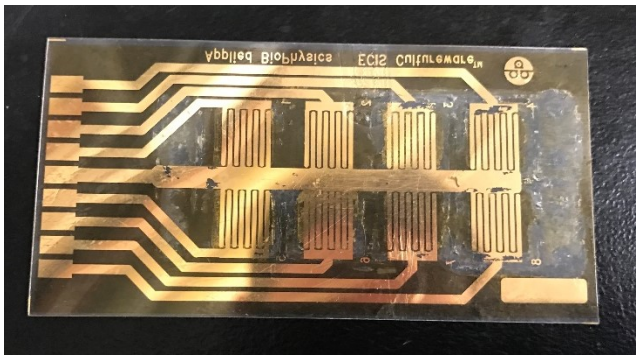

Figure 3.15: An Applied Biophysics Inc. sensor chip. This sensor chip has eight interdigitated electrodes made of printed gold on clear plastic. The electrode digits are very large with visible gaps between them.

While there are many interdigitated electrodes available for purchase for a number of different applications (from DropSens, Applied Biophysics Inc., and others), including the ones described above, there were none that fit the exact parameters that were required for this biosensor

design. Therefore, custom microfabricated sensor electrodes were designed. Designs were based on the overall footprint of the Applied Biophysics Inc. except with the electrode digits being much smaller and much closer together (resulting in many more electrode digits overall). Original mask files were obtained directly from Applied Biophysics Inc. and were modified using Klayout GDS editing software. A five-inch photomask was then created using the services provided by the University of Alberta Nanofab facilities.

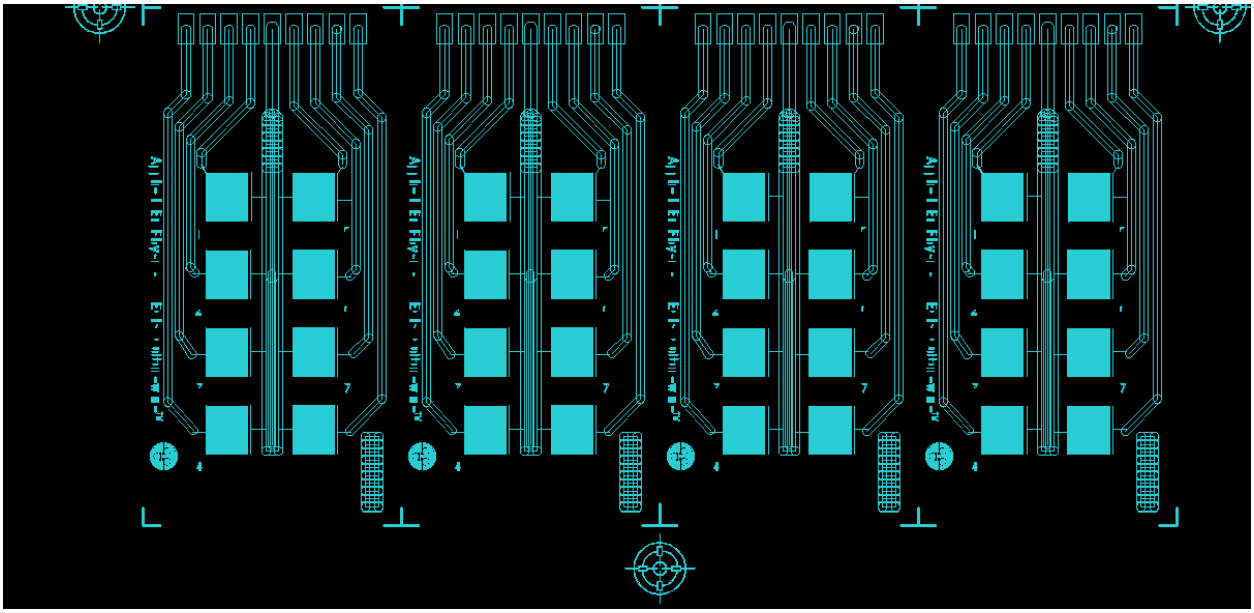

Figure 3.16: A portion of the mask design of the first series of microfabricated electrode chips (Electrodes A and B from Table 3.3).

Electrodes were then fabricated using standard photolithographic techniques on four inch square borofloat glass substrates[4]. A 100nm gold layer was deposited on the glass with a 10nm chromium adhesion layer in between to keep the gold attached to the glass substrate. After photoresist deposition and patterning using the mask, the gold and chromium were etched using a wet etch. After this, the electrode chips were diced into individual chips (with eight individual electrodes on a single chip) and cleaned.

[4] These first designs were fabricated by Tushar Biswas, a graduate student in another group working on the CRIO Tricorder project.

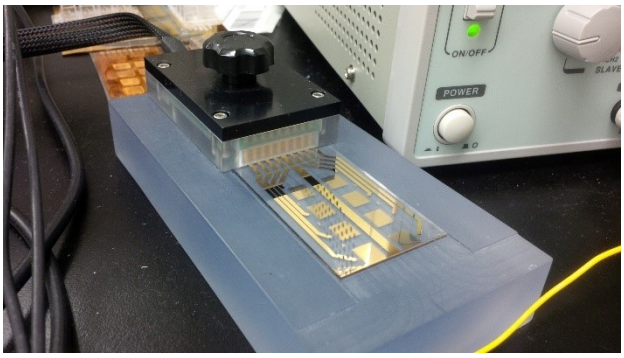

Figure 3.17: An electrode chip (Electrode A from Table 3.3) connected for impedance measurements. This electrode chip has eight electrodes on it with 20 µm digits with 10 µm spacing between adjacent digits. The electrodes are made of gold printed on a glass substrate. The chip is connected to a series of pins using a connector screwed into a base. This connector allows the chip to be easily connected to an impedance meter.

There were two different configurations of electrodes that were made using this mask. One with 20 µm digit width and 10 µm spacing between digits (Electrode A from Table 3.3), and another with 10 µm digit with and 5 µm spacing (Electrode B from Table 3.3). While simulations show that minimizing digit spacing would result in optimal performance, there were potential limitations from the photolithography and wet etching, thus the larger spacing. Testing of these electrodes did show that they performed as expected mostly (more on this in future chapters). There were some failures including over etched electrodes, and under etched electrodes, leading to short circuits on the electrodes, especially with those with smaller dimensions.

In the next iteration of electrodes, the main goals were minimizing cost, improving yield, and improving sensitivity. This was accomplished in two main ways: making all of the dimensions of the electrode chips smaller, and further decreasing the digit with and spacing of the interdigitated electrodes themselves. An entirely new mask layout was designed, this time with much smaller chips so that more could fit onto a single wafer, this time with six chips on each wafer, as opposed to just two before, significantly decreasing the price per electrode. Additionally, the surface area of the electrode pads was also significantly decreased. This serves to not only decrease the overall size of the chip, but also decreases the likelihood of defects on each electrode. With these changes along with refinements to the fabrication process, the dimensions of the electrodes were made even smaller, now down to 4 µm digit width and 2 µm gap spacing between digits. With even more

electrodes on this design, one entire chip on the mask was designed with different dimensions including 4 µm digits with 4 µm gaps, 2 µm digits with 2 µm gaps, 4 µm digits with 1µm gaps, and 2 µm digits with 1 µm gaps. The purpose of these electrodes was to test the limits of the fabrication techniques used and to compare their performance to the standard electrodes. The smaller gap sizes usually did cause short circuiting and the smaller digit sizes could lead to problems with over etching removing them completely. However, with the right amount of intentional over etching, some working electrodes were created with these alternatively sized electrodes.[5]

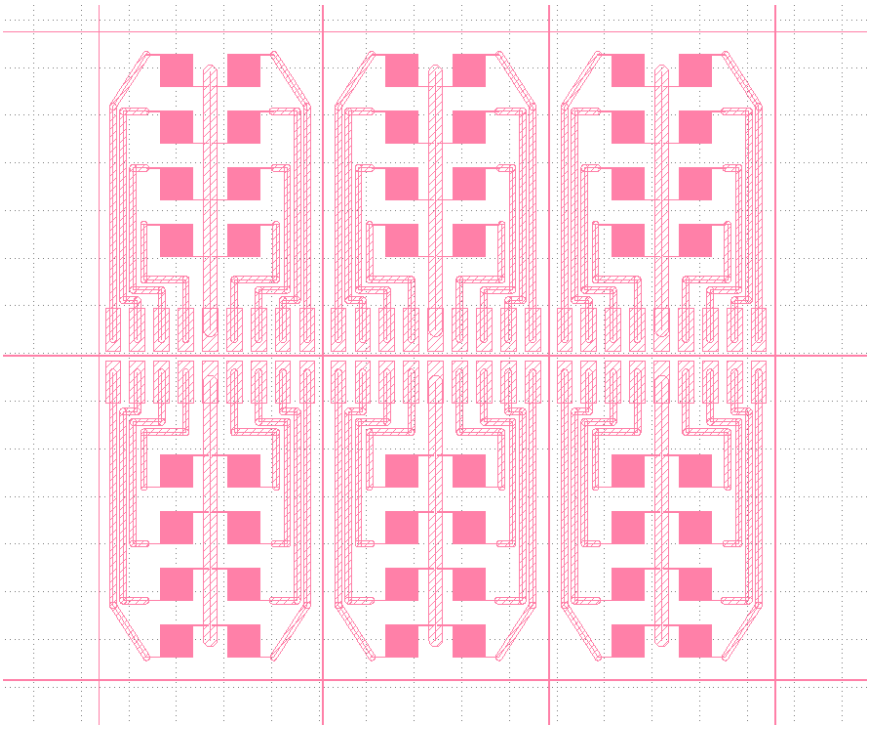

Figure 3.18: Mask layout for the smaller electrode chips (Electrodes C, D, and E from Table 3.3).

[5] While I designed the electrodes, fabrication was done in the ECE Nanofab both by nanofab staff, and by other members of the lab group. My appreciation goes to Gaser Negah and Ryan Corpuz for making some of these chips I designed.

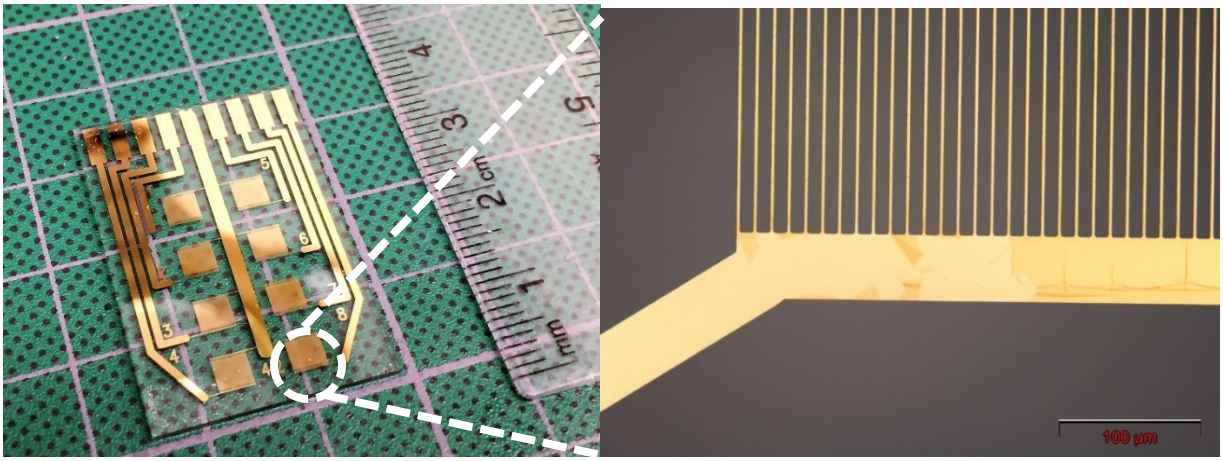

Figure 3.19: Left: Gold microfabricated electrode chip on a glass substrate (Electrode C from Table 3.3). Each IDE is designed with 4 µm digits with 2 µm spacing between digits. Right: a closeup image the side of one of the gold IDEs taken with an optical microscope. This image shows one side of the electrode digits (no interlocking digits are visible here).

The use of glass substrates did make imaging and characterization of the electrodes easier, but they lead to low yields and fabrication errors. Gold wouldn't adhere properly to the glass, and the thickness of the glass wafer would vary over the surface. Therefore, silicon dioxide was used for new substrates. Silicon wafers with 0.5 µm thermal oxide were used as substrates for new batches of electrodes. With these substrates, metal adhesion is more consistent and electrode yield and quality are higher. There are additional advantages in the ease of surface chemistry and interactions on silicon dioxide compared to borosilicate glass (more on that in the next chapter). One disadvantage of using silicon dioxide is that it is not as insulating as glass substrates, leading to a less capacitive impedance profile for the electrodes. Overall, the advantages in fabrication are greater than the disadvantages in measurements.

Additionally, as discussed previously, aluminum electrodes have also been made. In contrast to gold electrodes, aluminum electrodes are easier to fabricate with higher yields. Aluminum patterning is more standardized with no adhesion layer required and better controlled etching with wet etching techniques. Additionally, the aluminum oxide layer that forms on the electrodes insulates the electrodes making impedance measurements more capacitive (and therefore more sensitive to detecting nanoparticles). There are some issues however with reactivity

as salt solutions, buffers and biological samples can dissolve aluminum oxide and can even damage the electrodes.

Figure 3.20: Left: Aluminum electrodes patterned on silicon dioxide (Electrode D in Table 3.3). The majority of the electrode chips have dimensions of 4 µm wide electrode digits with 2 µm gaps between digits. The chip in the bottom centre has multiple configurations of electrode dimensions for testing purposes. Right: Another electrode design (Electrode F in Table 3.3). Gold electrodes printed on silicon dioxide. Each electrode is approximately one third of the size of the previous iteration with smaller dimensions (5 µm digits with 1 µm gaps between digits).

Table 3.3 shows an overview of several of the major iterations of fabricated electrode chips including the materials used to make the chips and the key dimensions of the interdigitated electrodes. Each of these configurations has been given a label (A-F) to refer to them and distinguish between them in this and other chapters.

Table 3.3. Electrode Configurations

Electrode Configuration	Materials	Electrode size (total surface area)	Number of Electrode Pairs	Electrode Digit Width	Electrode Gap Width
A	Gold on glass	7 mm x 7 mm	140	20 µm	10 µm
B	Gold on glass	7 mm x 7 mm	280	10 µm	5 µm
C	Gold on glass	3.4 mm x 3.4 mm	340	4 µm	2 µm

D	Aluminum on silicon dioxide	3.4 mm x 3.4 mm	340	4 µm	2 µm
E	Gold on silicon dioxide	3.4 mm x 3.4 mm	340	4 µm	2 µm
F	Gold on silicon dioxide	2.3 mm x 1.5 mm	210	5 µm	1 µm

3.7. Conclusion

As the design of the biosensor system has evolved, the design of the interdigitated electrodes has also changed and improved. Starting with electrodes with different intended uses, new and better suited electrodes have been designed, fabricated and tested. Simulations of the electrical properties of different electrode designs have not only revealed new and better mechanisms for detecting bound gold nanoparticles by changing how and where nanoparticles are bound to the electrodes, but these simulations also inform the electrode designs themselves. Choices of electrode dimensions and testing conditions were made based on the results of simulations, resulting in intelligent prototyping investments and electrodes best suited for the biosensor system.

However, the current iteration of these interdigitated electrodes is still in an early stage and are not perfect. The fabrication techniques used can be better suited to fabricating smaller digits and closer gap distances. The fabrication techniques currently available, particularly the use of wet etching, limit the dimensions and lower the yield of devices. One problem regularly encountered is over etching, causing gaps to be widened and digits to be smaller, or eroded completely. Other failure modes come from the chrome adhesion layer on the gold electrodes becoming etched away leading to gold that is not stuck to the substrate (often resulting in digits falling off the electrodes, or shorting out). The actual design of the electrodes themselves can also be improved in future iterations. In addition to further reducing the gap and digit sizes (as indicated by the previous simulations), the area of the electrode pads can also be reduced. The actual amount of digit overlap and number of digits in the electrodes do not have a major impact on sensitivity based on simulations, so decreasing the surface are of the electrodes can cut down on potential fabrication

errors, save substrate space (leading to decreased fabrication costs per electrode), and overall help miniaturize the device. Additionally, once fluidic channels are added to the system, the shape of the electrodes should likely be changed to better accommodate fluid flow.

With the detection method simulated and actual electrodes made, the logical next step is to confirm these simulations. This testing and confirmation involves measuring the impedance of electrodes over a range of frequencies, input voltages, and measurement buffers. Testing sensitivity to nanoparticles presents more of a challenge. Nanoparticles had to be attached to electrodes (both tests with nanoparticles attached on electrode digits and between electrode digits) by various means as well as biological recognition elements like DNA, antibodies and other proteins. The next chapter focuses on chemically modifying electrodes, attaching nanoparticles, characterizing surface chemistry, and testing the effectiveness of these electrodes using impedance measurements.

Chapter 4 : Chemistry and Impedance

4.1.Introduction

So far in the course of this biosensor design proof-of-concept experiments have shown that gold nanoparticles can be used to detect biological molecules using impedance changes on interdigitated electrodes. Next, simulations have been used to find a more effective detection method in attaching nanoparticles between electrode digits. Then, based on these simulations, electrodes were made. The next step is chemically modifying electrodes and nanoparticles for attaching molecular recognition elements for biomolecule detection. This is a vital step for the final implementation of the device as well as basic validation of the design, simulations and detection technique in general. To accomplish this, there were several necessary preliminary steps, intermediary setups, and independent validations required. The approaches for chemical binding have varied widely depending on the intended biomolecules, nanoparticles, and final placement on the electrodes.

In the earliest proof-of-concept experiments involved attaching molecular recognition elements to gold on the electrodes and gold nanoparticles. As such, the chemistry is basically the same for all gold surfaces. In later designs, where MREs are attached between electrode digits on the substrate, new and different binding strategies had to be used. These strategies often involved adding layers of chemical modification onto the electrode (both on the metal electrode digits and on electrode substrates) which could encourage or hinder specific binding. With multiple steps and multiple layers required to facilitate MRE modification, proper technique, consistency, and importantly, characterization was necessary. Characterization was employed in a number of different forms such as imaging using fluorescent imaging, scanning electron microscopy (SEM), or atomic force microscopy (AFM) to check for modification coverage or efficiency, and chemical characterization with techniques like X-ray photoelectron spectroscopy (XPS) or Fourier transform infrared spectroscopy (FTIR) to confirm the exact chemical composition of modifications.

In addition to this biosensor there are many other examples in biological sciences of immobilizing biological molecules to surfaces. Bound antibodies can be used for enzyme-linked immunosorbent assays (ELISA) in identifying proteins [113], [114]. Surfaces are treated with

proteins and polymers to allow for cell cultures to grow on them [115], [116]. DNA sequences are bound to substrates for DNA sequencing [117]. Different applications require different biological molecules, substrates, and chemical linkers.

4.2. Nanoparticles

As discussed in previous chapters, the use of signal enhancing gold nanoparticles is vital for this biosensor design. While bound biomolecules could potentially be enough to cause an impedance change on interdigitated electrodes [118] depending on the molecule size, charged functional groups and the electrode dimensions, the purpose of attaching gold nanoparticles is to provide a much larger change in impedance than can be caused by biomolecules alone, as well as providing a more consistent change independent of the type of biomolecule detected.

In Chapter 2 the specific role of nanoparticles was investigated in simulations. Briefly, gold nanoparticles bound between electrode digits in a buffer solution form a double layer which acts as a capacitor. This capacitance influences the electric field between electrode digits, thus raising the overall measured impedance. Further simulations showed that overall the size of the nanoparticles does not have a significant impact on impedance change. Therefore, the choice of nanoparticle size should be determined by what would work best for binding, chemical modification and stability.

4.2.1. Effect of Bare Gold Nanoparticles in Solution

In one early proof-of-concept experiment, gold nanoparticles suspended in solution were deposited on electrodes and that impedance was compared to solution alone. The idea here is that some of the nanoparticles in solution will be between electrode digits, thus causing intended effect on impedance (interfering with the electric field there) without having to bind the nanoparticles directly to the electrodes. There are of course some issues with this design, no guarantee of the exact number or concentration of nanoparticles between digits, or the placement of the nanoparticles over the electrodes, but the purpose here was to see the effect of nanoparticles, and show that it does indeed match the simulation results while not complicating the setup with chemical modification and binding. For this experiment, 30nm diameter spherical nanoparticles purchased from Cytodiagnostics (www.cytodiagnostics.com) were used. These nanoparticles were created using the citrate reduction method [119], [120] and were therefore citrate stabilized (which

provide a surface charge on the nanoparticles). Measuring the impedance of the nanoparticles as is would not be useful, as the surrounding solution that stabilizes the nanoparticles is too salty for measurements. That is, the ion concentration of the solution is too conductive, thus any impedance measurements will only reflect that conductivity and not the effect of the nanoparticles. Thus, the nanoparticles had to be suspended in a less concentrated salt solution. To do this 1 mL of nanoparticles ($1.79*10^{11}$ nanoparticles per mL) in the original solution were spun down in a centrifuge and washed three times with 150 µM KCl before being suspended in 1mL of 150 µM KCl. A gold IDE chip with 20 µm digit width and 10 µm gap spacing was used for experiments (Electrode A from Table 3.3). First, 50 µL of 150 µM KCl solution was put on the electrodes and the impedance phase and magnitudes of the electrodes were measured between 1 KHz and 100 KHz using a Gamry 500 Electrochemical Measuring Station.

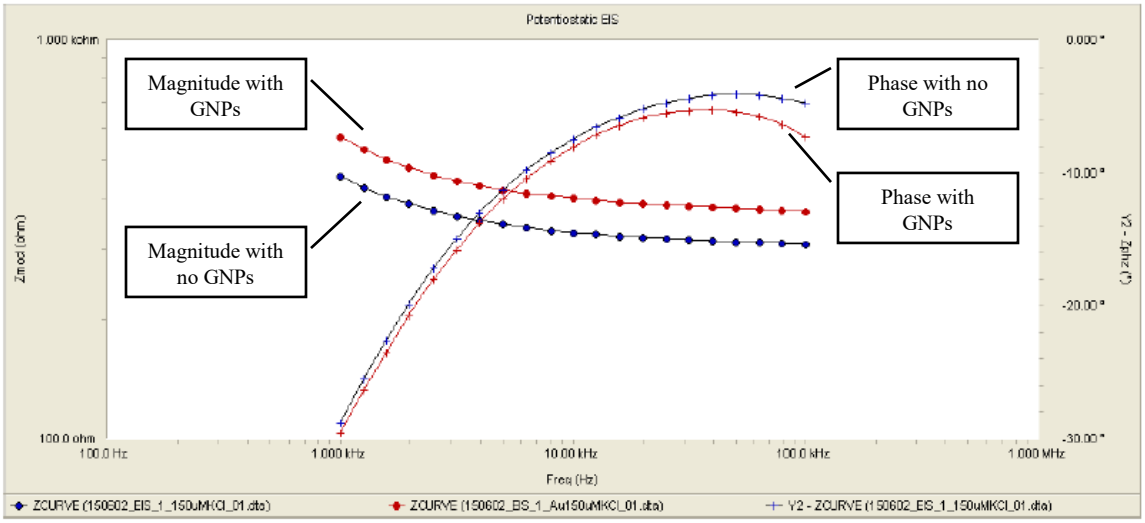

Figure 4.1: Graph comparing impedance phase and magnitude measurements over a range of frequencies (1 kHz – 100 kHz) for interdigitated electrodes (Electrode A from Table 3.3) in a 150 µM KCl solution (blue line) and suspended 30nm diameter gold nanoparticles in 150 µM KCl solution (red line).

The results here show that the presence of gold nanoparticles alone in solution cause a measurable change in the measured impedance magnitude. These results are also consistent with the prior simulations as the nanoparticles caused an increase in the impedance magnitude over the measured frequency range.

4.2.2. Gold Nanoparticle Synthesis and Modification

In addition to the 30nm and 60nm gold nanoparticles, smaller, 16nm diameter gold nanoparticles were made in our lab. These nanoparticles were made by a standard sodium citrate method [119], [120]. The size average and distribution was measured using optical density, zeta potential, and transmission electron microscope (TEM) imaging[6]. These tests determined that the average diameter was 16nm with a narrow variation in diameter. The 30 and 60 nm diameter electrodes were used for early experiments, including all tests with the RT-CES, suspended nanoparticles, and nanoparticles bound to the gold digits on the fabricated electrode chips. The smaller lab-made nanoparticles were used for all testing and modifications related to attaching nanoparticles to electrode substrates.

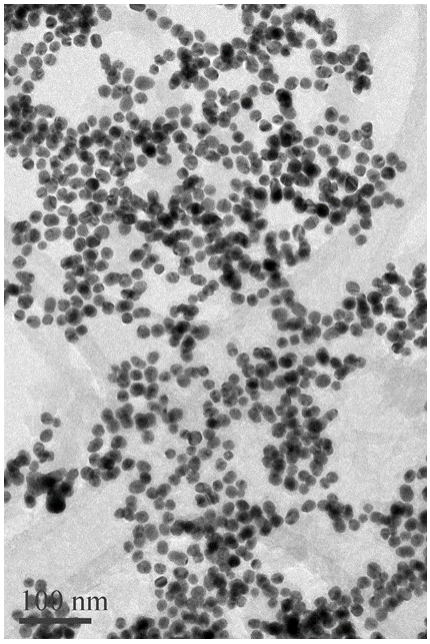

Figure 4.2: TEM image of gold nanoparticles modified and used in biosensor experiments. The nanoparticles are approximately 16 nm in diameter. (Scale bar in the bottom corner denotes 100nm)

[6] Thanks to Donghai Lin and Gaser Nagah for characterizing the nanoparticles and taking the TEM image shown in Figure 4.2

In the course of biosensor experiments, gold nanoparticles were modified in many ways with different chemicals, surfactants, stabilizers, biomarkers, fluorescent tags, DNA, and molecular recognition elements. In almost all cases thiol modification was used [121]. Gold readily forms bonds with sulfur (forming a thiol bond), so almost any small molecule modified with a sulfur group can be attached to nanoparticles. Regardless of what was being attached to the nanoparticles, the general procedure was basically the same. Thiol terminated modifiers (e.g. DNA with terminal thiol groups, or polyethylene glycol with an attached thiol group) suspended in water were added to nanoparticles in suspended in citrate solutions. Though the amounts of these varied depending on the modification, in most cases much more modifiers are used than nanoparticles, ensuring multiple modifiers are attached to each nanoparticle. In some cases, two or more types of modifiers were used, such as stabilizers to keep nanoparticles suspended in solution along with DNA for molecular recognition. In order to prepare the thiol groups for binding to the gold, TCEP, a reducing agent, was used. A small amount of TCEP (with about a 3:1 molar ratio of TCEP to thiols) was added along with the GNPs. After mixing and allowing time (several hours) for the reducing agent to react and for the thiols to bind to the gold, the solution is spun down in a centrifuge. Centrifugation separates the modified nanoparticles out of the surrounding solution, which can be removed and replaced with water or low salt buffers. The centrifugation is repeated three times to ensure all of the unbound modifiers, reagents, and citrate buffer are removed. After modification, the nanoparticles can be used on the biosensor, or they can be tested using techniques such as optical density or zeta potential measurements to confirm successful modification.

4.3. Impedance Measurements

It is important at this point to take a slight detour and provide some explanation of how exactly the impedance of electrodes is measured. Over the course of design and testing of the system this has been accomplished many ways, from simple measurements using a handheld impedance meter, to the final biosensor device. As described previously, the RT-CES cell counting system was used for initial proof-of-concept experiments, and while it does measure impedance, it only presents its data as a “cell index” value. This reflects changes in impedance, but not the intricacies of the measurement. Important information like the input voltage and frequencies, as well as exact phase and magnitudes were missing. Next the handheld LCR meter (from Agilent) was used for subsequent tests. This inexpensive device, as the name suggests, is capable of

measuring inductance, capacitance, and resistance, and functions in a similar way to a multimeter. The LCR meter has a small set output voltage, and discrete output frequencies ranging from DC up to 100 kHz. It was very useful in discovering more about the exact impedance ranges of electrodes and the most effective frequencies at which to measure impedances. There are still some significant disadvantages to exclusively using an LCR meter for impedance measurements. These include the inability to record impedance measurements over time or measure impedances at a range of frequencies.

For more detailed impedance measurements, electrochemical potentiostats were used. These tabletop electrochemical analysis stations are capable to measuring a wide range of impedances with a high degree of control over input characteristics and how information is displayed. These devices are useful for electrochemical measurements and characterizing thin films among many more diverse applications [122], [123]. For the purposes of this biosensor design, impedance phase and magnitudes are measured over a range of frequencies. These devices also allow for data analysis and comparisons between measurements making electrode characterization much easier.

While potentiostats are invaluably useful for testing electrodes, characterizing surface chemistry, and defining design parameters required for the biosensor device, they are far from ideal as an inexpensive, portable biosensor device. Standard potentiostats are tabletop devices that require a computer to operate, and can cost on their own between $10000-$50000. It is still necessary then to “strip down” the unneeded aspects, and simplify the required elements to create the desired biosensor (more on this in the next chapter).

4.4. Gold Electrode Binding

Binding gold nanoparticles to gold substrates is a popular technique in biosensor design [88], [124]. The main reasons for this are the biocompatibility of gold and the simplicity of using the same thiol binding scheme for both substrate and nanoparticles. It is this simplicity that initially inspired early designs that bound gold nanoparticles directly to gold electrode digits on our IDEs (as opposed to between them in later designs). This way the same thiol binding techniques that attached MREs or biomolecules to modified gold nanoparticles could be used to attach capture agents. As with GNP modification, molecules with thiol groups can be attached to gold electrodes

by covering the electrodes in a solution of the modifying molecules along with an appropriate reducing agent (again, TCEP just like for nanoparticles). After modification, electrodes are washed with water and sonicated (submerged in ultrasonically vibrating water) to remove and wash away any unbound molecules and clear off remaining reducing agent. This technique was used for early proof-of-concept results (as discussed in Chapter 2), and for tests involving short complementary strands of DNA.

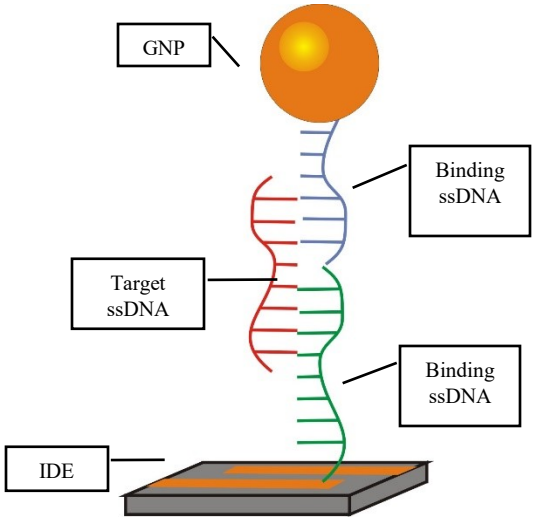

Figure 4.3: One possible configuration for detecting DNA. A sample containing the target DNA (red sequence) is complementary to part of a strand on the electrode surface (green strand) and part of a strand on modified GNPs (blue strand). This binds the nanoparticles to the electrodes for detection.

4.4.1. Poly-A/Poly-T DNA Experiments

(Note: These early proof-of-concept DNA experiments were briefly covered in Chapter 2.)

In early experiments with alternative electrodes, either adapted conductivity sensors from BVT technologies, or the first generation of our own fabricated electrodes, short, highly complementary strands of DNA were used for linking GNPs directly to electrodes without a biological intermediary between the two. This simplification increases the chances of successful binding allowing for better characterization of surface coverage and binding efficiency. Thiol-modified DNA was purchased from Integrated DNA Technologies. A sequence consisting of adenine for binding, called Poly-A was used to bind to nanoparticles. The sequence for Poly-A is: /5ThioMC6D/CCCCCCCCCCCCCCCCCCCCCCCCCCAAAAAAAAAAAAAAAAAAAA.

Here, as is standard for DNA naming, the sequence is ordered from the 5′ end of the DNA to the 3′ end. “A” stands for a single adenine base, and “C” is for cytosine bases. “/5ThioMC6D/” denotes a thiol modifier on the 5′ end of the DNA. This adds a thiol group that can be attached to gold in the gold nanoparticles. Although the adenines in the sequence are used for binding to the complementary strand, the cytosine bases are there as “spacers” keeping neutral unbound DNA on the section of the sequence that is closest to the GNP. This serves to space out the binding area from the nanoparticles and other Poly-A strands, increasing binding efficiency. The sequence of the complementary strand, called Poly-T, was similar, except with fewer “spacer” cytosine bases, and thymine bases rather than adenine bases. The sequence for Poly-T is: /5ThioMC6-D/CCCCCCCCCCTTTTTTTTTTTTTTTTTT. These strands were attached to the gold electrodes. During binding experiments, Poly-A on modified GNPs binds to Poly-T on the electrodes.

4.4.2. Poly-A/Poly-T Experiments with BVT Conductivity sensors

The first Poly-A/Poly-T experiments were done on interdigitated gold conductivity sensors from BVT Technologies (see Figure 2.10). These electrodes have much larger digits and gaps than even the ACEA e-plate electrodes, but could be connected directly to an impedance meter (as opposed to the proprietary RT-CES system). Impedance measurements were taken with the Agilent LCR meter set at 10 kHz.

For these experiments, first the nanoparticle probes were made (as described previously) and the thiol-modified poly-T DNA strands were attached to the gold electrodes (in a same way the poly A is attached to the gold nanoparticles). After the poly-T is given time to attach, the excess solution was removed from the electrodes and some of the prepared nanoparticle probes were added. Control electrodes were also tested, usually either without the attached poly-T strands or without adding nanoparticle probes. Therefore, the control samples should not have any bound nanoparticles. Generally, impedance measurements were taken for each sensor electrode at this point and again after the probes were given time to attach (after about half an hour).

After the excess nanoparticles were removed, a fixed charge was added to the nanoparticles using the attached PEG and a high pH background buffer. For these experiments, PBS buffer with

a pH of 8.0 is used to add this charge, but the conductivity of this buffer is so high that it overwhelms any change due to the nanoparticles. To remove this effect, the electrodes are washed twice with water so that a difference can be seen between the tested electrodes and the controls.

These results (presented back in Figure 2.11) show that there is a measurable change caused by charged nanoparticles bound to gold IDEs. These results are also consistent with simulations for nanoparticles bound to electrodes, with an overall decrease in impedance. There were some issues with this type of test however. The high concentration PBS required for distinguishing the change caused by nanoparticles is so conductive that it reduces the impedance itself (as seen in point 2 on Figure 2.11). This required washing out the electrode with water, but washing once was often not enough to remove this effect (point 3 in Figure 2.11). After two rounds of washing the electrode with water the difference caused by the nanoparticles can be seen. The issue here is inconsistency. Washing too many times removes the effect altogether, and not washing enough leaves the difference indistinguishable. Therefore, while this was a good proof-of-concept for the chemistry, this is not a practical solution for a working biosensor.

As an alternative, experiments were done without the high concentration pH 8.0 PBS. Instead, a low concentration neutral buffer was used for all measurements. These experiments had the exact same DNA binding and nanoparticle attachment steps, except all measurements were done in the low concentration buffer, eliminating the need for excessive washing steps. The buffer used in these cases was a 0.15mM concentration of KCl salt dissolved in water.

Even on the larger “e-plate” electrodes, a measurable change impedance is observed between electrodes with bound nanoparticles compared to controls (as shown in the graph presented in Figure 2.12). However, these results are not as repeatable, and can vary by large amounts (though this could be due to the large dimensions of the electrodes, which would decrease the sensitivity).

This same experiment was therefore repeated once microfabricated gold electrodes were made on glass with much smaller dimensions (20 μm digits with 10 μm gaps, Electrode A from Table 3.3). The same binding procedure with poly-A and poly-T with nanoparticles was used. In addition to impedance measurements, AFM imaging was done on the electrodes.

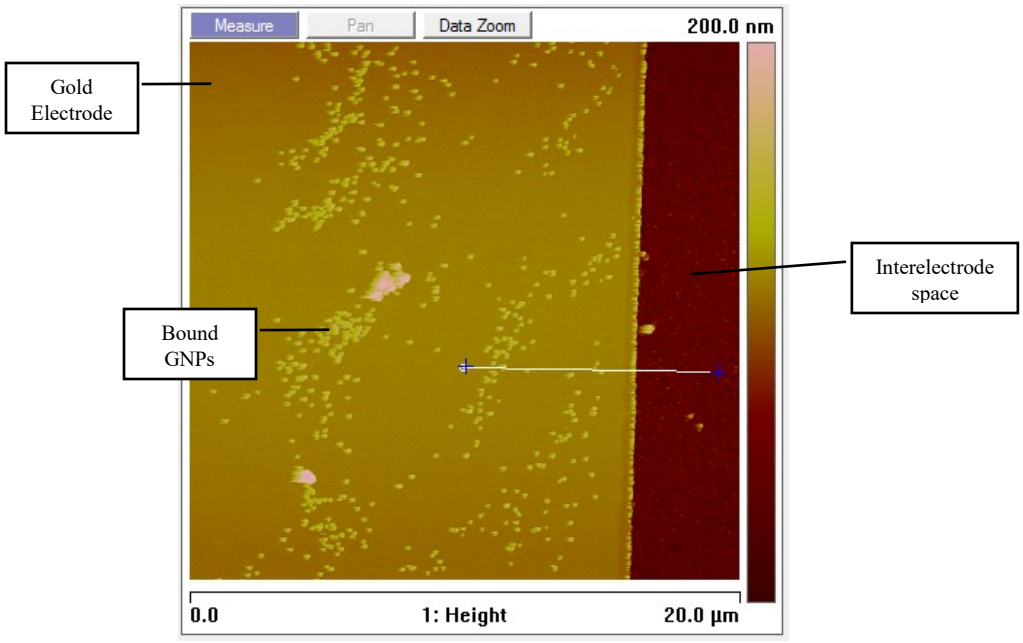

Figure 4.4: AFM image of gold nanoparticles bound to a gold electrode digit via complementary DNA sequences. The large yellow area is the gold digit, the red area is the glass between digits and the lighter yellow dots are bound nanoparticles.

AFM imaging showed nanoparticles bound only to electrode digits and not between. This confirms that the binding method used is specific to binding only to gold. Even with these results, unfortunately the impedance results were not consistent enough. Even after repeated experiments there were no major changes in impedance with nanoparticles compared to without nanoparticles. Tests were done with larger concentrations of nanoparticles and DNA, but even with confirmed binding with AFM imaging, still no meaningful, consistent changes. It was therefore necessary to refine the design. After further research and simulations (see Chapter 3), it was decided that binding nanoparticles between electrode digits rather than on top should be a better design and lead to more sensitive and consistent results.

4.5. Electrode Substrate Binding

In Chapter 3 it was shown that gold nanoparticles bound between electrode digits can have a much greater impact on the impedance of the interdigitated electrodes than if the nanoparticles

are bound to the gold electrode digits themselves. While on the simulations this change is as easy as moving the positioning of the nanoparticles, in practicality this proved much more difficult. To bind MREs to the substrate between electrodes, different methods often involving multiple steps and surface treatments were necessary. Several different methods were explored for different MREs, but many involve similar first steps, treatments, and some basic modifications.

4.5.1. APTES Surface Modification of SiO_2 Substrates

(3-Aminopropyl)triethoxysilane (APTES) was chosen as an intermediary molecule between the silicon dioxide substrate and bound MREs/GNPs. One end of the APTES molecule binds via silane chemistry to the -OH groups on the surface of the silicon dioxide substrate and the other end of the APTES terminates with an amine group (NH_2) which can be used to bind to a variety of functional groups on other linker molecules or directly on antibodies or other MREs.

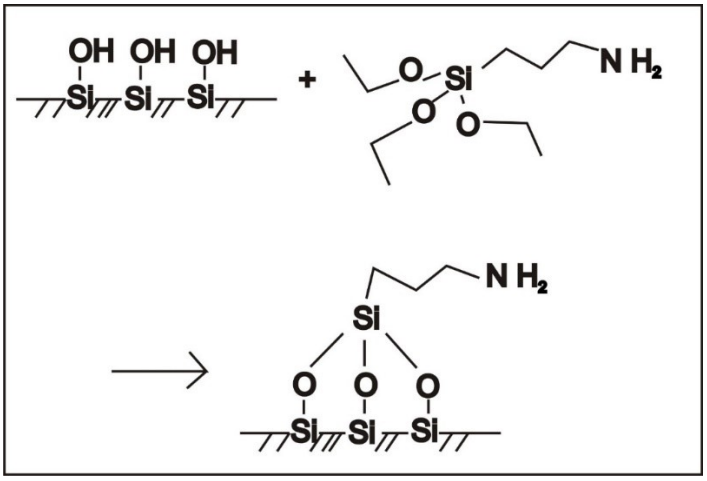

Figure 4.5: Schematic of APTES binding to a prepared silicon dioxide surface. The amino functional group on the APTES is used as an anchor for binding MREs to the spaces between electrode digits.

Initial tests with APTES binding were to directly bind modified GNPs to electrodes (as mentioned in previous chapters). There were several motivations for these tests including: comparting results directly to simulations, simplifying the tests by removing biological molecules and MREs, and characterizing measurement parameters and each modification.

The first step in APTES modification of any of the electrodes is to treat the surface with oxygen plasma. Oxygen plasma is commonly used to "prepare" surfaces for modification [125]. Without oxygen plasma, the surface of the silicon dioxide exists in varied states with terminating -OH groups, or bonding oxygen at the surface (Figure 4.6 a). The addition of energy from oxygen plasma causes reactions with break oxygen bonds and provides uniform coverage of the -OH groups required for APTES modification. This effect does not last long however (several hours or so), so APTES must be added immediately after the oxygen plasma treatment. For both aluminium and gold electrodes (on silicon dioxide substrates), oxygen plasma was applied at 1torr O_2 pressure for 10 minutes at low voltage.

Immediately after oxygen plasma treatment various concentrations of APTES (in ethanol) are added to each electrode and left to incubate refrigerated (to prevent evaporation of the ethanol) for two hours. After this the APTES solution is washed with ethanol several times and dried. The different concentrations tested were 2, 5, 7, 10, and 20% V/V. The motivation for testing various concentrations was to attempt to optimize the APTES surface coverage. More APTES coverage, and equally importantly more uniform coverage over the surface, should result in more binding sites available for GNPs, which should result in a more sensitive sensor. However, too much APTES (as will be seen soon) oversaturates the surface and can lead to aggregation of APTES. Once modified with APTES, electrodes can be stored at room temperature until they are used for further modification or testing. In the case of direct GNP attachment tests, further testing came in the form of directly binding modified GNPs.

4.5.2. Synthesis and Modification of GNPs[7]

Synthesized GNPs used for sensor experiments were made using the Turkevich-Frens method [126] using using trisodium citrate dihydrate (TSC) (purchased from Sigma-Aldrich) as both as reducing and dispersion agent. Hydrogentetrachloroaurate trihydrate ($HAuCl_4.3H_2O$) (99.9 % Aldrich) was used as a gold precursor. The GNPs were characterized by transmission electron microscope imaging. Characterization of these GNPs showed a consistent diameter of 16nm.

[7] Gaser Nagah is a very talented chemist who worked with me in the lab and created the GNPs used in these experiments.

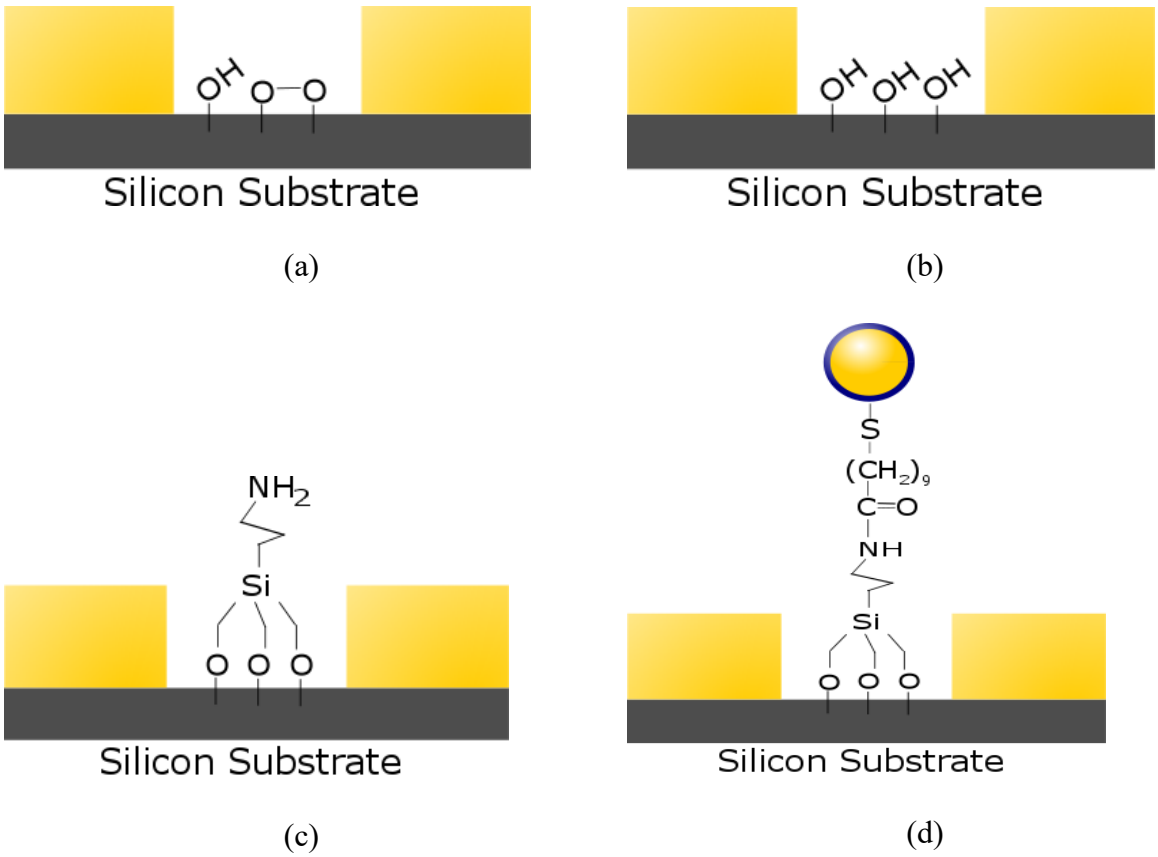

Figure 4.6: (a) Silicon IDE chip after microfabrication. Silicon dioxide substrate has reacted with oxygen in the air, but not always in the same fashion. (b) Oxygen plasma removes the silicon oxide layer and it is replaced with hydroxy groups. (c) Hydroxy groups are used as binding sites for the APTES, which have a free amine group. (d) GNPs are bound to the APTES using EDC/NHS chemistry.

The prepared nanoparticles were next modified with 11-Mercaptoundecanoic acid (MUA) to provide a -COOH functional group that can be used as a binding group to bind to amine groups on MREs or directly to APTES. MUA binds via thiol binding to the gold of the GNPs (described previously). The surface functionalization of the GNPs was carried out as follows. To a 5ml of GNPs dispersion of estimated concentration 0.22 µM GNPs, a 5mL aqueous solution consisting of 2mM Poly(ethylene glycol) methyl ether thiol molecular weight 800 (Aldrich) and 2mM of MUA (Aldrich) was added drop wise. The concentration of MUA was selected to be 20% (V/V). The reaction solution was stirred overnight to ensure sufficient functionalization of the

nanoparticles. Then the MUA-GNPs were collected by centrifugation at 13000rpm for 10 minutes and resuspended in Milli-Q water. The last two steps were repeated two more times to completely remove the unbound thiol compounds. GNP functionalization was evaluated by zeta potential measurement (Zetasizer Malvern) and nuclear magnetic resonance (NMR).

4.5.3. GNP/APTES Direct Detection Tests[8]

For tests without MREs and biological molecules, MUA-GNPs were bound directly to APTES bound to the silicon dioxide substrate between IDE electrode digits using EDC/NHS chemistry [127]. The general procedure for these tests is shown in Figure 4.7. After oxygen plasma treatment and APTES modification, the impedance of the electrodes was taken over a range of frequencies. This not only confirmed and characterized the APTES modification, but also served as a baseline for comparisons after GNPs are added. For MUA-GNP APTES binding the carboxylic group at the nanoparticle's surface was activated by the addition of 30mM N-Hydroxysuccinimide (NHS) (Aldrich) and 15 mM N-(3-Dimentylaminopropyl)-N′-ethylcarbodiimide (EDC) (Sigma-Aldrich) 15 mM. A polydimethylsiloxane (PDMS) template cover with 8 well was fixed over the chip, where each well set directly over each IDEs. Later after that, 50 µL of the activated MUA-GNPs were added in each well and the IDEs were incubated overnight to complete the binding. The GNPs solution was discard from each well and all IDEs were washed several times with Milli-Q water removing unbound GNPs. The concentration of GNPs was kept high enough to be in excess of the APTES, assuring that the APTES concentration will be the limiting factor for binding sites on the electrode. Once nanoparticles were added, left to bind, and washed, a second impedance measurement was taken for each electrode. The result of this measurement was then compared to the previous result. Further surface imaging was done using AFM imaging to check for bound nanoparticles and APTES characterization.

[8] Again, my appreciation goes to the lab chemists Gaser Nagah and Donghai Lin for their work on surface modification of the electrodes. Also to Marcus Tamura (summer student) and Zhimin Yan (NINT researcher) for all of their help with these experiments.

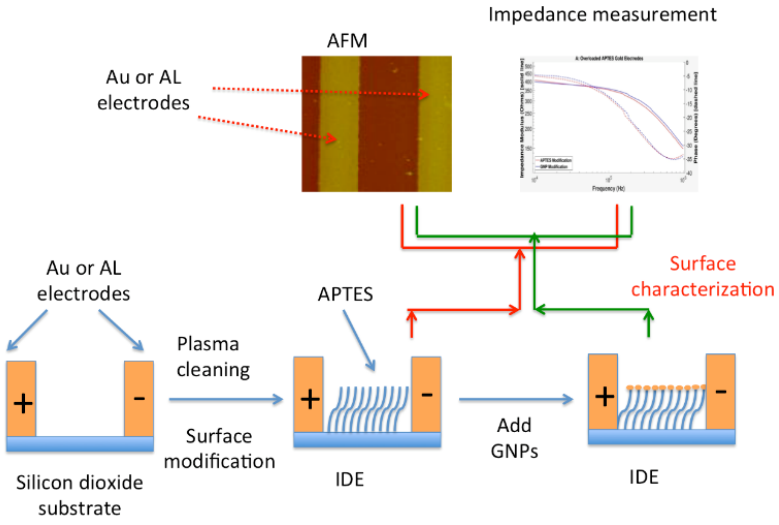

Figure 4.7: Overview of APTES tests. Electrodes are prepared and modified with APTES, then GNPs are chemically attached. Impedance measurements and AFM imaging was done before and after the addition of GNPs.

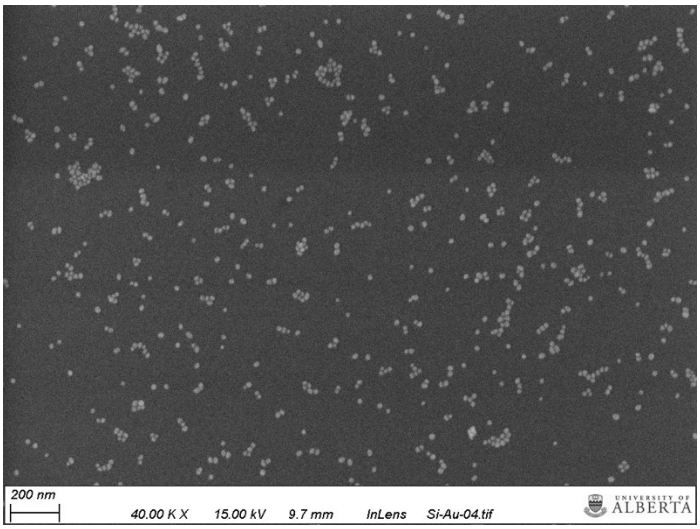

Figure 4.8: Scanning electron microscope image of 13nm gold nanoparticles bound to a silicon dioxide substrate.[9]

[9] A big "thank you" to Nikola Pekas, a NINT researcher who I worked with on the binding chemistry scheme and who took this AFM image using a NINT AFM.

4.5.4. GNP/APTES on Aluminum Electrodes

Figure 4.9 shows a representative set of measurements for one electrode before and after nanoparticles are added (with a 5% APTES concentration) on an aluminum IDE chip (Electrode D from Table 3.3). The aluminum electrodes used for these tests were designed with 4 µm digit width with 2 µm spacing between adjacent digits. As seen from these results, the addition of bound nanoparticles increases the impedance magnitude and decreases the phase. These results are consistent with previous simulations (see Chapter 3). Figure 4.10. shows accumulated results of multiple GNP/APTES tests on aluminum electrodes with varying concentrations of APTES (ranging from 2%-10%). These results are presented as the percent difference in the impedance magnitude before and after GNPs are bound. Error bars in the graph are from repeating the APTES concentration on three separate electrodes. As seen here, although the difference in impedance increases as the APTES concentration increases from 2% to 5%, higher concentrations of APTES have a smaller change and have much larger standard deviations. This indicates that if the APTES concentration is too high it can limit the available binding sites for GNPs (more on this in the following sections).

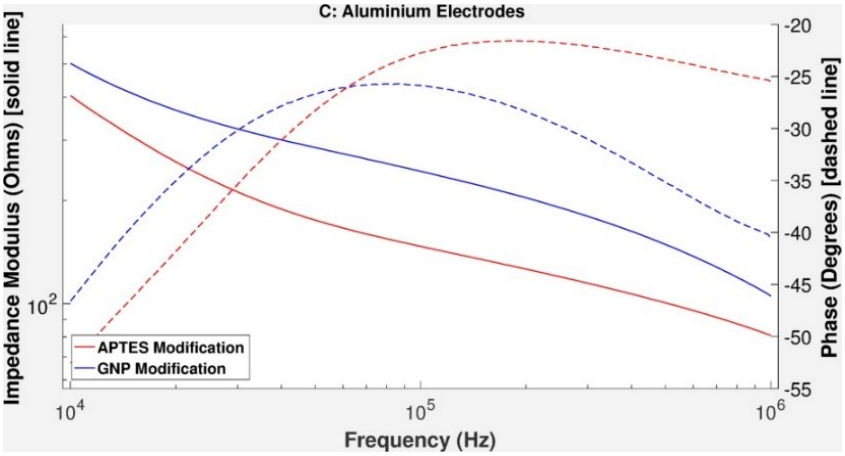

Figure 4.9: Representative impedance spectrum results for an aluminum IDE (Electrode D from Table 3.3) before and after GNPs are attached. Red lines are after APTES modification (before GNPs). Blue lines are after GNPs were added. Solid lines are impedance magnitude measurements, and dotted lines are impedance phase.

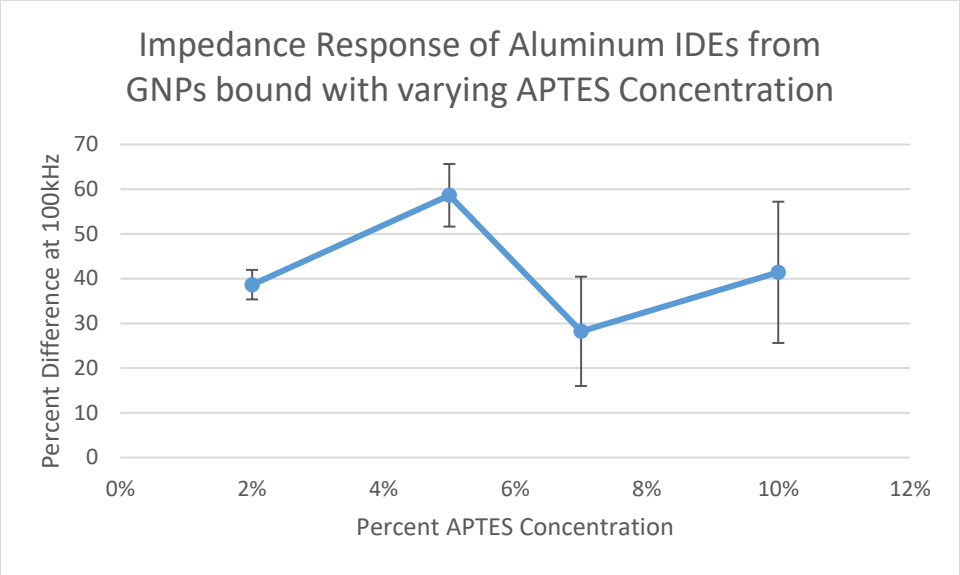

Figure 4.10: Accumulated results of APTES-GNP tests on aluminum electrodes (Electrode D from Table 3.3). Each bar represents a different concentration of APTES and the percent difference value is calculated as the percent difference in impedance magnitude between impedance magnitude measurements before and after GNPs are bound (measurements taken at 100 kHz).

As seen in Figure 4.10, there is no statistical difference between the 2%, 7%, 10%. This could be due to a few factors. First, the APTES concentration may not be the limiting factor in detection. If the concentration of GNPs is not sufficient, it would limit how many can be detected, regardless of binding sites available. The second, more likely factor is variance between electrodes. The electrodes used in these experiments had some variation in their impedance response due to variations in fabrication. This had more of an effect on the gold electrodes than the aluminum ones as seen in the next section.

As mentioned in the previous chapters, the purpose of aluminum electrodes was mainly to simplify fabrication, and take advantage of the capacitive and insulating effects of natural aluminum oxide layers. Compared to results on gold (see the next section) there is less variance between tests on aluminum electrodes, but aluminum electrodes will react with ionic solutions, destroying them in a matter of hours, making their application in testing biological samples limited.

4.5.5. GNP/APTES on Gold Electrodes

The same GNP/APTES tests were done on gold electrodes as well (with 4 µm wide digits and 2 µm spacing between adjacent digits, Electrode E from Table 3.3). Figure 4.11 shows a typical result before and after the addition of GNPs. While the values are different than the results for aluminum electrodes, the overall trends are the same, with GNPs causing an increase in impedance magnitude and a decrease in phase.

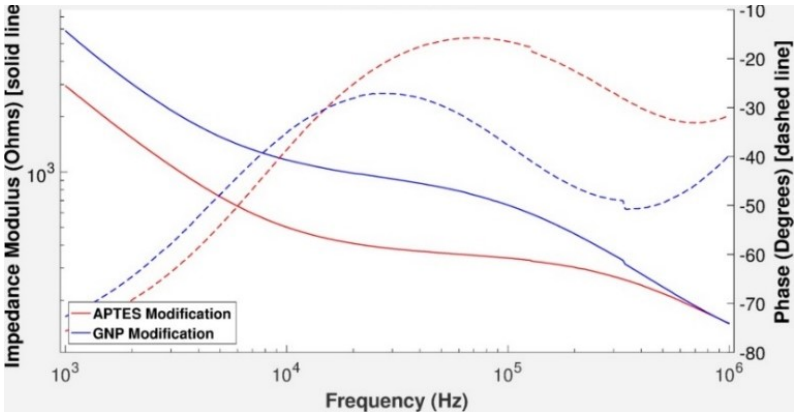

Figure 4.11: Representative impedance spectrum results for a gold IDE (Electrode E from Table 3.3) before and after GNPs are attached. Red lines are after APTES modification (before GNPs). Blue lines are after GNPs were added. Solid lines are impedance magnitude measurements, and dotted lines are impedance phase.

The accumulated results are shown in Figure 4.12. and like the results with aluminum electrodes, there is a measurable change in impedance of electrodes caused by the addition of GNPs. It should also be noted that the standard deviation in these results is larger than the results from aluminum electrodes. This is likely because of the challenges in gold etching during fabrication (wet etching gold can lead to overetching and inconsistent dimensions), or the lack of an insulating layer around the electrodes.

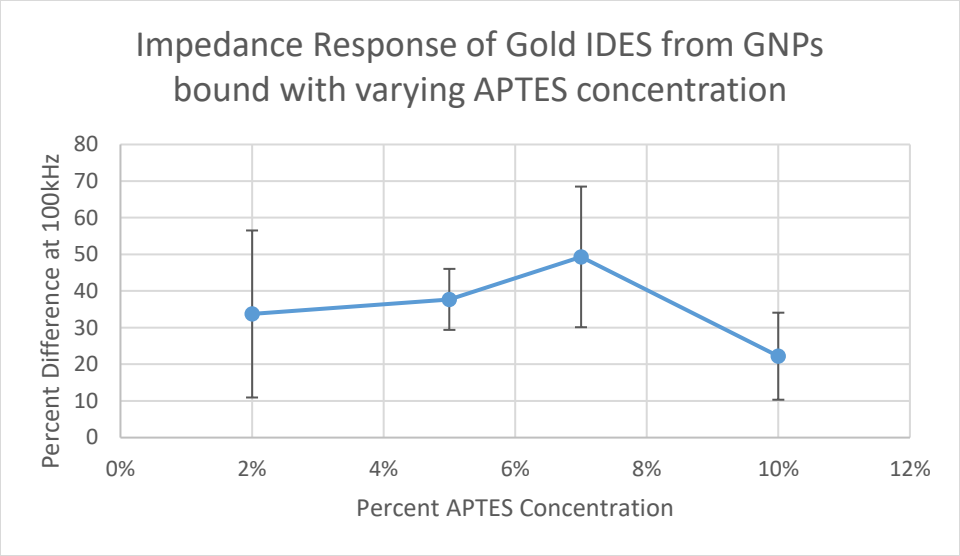

Figure 4.12: Accumulated results of APTES-GNP tests on gold electrodes (Electrode E from Table 3.3). Each bar represents a different concentration of APTES and the percent difference value is calculated as the percent difference in impedance magnitude between impedance magnitude measurements before and after GNPs are bound (measurements taken at 100 kHz).

These potential explanations are both supported by AFM images taken of electrodes after the addition of GNPs. Figure 4.13 shows one such image taken of a gold electrode after GNPs were added. Large aggregations of GNPs are present on and around electrode digits [128]. Additionally, the dimensions of the electrodes are clearly different than what was designed, due to overetching in the fabrication of the electrodes.

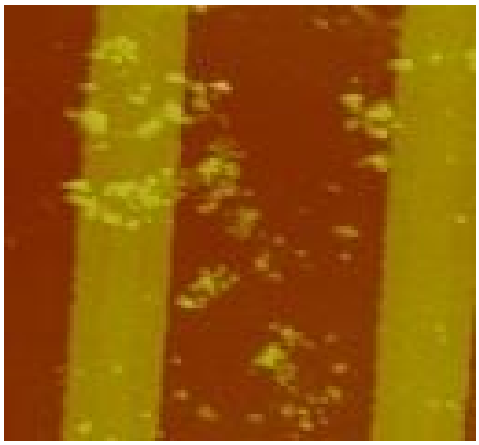

Figure 4.13: GNPs clumping on and around gold electrodes (Electrode E in Table 3.3). Images were taken using an AFM. The image is 5 µm x 5 µm. This image also shows the effect of overetching on the electrode as each electrode digit is less than 4 µm and the space between them is larger than it should be.

4.5.6. MUA Electrode Surface Modification Tests

From the results of tests with aluminum and gold electrodes, it is apparent that while aluminum electrodes gave more stable results (likely due to the native oxide layer around the electrodes), gold is the only option for most applications due to its stability in ionic solutions. Therefore, it was decided to try to duplicate the effect of an oxide layer on gold electrodes. By adding an insulating layer to the gold IDEs, extra capacitance, stability, chemical isolation could be gained [129]–[131]. To do this, MUA was used to coat the gold, in a similar way as it has been previously reported for modifying gold surfaces [132], [133]. This is the same molecule used to modify the GNPs. Before APTES modification gold electrodes were immersed in high concentration MUA. Like with the GNPs the thiol group on the MUA has a high affinity for the gold on the electrode and forms a self-assembled monolayer on the gold surfaces of the electrode. After MUA modification, the same APTES/GNP test was performed, with the hope that the MUA would provide extra stability to the measurements, and prevent GNP aggregation on the electrodes.

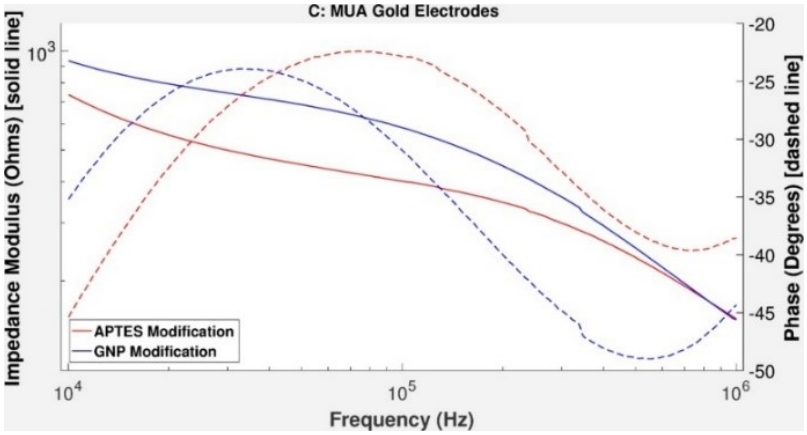

Figure 4.14: Representative impedance spectrum results for a gold IDE (Electrode E from Table 3.3) modified with MUA before and after GNPs are attached. Red lines are after APTES modification (before GNPs). Blue lines are after GNPs were added. Solid lines are impedance magnitude measurements, and dotted lines are impedance phase.

Figure 4.14 shows representative results of APTES/GNP tests on MUA-modified gold electrodes. In general, results are as expected, with a slight increase in the percent difference in impedance magnitude and a slight decrease in phase. This indicates that the added MUA had the intended effect of isolating the gold and stabilizing the measurements. (Note: experiments using MUA-modified electrodes are ongoing)

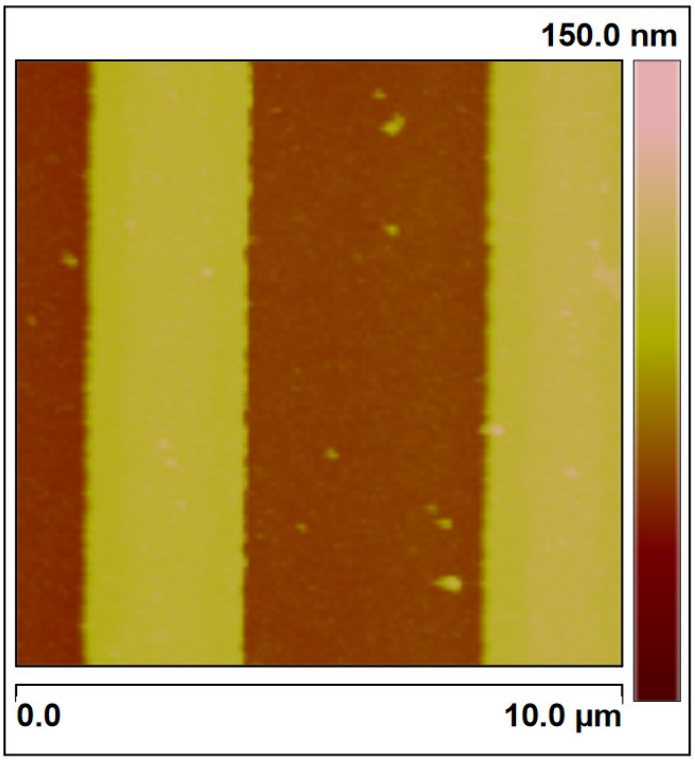

Figure 4.15: Representative AFM image of a gold electrode (Electrode E from Table 3.3) modified with MUA, APTES and GNPs. Nanoparticles are present between the electrode digits and dispersed without aggregation. The image is 10 µm x 10 µm.

4.5.7. APTES Binding Issues

The results of the previous tests using APTES showed a sharp decrease in effectiveness as the concentration is APTES increased leading to the hypothesis that too much APTES inhibited the formation of uniform surface binding and limited GNP binding sites. Additionally, a large amount completely and irreversibly shorted out electrodes. Figure 4.16 shows one such result, where a high concentration of APTES was used. Right after the addition of APTES the electrode showed signs of acting more like a resistor than a capacitive system (near zero phase and impedance magnitude mostly independent of frequency). The results were exactly the same after the addition of GNPs, meaning either they did not bind to the electrode or their effect was overshadowed completely by the APTES.

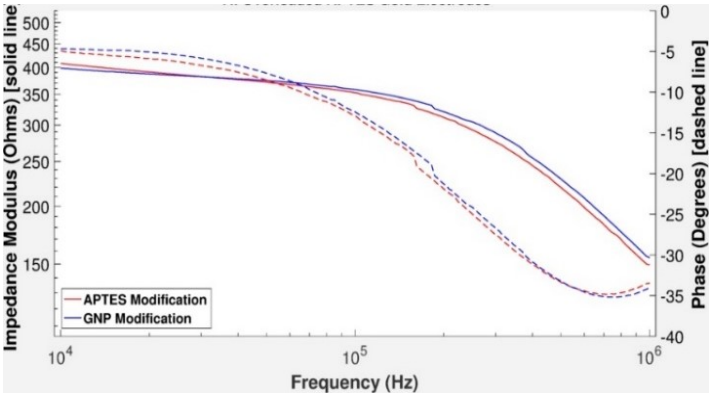

Figure 4.16: Representative impedance spectrum results for a gold IDE (Electrode E from Table 3.3) before and after GNPs are attached with a high concentration (20%) of APTES used. Red lines are after APTES modification (before GNPs). Blue lines are after GNPs were added. Solid lines are impedance magnitude measurements, and dotted lines are impedance phase.

Upon inspection using AFM, the reason for this became clearer. When higher concentrations of APTES were used (10% and 20%), large amorphous clumps can be seen covering the electrodes. These cover all areas of the electrodes, bridging the gaps between the electrode digits. This is the cause of the results seen in Figure 4.17.

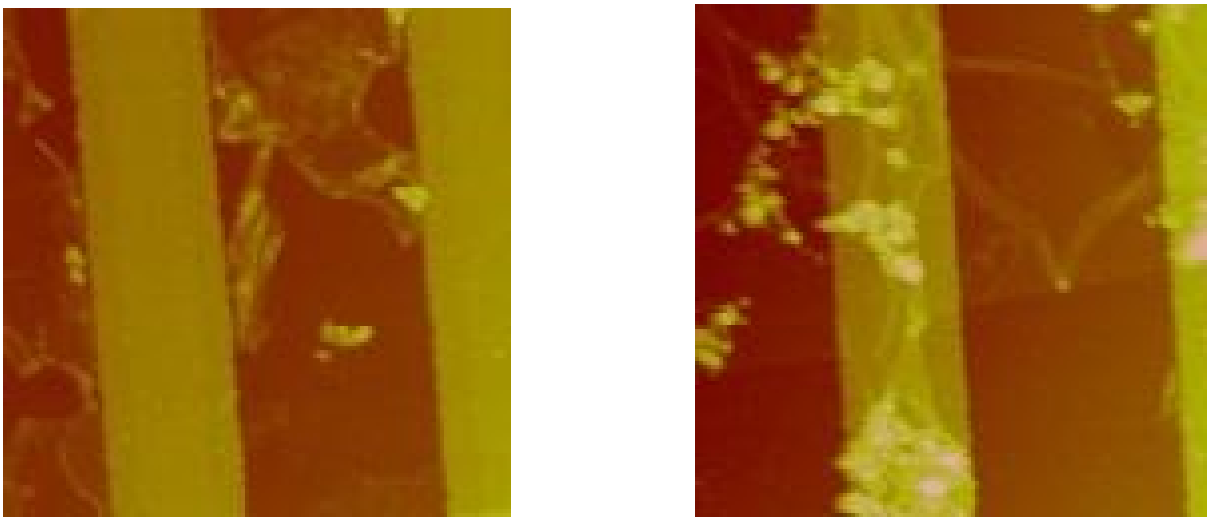

Figure 4.17: AFM images of interdigitated electrodes modified with “10%” (left) and “20%” (right) APTES as well as 13 nm GNPs. Each image is 5 µm x 5 µm. These images show aggregated APTES on and between electrode digits and aggregated GNPs. This non-uniformity is the likely cause of the widely varying impedance measurements for electrodes with higher concentrations of APTES.

4.6. Antibody/protein Tests

All tests up to this point have been proof of concept tests in various forms. Tests have been done to detect bound nanoparticles, but without biological recognition in between. Therefore, the next step in testing would be to use what was learned up to this point to detect a biomolecule with clinical relevance using the sensor system. While the design of the sensor is such that many different substances could potentially be detected, we wanted to find something that would be: 1) easy to detect in quantities that are biologically relevant (levels that would be found in real biological samples), 2) well characterized and understood, 3) something with a standard test already used that could be used for comparison, 4) well defined molecular recognition elements readily available, and 5) sensing this biomolecule would have a practical use and need in health care applications. A biomolecule that fits with these criteria was found through a collaboration with Dr. Rachel Khadaroo at the UofA hospital. Her research has found that Intestinal Fatty-acid Binding Protein (I-FABP) is a strong diagnostic marker of acute mesenteric ischemia (an indicator for bowel damage) [134]. There is currently a standard ELISA that uses readily available anti-I-FABP antibodies for testing. The clinical relevance for using this biosensor system rather than the ELISA is time. While the ELISA is adequate in detecting relevant amounts of I-FABP, the test takes over 4 hours to complete [135], and takes a trained professional to carry them out. This is too long to be clinically relevant, as a positive test for bowel death would require immediate surgery. The designed biosensor, depending on the configuration of the test, would take much less time (~2 hours or less), and be much less labor intensive. Therefore, detecting I-FABP became the first model biomolecule for testing this system.

Tests for protein detection are ongoing, and the particulars of the experimental procedure are constantly evolving. Example results from recent tests are shown in Figure 4.18 which shows results from one electrode with bound capture antibodies, 2ng/mL I-FABP, and GNPs modified with a secondary antibody for I-FABP. The results shown here are before and after nanoparticles were added. The results here are very similar to the results of the APTES/GNP experiments, with an overall increase in impedance magnitude, and a decrease and shift in phase. This indicates that both nanoparticles are bound to the electrode, and that the protein (at 2ng/mL) has successfully been detected.

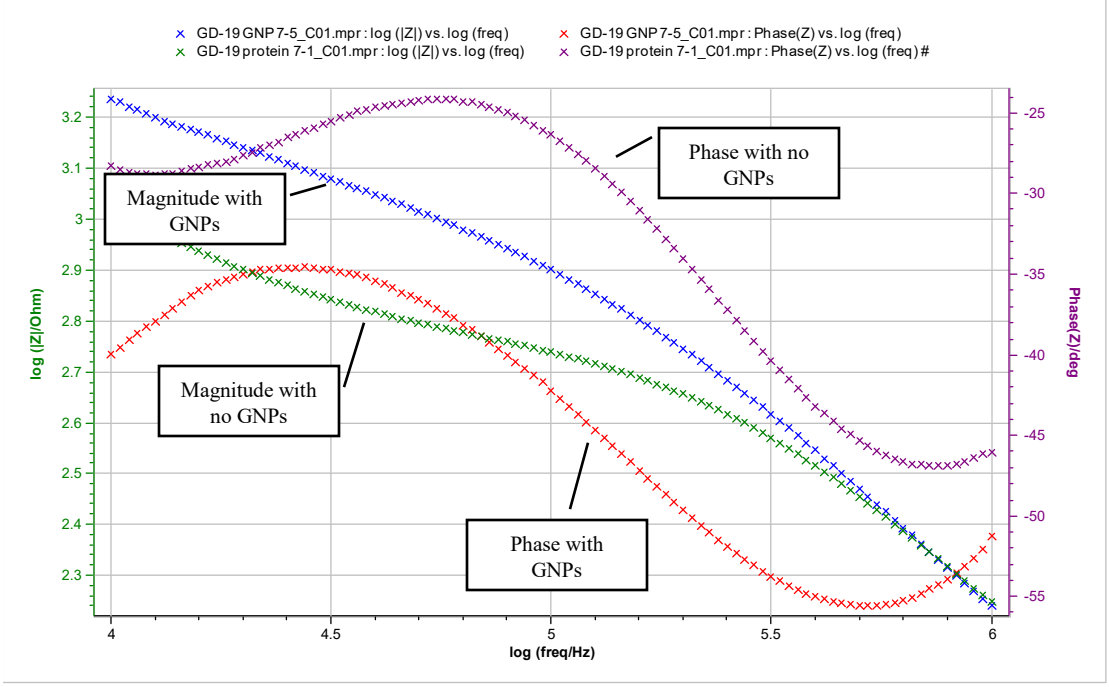

Figure 4.18: Impedance measurement results on an electrode (Electrode E from Table 3.3) before and after the addition of IgG modified gold nanoparticles. The green (impedance magnitude) and purple (impedance phase) lines correspond to the results before the addition of nanoparticles. The blue (impedance magnitude) and red (impedance phase) lines correspond to results after the addition of nanoparticles.

In order to eliminate the possibility of non-specific binding (i.e. nanoparticles stuck to the surface electrode and not binding to the proteins on the electrode), negative control electrodes were also tested. In these cases, all steps were kept the same for nanoparticle and electrode modification, but no I-FABP was added. Nanoparticles modified with antibodies were still added to the electrodes, the same washing was done afterwards to remove unbound GNPs from the surface. Impedance measurements were taken before and after the addition of GNPs (and washing). Figure 4.19 shows the results of the negative control test. Here, while there is a slight change in impedance magnitude and phase, which may be accounted for from some non-specific binding, or measurement error. Overall this change is not nearly as significant as with the positive test (an approximate 100% change in impedance magnitude compared to only about 20% for the negative control.

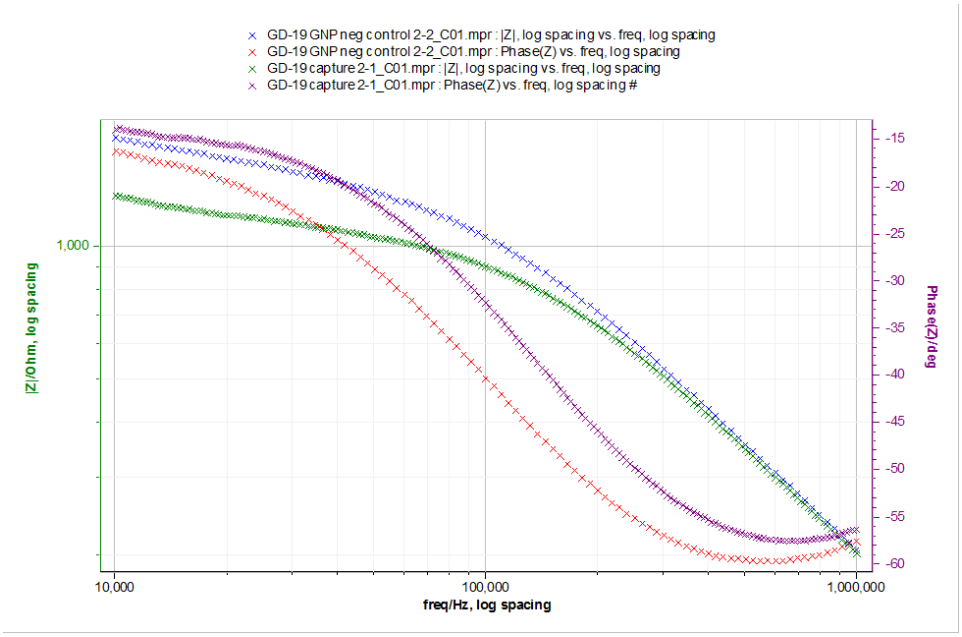

Figure 4.19: Impedance measurement results on an electrode (Electrode E from Table 3.3) before and after the addition of IgG modified gold nanoparticles without the addition of I-FABP, acting as a negative control. The green (impedance magnitude) and purple (impedance phase) lines correspond to the results before the addition of nanoparticles. The blue (impedance magnitude) and red (impedance phase) lines correspond to results after the addition of nanoparticles.

Testing for I-FABP has continued to the stage of measuring different concentrations of I-FABP suspended in synthetic human urine. The urine was spiked with 1, 2, 3, 4, 5, and 7 ng/mL of I-FABP. The urine was tested using the same procedure shown above, where electrodes were modified with antibodies, the urine was deposited on the substrates and washed with modified GNPs. Impedance measurements were taken on the modified electrodes and after the addition of GNPs. Figure 4.20 shows very early results from a test of varying I-FABP concentration (note: because these results are so new at the time of writing this, there is not enough data for a full statistical analysis). These results were obtained by taking the difference in the impedance magnitude value measured at a single frequency (100 kHz). They show a linear trend in the change in impedance magnitude as the concentration of I-FABP increases. Overall, these results are meant to demonstrate the utility of using this system as a practical biosensor. Here, proteins in synthesized human urine were detected at concentrations that are relevant to the diagnosis of actual serious health conditions.

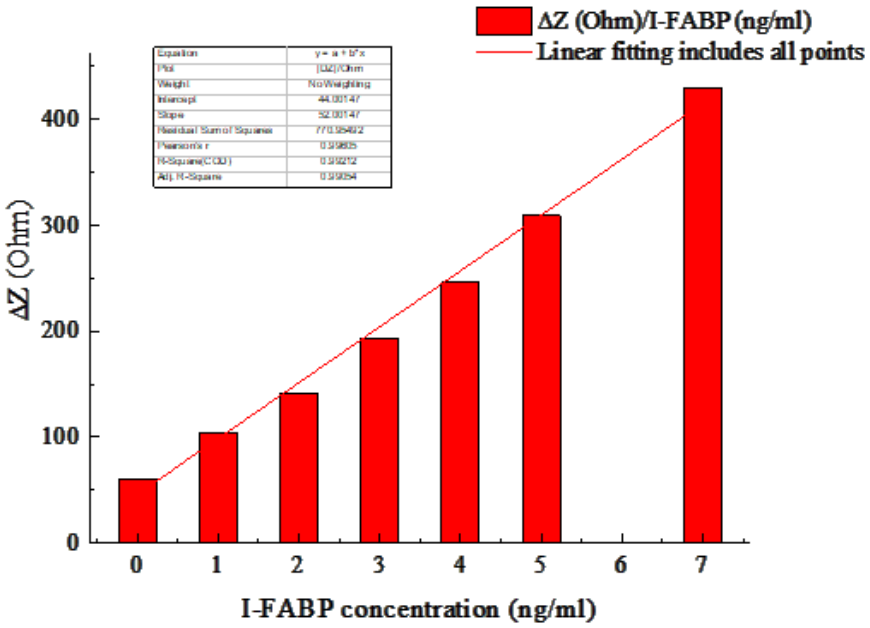

Figure 4.20: Preliminary results of varying I-FABP concentrations. Results are expressed as the difference in impedance magnitude measured at 100 kHz from an initial measurement on a modified electrode and then one after the electrode was exposed to synthetic human urine spiked with I-FABP and MRE modified GNPs. A best fit line shows there is a linear trend in increasing protein concentration and impedance change.

In addition to impedance testing, electrodes modified and tested for I-FABP were imaged and characterized using AFM imaging. Figure 4.21 shows three AFM surface plots of the silicon dioxide space between electrode digits at different stages of surface modification and testing. Figure 4.21 a. shows a bare, unmodified electrode, and as expected, the surface is very smooth with less than 2nm of variation over the surface. Figure 4.21 b. shows a similar section after the electrodes were modified with antibodies. This section shows more overall roughness, and some comparatively large “clumps”. Figure 4.21 c. shows another section after I-FABP and GNPs were added. There is even more variation and overall roughness in the image indicating that there are additional bound entities on the surface. These images show the progression of the modification steps and along with the impedance measurements show the surface chemistry and detection mechanism of this sensor system.

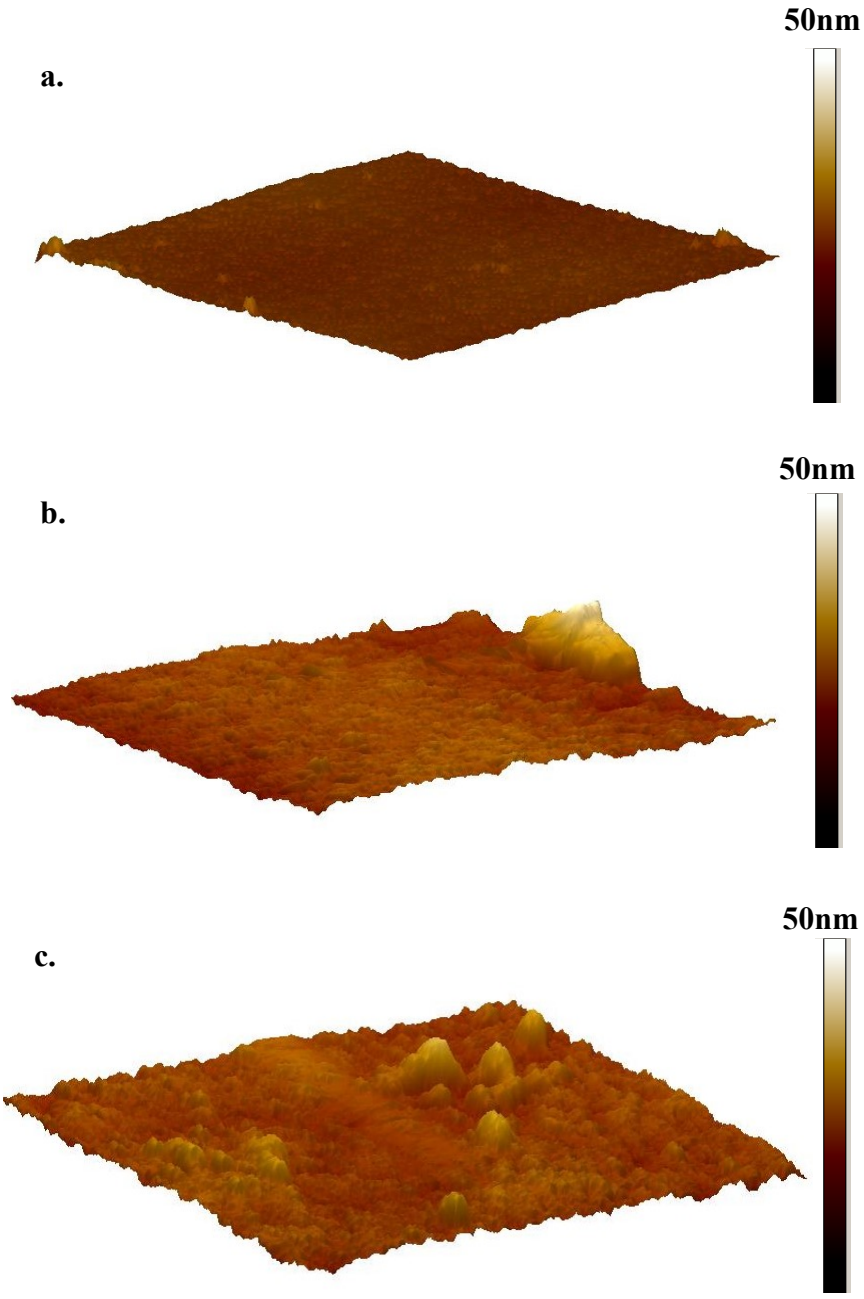

Figure 4.21: AFM surface plots of a section of the silicon dioxide substrate between gold electrode digits (Electrode E from Table 3.3) during modification for detecting I-FABP. Each section is a 2 µm x 2 µm area with a vertical scale of 50 nm (shown by the colour scale bar). a) an unmodified, bare electrode. b) modified with antibodies. c) after the addition of I-FABP and GNPs.

4.7. Conclusion

This chapter covered the techniques used to bind molecular recognition elements and GNPs to IDEs, as well as characterization and detection of the modifications. The synthesis and surface modification of nanoparticles was discussed, along with techniques used in early experiments in modifying electrode digits. More complex binding schemes had to be devised for binding nanoparticles between electrode digits, but measurement results showed that (as the earlier simulations indicated), this lead to more sensitive detection. Finally, a full design was tested for detecting a clinically relevant biomolecule. At the time of writing this, tests are continuing focusing on refining surface modifications, and detecting other biomolecules.

The original goal of this research, to keep things in perspective, is to make a versatile, handheld, inexpensive biosensor device. The design and experiments discussed so far cover the detection mechanism, versatility, and effectiveness of this system. What hasn't been discussed (yet) is the sensor itself. Impedance measurements have generally been taken on large tabletop electrochemical analysis equipment, and while these tools have been invaluable, they are not exactly inexpensive or portable. The next chapter focuses on the hardware design of the sensor and the creation of a specialized impedance measuring circuit and software to act as the biosensor itself.

Chapter 5 : Hardware

5.1. Introduction

The first four chapters of this thesis have focused on the mechanism proposed for this sensor, and with good reason. It was a laborious process to design a system for measuring small amounts of analytes, and make each of the disparate components involved work together to prove the proposed concept. And while many components had to be designed and made from scratch, existing equipment was, up until this point in the research, used for taking impedance measurements. Many devices exist that were appropriate for the tasks required, such as the RT-CES cell counting system, LCR meters, or electrochemical work stations. However, the main goal of this research was to create a portable, easy to use, and inexpensive biosensor, and none of the devices used previously for measurements fit these qualifications. The natural conclusion is that an entirely new device had to be designed and created. There have been other, similar designs proposed for impedance measurements in biological applications as well [136], though these are often specifically designed for certain applications.

Beyond the basic metrics of properly measuring impedance, reliability, cost, and size, there are many other considerations to take into account. The concept is for the biosensor to be used by either medical personal with limited training, or eventually anyone. It should therefore be easy to use, and the results should be clear and not require excessive interpretation. This means that the device itself should take measurements, calculate results, and display/save results on its own. The impedance measurements made by the device must be sensitive and precise enough to distinguish between relevant numbers of nanoparticles bound to electrodes. The device has to operate within an applied frequency range for optimal measurements. The voltage applied to electrodes during measurement has to be kept low enough to ensure no electrochemical reactions take place [42], [65].

In the most basic sense, impedance is the AC form of resistance. Where a resistor causes a voltage drop across it, an impedance causes an AC voltage drop as well as a phase shift. To measure total impedance either the real and imaginary components of the impedance have to be measured, or the impedance magnitude and phase. Impedance meters apply a known AC current

or voltage to a load, then measures the corresponding AC voltage or current, respectively, from this measurement, the complex impedance of the load can be found.

5.2. Biosensor Device Design[10]

Due to the initial design constraints on the device, certain decisions were made for the initial biosensor design. Most significantly, for size, ease of use, and cost considerations, the decision was made for the computation and display of the device to be offloaded to a smartphone platform. Using a custom app and Bluetooth connection, the sensor device could send raw data directly to the app, where it could be interpreted and presented, saved, or sent. This decision also helps reduce design complexity, using existing hardware in the final device. Other early considerations were the desired frequency range, between 10 kHz and 1MHz, with a focus on measurement accuracy at 100 kHz. It was also known that the input voltage on the electrodes has to be kept below 300 mV to stop electrochemical reactions from happening on the electrodes. In electrochemical sensing, where electrochemical reactions are caused by applied voltages for detection, generally 1-2 V is applied, with reactions occurring between 0.4 V-0.9 V [42], the voltage applied here is set well below that at 100 mV to prevent the possibility of any such reactions influencing the system or impedance results. The biosensor device itself is separated into five parts: the voltage source, impedance magnitude detection, impedance phase detection, and processing. Figure 5.1 shows a basic block diagram for the complete system.

[10] A big thanks to the lab's "hardware team" for their hard work on perfecting the electronics for the sensor. This includes Ryan Corpuz, Ben Flanders, Ian Prescott, Mihai Esanu, Xiaojian Yu, Allison Chen, and Samuel Lehmann. Each of them was invaluable in adjusting, testing, and assembling hardware, as well as designing the software that runs the device. While the initial design specifications as well as the impedance detection strategy were mine, the rest of the team's support was necessary to take it to the level that it is now.

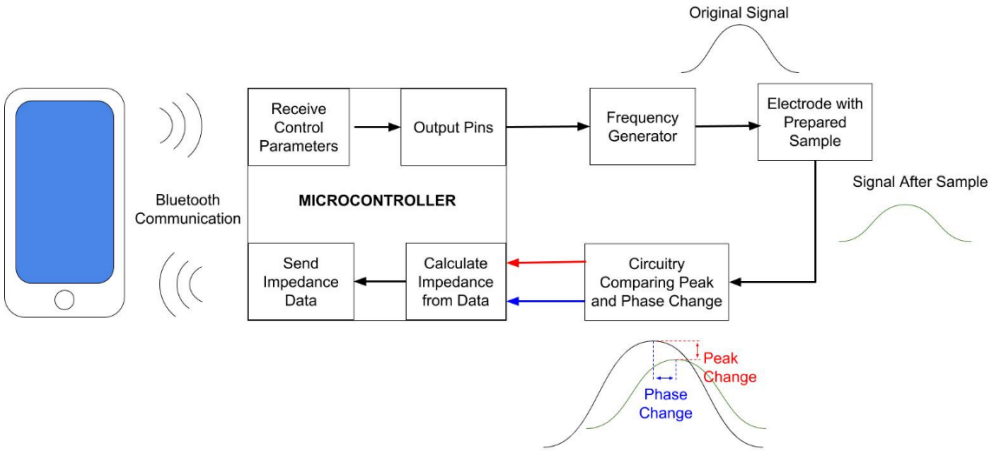

Figure 5.1: Basic block diagram for the entire device.[11]

The voltage source generates an AC voltage at a known amplitude and frequency (with a tunable frequency range) and passes it through a voltage divider between a known resistance and the electrode that is to be tested. The impedance magnitude detection portion measures the drop in voltage amplitude caused by the electrode. The phase detection portion measures the phase delay in the voltage signal caused by passing through the electrode. The information gathered from both components are used together to calculate the total impedance of the electrode. Finally, the data is used to find the impedance data for the electrode and display it on the control app.

[11] Thanks to Ryan Corpuz for putting together this block diagram.

5.2.1. Voltage Source and Voltage Divider

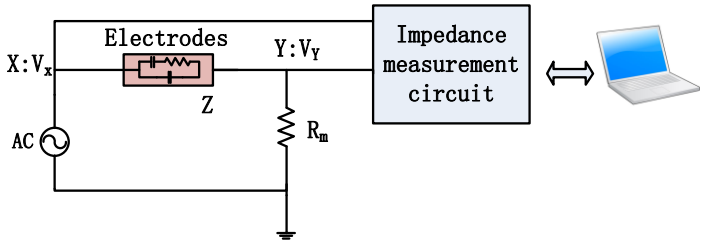

Figure 5.2: Layout of the voltage source and voltage divider. In this figure, the electrode is represented by an equivalent circuit.

A sine generator chip with a frequency range between 100 Hz and 1 MHz (the AD9837 Programmable Waveform Generator by Analog Devices) was chosen as the AC source for circuit. The voltage amplitude of the source is 600 mV. The output of the AC source is passed to both the impedance measurement circuit as a reference signal, and to the electrode. Before passing through the circuit, the voltage is stepped down to 100 mV and is stepped back up to 2 V after. This low input voltage prevents electrochemical reactions on the electrode. The voltage divider, as shown in Figure 5.2, consists of the electrode (represented by an equivalent circuit) in series with a known resistor (2 kΩ).

5.2.2. Impedance Magnitude Detection

The impedance magnitude measurement portion of the design operates by comparing the voltage amplitude change before and after the input voltage passes across the voltage divider. To do this, first the step is measuring the voltage amplitude of the signals. This is accomplished by using an open loop peak detector. This circuit, shown in Figure 5.3, is based on previously reported design [137] which consists of an op amp-based half wave rectifier and a capacitor filter. The rectifier isolates the positive component of the AC voltage and the parallel RC components smooth out the waveform, resulting in a DC voltage output equal to the initial amplitude of the input AC voltage. The RC time constant of the capacitor filter determine the time delay in the signal and the variation in the value. These values were chosen to provide minimal error, while still providing enough responsiveness for reliable measurements (found through testing to be: R_0=1.19 MΩ and

C=2.2 μF). Some changes were made to the initial circuit design including low voltage “stabistor” diodes, and an output buffer to help isolate the circuit and mitigate the effects caused by the low input impedance of the ADC at the output of the detector.

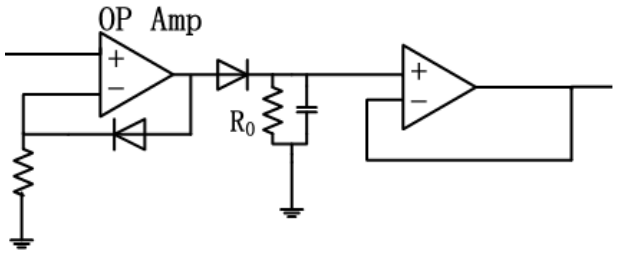

Figure 5.3: Circuit diagram for the open loop peak detector used for impedance magnitude detection.

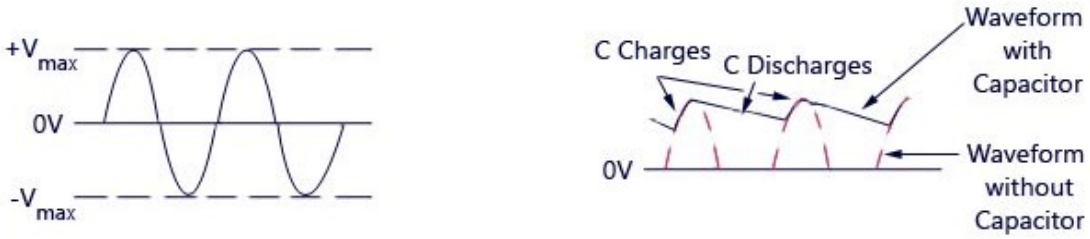

Figure 5.4: Left: Input AC voltage into the peak detector. Right: Resulting output (black line) and the output of the half wave rectifier (red dotted line). By changing the RC parameter of the circuit, the variation between the “capacitor charging” and “capacitor discharging” voltages can be reduced, resulting in a DC voltage at $+V_{max}$. [138]

The input into the peak detector switches between the direct output of the AC source, and the signal after it has been passed through the voltage divider (the electrode) and stepped up. The output result is therefore DC voltages corresponding to the amplitude of the input voltage and the output voltage. The reason for using a switch and a single peak detector is to both save on board space and components, but more importantly to reduce errors in measurements that could be caused by the signals passing through different components. By using a single peak detector, any errors will not be compounded between the two signals.

This system does not measure the exact impedance magnitude of the electrode itself, but rather the total impedance magnitude of the combined voltage divider circuit (the electrode in

series with the known resistance, here called R_m). The information from the phase detection circuit is used to isolate the exact impedance value of the electrode itself.

5.2.3. Impedance Phase Detection

The phase detection portion of the impedance measurement circuit consists of two high speed comparators and an XOR gate (Figure 5.5). The comparators are configured as zero cross detectors (output a "1" when the signal is above the zero point, and "0" if the signal is below). The inputs of the comparators are the AC source signal, and the signal after the electrode, which results in a phase shift based on the phase of the electrode impedance. The output of both comparators are the inputs for the XOR gate.

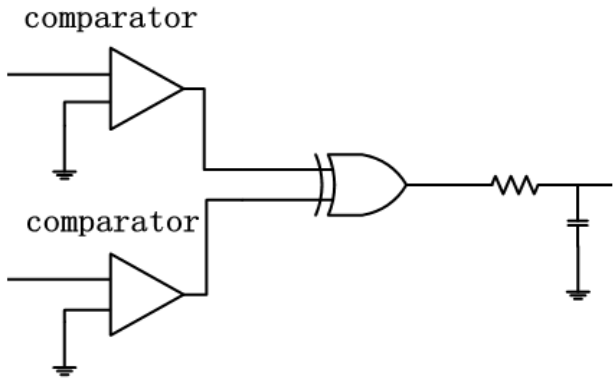

Figure 5.5: Circuit diagram for the phase detection portion of the circuit.

This way, the output of the XOR gate is "1" if one of the voltages is positive while the other is negative, and "0" otherwise. Therefore, the duty cycle of the XOR gate is directly proportional to the phase shift between the two signals. Figure 5.6 shows a general example, where the delay in phase between the two signals is reflected by the amount of time the output of the XOR gate is "1". For an example, if there was no phase change (purely resistive load), there would be no time that one of the signals is positive while the other is negative, so the output of the XOR gate would always be "0" (0% duty cycle). Conversely, a 180 degree phase shift would mean that one signal would always be positive while the other is negative, meaning the XOR gate would always be "1" (100% duty cycle). The RC lowpass filter on the output of the XOR gate filters the output to a DC signal that can be read by the ADC. Since there is no distinction between the two

signals in the design, there is not a clear way to measure the sign of the phase shift, however, since all loads on the system are capacitive in nature (due to the structure of the electrodes), all phase changes are assumed to be negative.

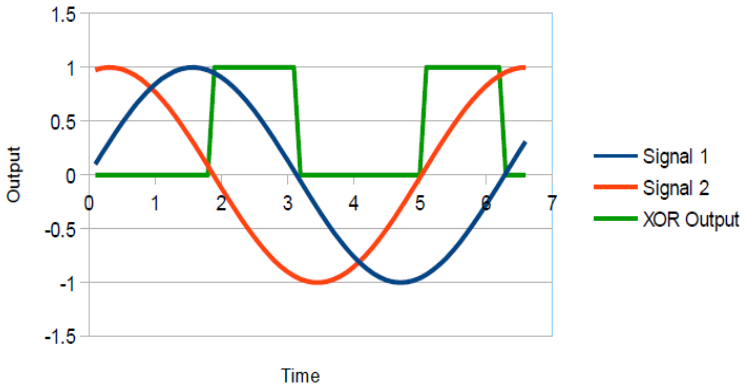

Figure 5.6: General example of the principle for phase detection. The phase delay in the two signals is reflected in the duty cycle of the XOR gate.

5.2.4. Data Processing and Output

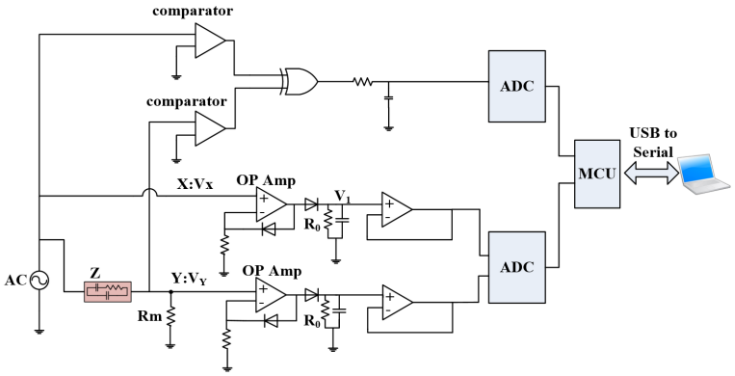

Figure 5.7: Generalized circuit diagram for the entire impedance measuring circuit combining the AC source, electrode voltage divider, magnitude detection, phase detection, and microcontroller. For the sake of simplicity, two peak detectors are shown, though just one with a switching input is used in the final design.

The previous two sections show how the circuit takes the input AC voltage, passes it through the electrode load, and outputs three values to the microcontroller: the unaltered voltage amplitude of the original AC input ($|V_x|$), the amplitude of the voltage after the signal passed through the voltage divider with the electrode ($|V_Y|$), and the phase change (θ_1). Using these values

along with the known voltage divider resistor value (R_m), the total impedance of the electrode (Z) can be found. From the voltage divider, the relationship between $|V_x|$ and $|V_Y|$ is:

$$|\frac{V_y}{V_x}| = G = \frac{R_m}{\sqrt{(R_m+R_z)^2+{X_Z}^2}} \tag{5.1}$$

Here, the ratio of the voltage magnitudes is defined by G, which will be used in later equations. Like any voltage diver, the ratio of the voltage before and after the voltage divider is equal to ratio of the resistor R_m and the sum of the electrode impedance and R_m. Here however, the magnitude of this ratio is taken, and the impedance, Z, is broken down into resistive component, R_z and its reactive component, X_z.

A similar procedure can be done for the phase change:

$$\frac{V_y\angle\theta_1}{V_x\angle 0} = \frac{R_m}{(Z+R_m)\angle\theta_2} \tag{5.2}$$

Here the voltages and impedances are expressed as phasors, with the phase of the input signal set to 0, so the phase angle after the electrode divider is equal to the total phase shift, θ_1. Since the resistor R_m, is just that, there is no phase change so the phase of the combined impedance of the electrode and R_m, θ_2 is equal to $-\theta_1$. Next, the phase angle for the voltage divider can be expressed as the ratio of the reactance and combined resistances:

$$\tan(\theta_2) = \frac{X_Z}{(R_m+R_z)} \tag{5.3}$$

This can be substituted back into the first equation which can then isolate X_z:

$$X_Z = \frac{R_m}{G\sqrt{\frac{1}{\tan^2(\theta_2)}+1}} \tag{5.4}$$

From these equations and the relationship between θ_2 and θ_1, the previous equation can be simplified as:

$$|X_Z| = |\frac{R_m}{G}\sin(\theta_2)| \tag{5.5}$$

Substituting this back into the previous equation, an expression for the resistance of the electrode can be found:

$$R_z = R_m\left(\frac{cos(\theta_2)}{G} - 1\right) \tag{5.6}$$

The total impedance Z is the vector sum of R_Z and X_Z, and each can be calculated using the known resistor R_m, the measured voltage amplitudes, V_x and V_Y, and measured phase shift.

5.2.5. Smartphone App Design[12]

In keeping with the goal of making the biosensor inexpensive and portable, smartphone and tablet apps were designed for the purposes of controlling the device, processing measurements, and displaying data.

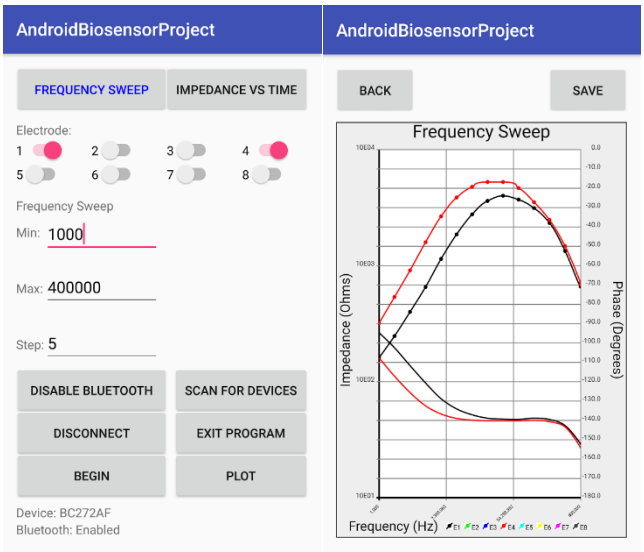

Figure 5.8: Screenshots of the impedance board control app running on an Android smartphone. Left: the control panel is used to select which IDEs on a chip will be measured, the set measurement time or frequency ranges, and for connecting to the impedance sensor. Right: the displayed results of an impeacne measurement for two IDEs (measured at the same time). This includes both the magnitude and phase of the impedance measured over a frequency range.

The app connects with the impedance board using a Bluetooth connection. The two main functions of the app are to control impedance board, and to interpret and display results from the

[12] Of all of the different components to this entire biosensor, from chemistry to microfabrication, to circuit design, I had the least direct involvement with making the app. I described the app specifications (what it should look like, what it should do, etc.) and tested the app, but the majority of the programming was done by Ryan Corpuz, Ben Flanders, Allison Chen and Samuel Lehmann. There wouldn't be an app without them.

board. The “control” portion of the app selects which electrode on an 8-electrode chip is measured (this part controls a multiplexor on the board which passes the AC voltage signal to the electrodes), as well as the type of test done. Tests can either be taken over a range of frequencies, where the app steps through a series of frequencies from input frequency limits and takes measurements at each point, or taken over a period of time at one set frequency. The “display” part of the app, displays the data in a graph. It can overlay multiple measurements, displays both impedance phase and magnitude at the same time, and can export the data in the form of a spreadsheet file.

5.3. Noise and Error Reduction

As with any circuit, signal noise and errors are inevitability. In the impedance measuring circuit noise can have various effects including inaccurate and imprecise impedance measurements, and, the more troublesome random variations in measurements. Constant errors, like those caused by inaccuracies in component specifications or constant power supply drops can be detected and calibrated out of the system (e.g. measuring a test circuit with a known impedance then correcting the discrepancy in the software). The specifications for the device are only for a specific impedance range (in this case centered around 2kΩ) and frequency range (1Hz -1MHz), so components were chosen to function best in these circumstances. At frequencies that are too high, or loads that are outside the designed range, errors occur, and components stop function in expected ways (particularly the many op amps in the circuit which only function the way they are intended to below certain frequencies).

Random noise in the circuit can be a bigger problem than constant errors. Random noise is random. It can cause unpredicted changes in measurement results, and if these changes are big enough, that can make the difference between a good result and a false reading for the biosensor. Particularly when trying to measure small concentration of a biomolecule. Because of this required accuracy, steps had to be taken to mitigate this. During initial testing, by far the largest source of noise in the circuit was at the electrode itself. As mentioned previously, the voltage going to the electrode is stepped down to 10mV, then stepped back up the same amount immediately after. This reduced voltage prevents the possibility of electrochemical reactions occurring on the electrodes. However, when the signal is stepped up, so is any noise in that signal. This noise can be significant, as the electrodes themselves pick up noise, and that is compounded by the step up in the voltage. To mitigate this problem, two filters were added to the circuit. One before the signal passes to the

electrodes and one after. Since the frequency of the signal is always known, filters were used to remove any noise outside the designed frequency range, limiting the noise in the signal significantly.

5.4. Device Testing

All of this design work would of course be useless if it did not function properly. Throughout the design and refinement process for the device it was tested in several different ways. In early stages of the design process, the circuit was tested using basic components like resistors and capacitors. Once the circuit was completed, testing expanded to include measuring the impedance of more complex circuit combinations, interdigitated electrodes, and comparing results directly to both handheld impedance meters and electrochemical measurement equipment.

5.4.1. Component Tests

The earlier tests of the impedance circuit's effectiveness were measuring the impedances of circuit components and combinations of components at a set frequency (10 kHz) and comparing the results directly to measurements taken with the Agilent LCR meter (U1733C, Agilent Technologies, Santa, Clara, CA). The accuracy of the LCR meter is stated to be 0.2%, and had been shown in early proof of concept experiments to be able to detect changes in impedance on IDEs.

TABLE 5.1: Impedance magnitude Tests and Comparison

Measured component	**Measured Impedance at 10kHz**		
	Circuit measurement	**LRC Meter measurement**	**Error**
1k Resistor	992.35 Ω	998.2 Ω	0.586%
10nF capacitor	1680.15 Ω	1710.2 Ω	1.76%
10nF || 2.2nF	1424.18 Ω	1449.5 Ω	1.75%
1k Resistor – 10nF || 2.2nF	1744.41 Ω	1770.8 Ω	1.49%
1k Resistor – 10nF capacitor	1962.75 Ω	1992.2 Ω	1.48%

(Note: "||" refers to components connected in parallel and "–" refers to components connected in series.)

Table 5.1: shows impedance magnitude measurements for combinations of resistors and capacitors in the designed impedance range (around 1-2 kΩ) at the tested frequency of 10 kHz. The percent error between the circuit result and the LCR meter measurement is constantly less than 2%.

Next, the circuit was tested over a range of frequencies. Measurements were taken at several set input frequencies between 1 kHz and 100 kHz on a circuit that is representative of an actual biosensor electrode (the equivalent circuit as shown in Figure 5.2). The tested circuit consisted of a 471pF capacitor in series with a 1 kΩ resistor both in parallel with a 1759pF capacitor. These values were chosen as they closely simulate the actual impedance values of the biosensor IDEs, while giving more consistent results.

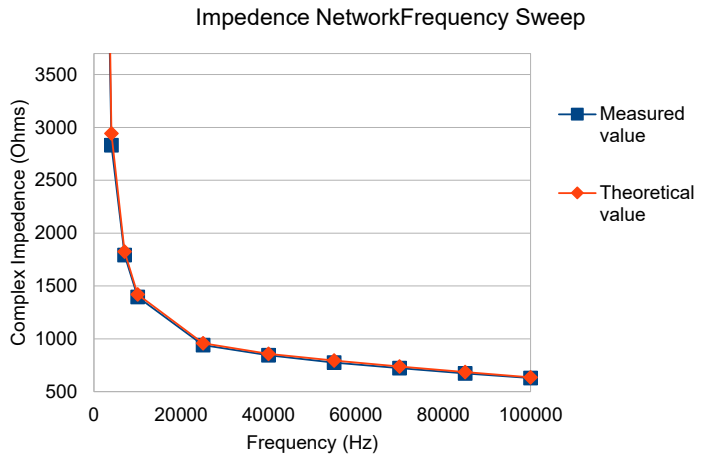

Figure 5.9: Graph of the measured results from the equivalent electrode circuit over a range of frequencies compared to the theoretical impedance magnitude value.

Shown in Figure 5.9, the results from the impedance circuit are in very close agreement with the theoretical values. The largest discrepancy is at the lowest frequency (10 kHz) with an error of 12% (note: this measurement was on a slightly older iteration of the circuit, which has since been improved upon). At higher frequencies, the error was within 3%.

5.4.2. Electrochemical Workstation Comparison

As a final, definitive test of the impedance circuit, measurements were compared directly to results from the electrochemical impedance spectroscopy workstation used for proof of concept experiments (SP-200 Potentiostat from BioLogic). The impedance of the same equivalent circuit for IDEs was measured with both the designed circuit and the potentiostat.

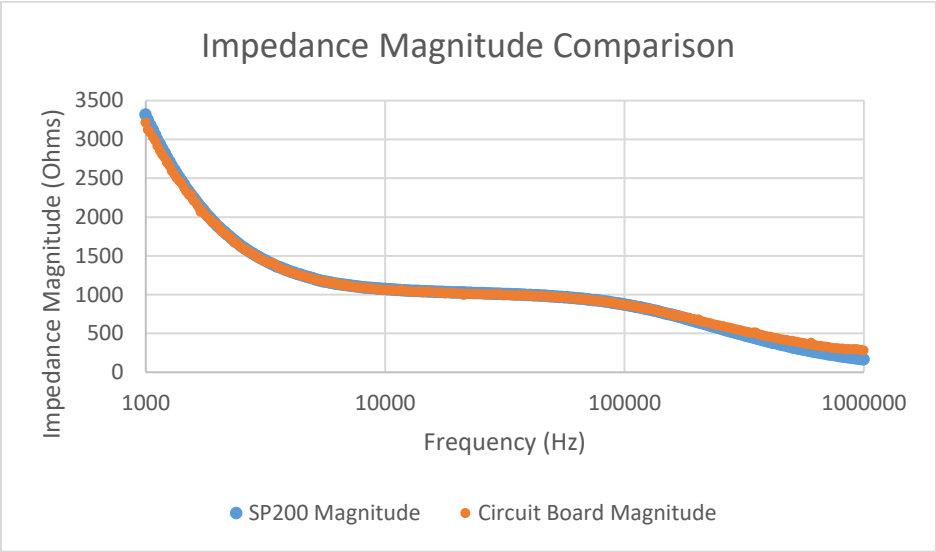

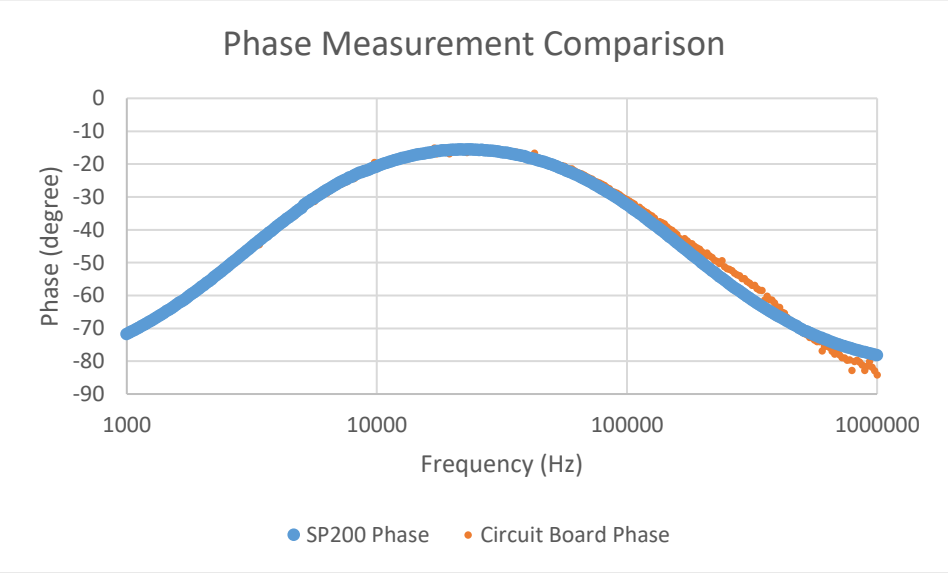

Figure 5.10: Top: Impedance magnitude measurements from the designed circuit and the SP-200 potentiostat. Bottom: Impedance phase measurements from the designed circuit and the SP-200 potentiostat.

As seen in the graphs in Figure 5.10, the impedance magnitude is in very good agreement between the two measurement devices. There is less than 1% difference through most of the frequencies, only deviating at higher frequencies close to 1MHz (with 7% error). The phase deviates from the potenitostat phase slightly more, but still only at high frequencies. These differences are due to the components in the circuit, such as the opamps, which begin to not work as designed at higher frequencies. However, these changes are not significant, as the optimal measurement frequencies are between 10 kHz and 100 kHz.

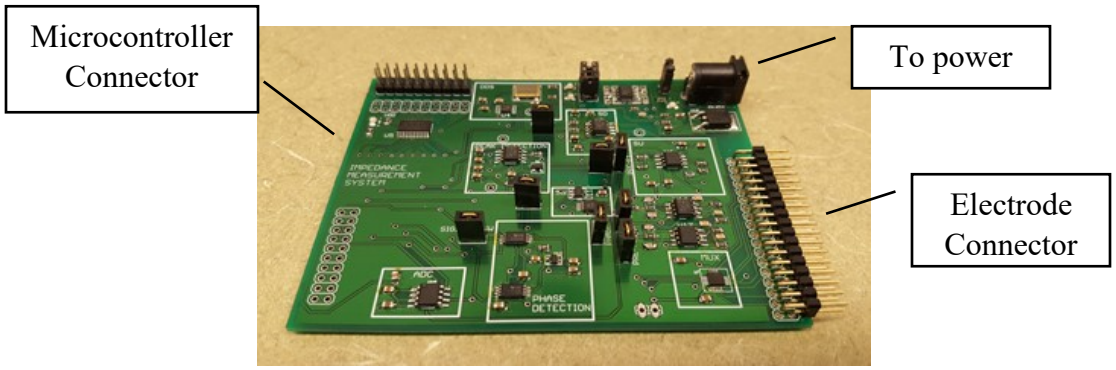

Figure 5.11: Printed circuit board for the impedance circuit. The board runs off of an external power supply (with a barrel jack on the top right) and has connectors for both the electrode chips and the microcontroller. The board has a signal generator which passes a sinusoidal voltage through the electrodes, then measures the change in voltage magnitude and phase delay. That information is passed to the microcontroller where the impedance is calculated.

5.5. Conclusion

While the bulk of design and testing of the biosensor system was carried out using preexisting electrochemical analysis hardware and software, it was by no means trivial to create an impedance measuring device that is both much smaller and much cheaper than what is currently available. Granted, this final device is much more focused on one specific task, measuring the impedance of the sensor's custom designed electrodes, at a specific frequency range over a specific range of impedances. With these constraints, this device can effectively measure the impedance of the IDEs over all frequencies or relevance with enough accuracy to be comparable to much more expensive equipment. As for cost, this device is very inexpensive, even in the prototype stage it is

currently in. The total cost of the PCB and components is under $40 (not including the Arduino, Blue tooth board, and smartphone), and with further refinement both the cost and size can be reduced significantly. Comparing that to the cost of the portable Agilent LCR meter used for testing (~$300) which can only measure impedance at a few set frequencies, or electrochemical potentiostats (~$15000-$50000) which, while much more versatile, are much larger as well, this device is certainly far less expensive.

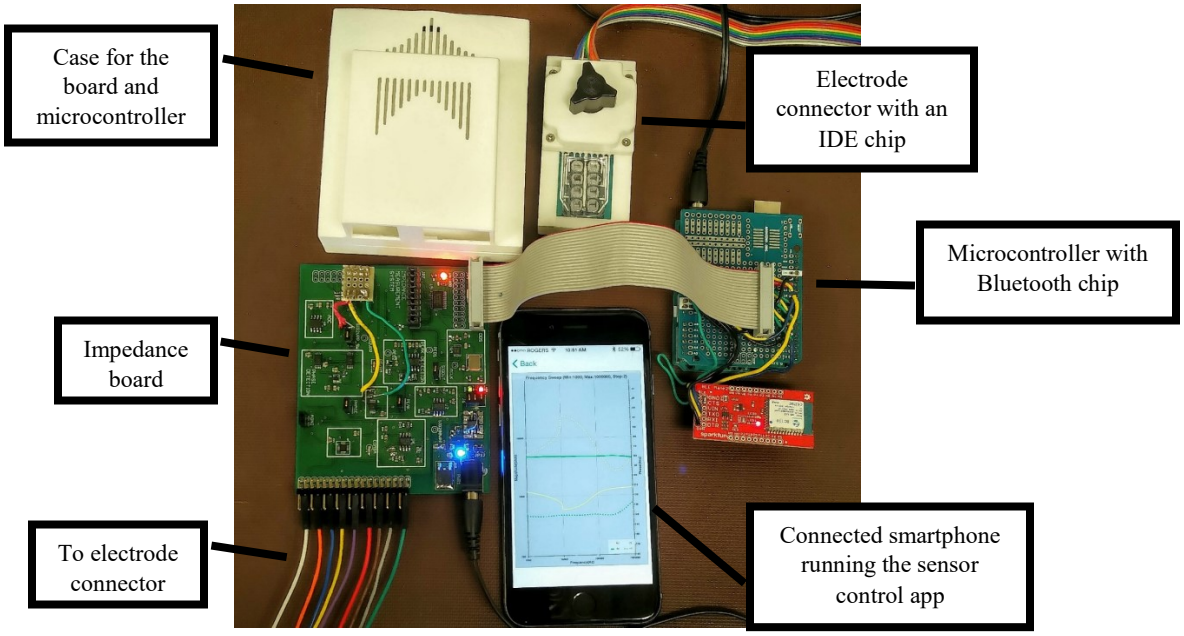

Figure 5.12: The different components of the biosensor device. Bottom left: PCB board with the impedance measuring components. Bottom middle: A smartphone with the impedance measurement app running. Right: Arduino and Bluetooth board. Top middle: An IDE electrode chip in a connector connected to the impedance board. Top left: 3D printed case for the various components.

There is still more work to do before this prototype is a finished device. This would include updates to the circuit board, making it smaller and incorporating the microcontroller and Bluetooth chip directly onto the board. Certain components can even be made into single chips eventually, further cutting down on size and potentially improving performance of the components. Noise can be further reduced by adding adaptive filters that can isolate only the frequency of interest in the signal. The app will also require redesigning for final use. The app currently serves to control the system and display impedance results. In the final device, the change in impedance of the

electrodes will have to be interpreted as a change in the number of nanoparticles bound to the electrode, and a concentration of the target biomolecule in the tested sample. That concentration will have to be used (possibly along with other results) to find and display the information in a relevant way. Other future device work will focus on making the system more automated, including a fluidics system for automatic measurements (more on that briefly in the next chapter).

Chapter 6 : Conclusions and Ongoing Work

This section includes aspects of the biosensor design that did not quite fit into the other chapters. These include parts of the device itself, or applications of the biosensor which have been investigated (if only partially in ongoing experiments and collaborations).

6.1. Fluidics

How fluidic samples and solutions interact with IDEs has not, up until this point been discussed in much detail. In the earliest experiments using cell counting e-plates, or BVT conductivity sensors, electrodes had built-in well plates. These plastic coverings were permanently attached to the electrodes and allowed for fluids to be deposited and to sit on the electrodes for periods of time. When the custom designed electrode chips were made, there were no glued on covers initially. In early testing, fluids were simply dropped directly on the electrodes, relying on surface tension to keep droplets on the electrodes. The advantage of this, beyond not having to make and somehow attach well-plate covers, is that the entire surface of the electrode chip is accessible, making treating and cleaning the whole surface (such as with plasma cleaning or extra chemical etching) easy. The disadvantages are more obvious. Only putting droplets of liquid on the electrodes limited the amount that could be applied. Droplets also dried out quickly, limiting reaction times unless great care was taken, and some surface treatments even affected the wettability of the electrodes themselves, making placing droplets on the electrodes difficult in the first place.

A solution to the fluid problem was found by using PDMS to make removable well covers for the electrode chips. PDMS is a polymer that is commonly used in microfluidics applications [139]–[141]. It can be molded into any shape and can stick to a flat surface forming a water-tight seal. PDMS well covers were custom made for all types of microfabricated electrode chips by casting PDMS on silicon wafers with 3D printed molds. The silicon wafer makes the PDMS have a perfectly smooth surface that can stick to the electrode chip. The molds are used to add the holes in the PDMS where the electrodes are, forming the wells. Each well can hold 20-50 μL of fluid (depending on the design used and the thickness of the cover). The well covers can be attached to

electrode chips by simply placing them on the chips. From there fluids can be added to the wells for chemical modifications or testing. The PDMS covers can be removed just as easily for cleaning or testing the chips, and reused after washing with ethanol.

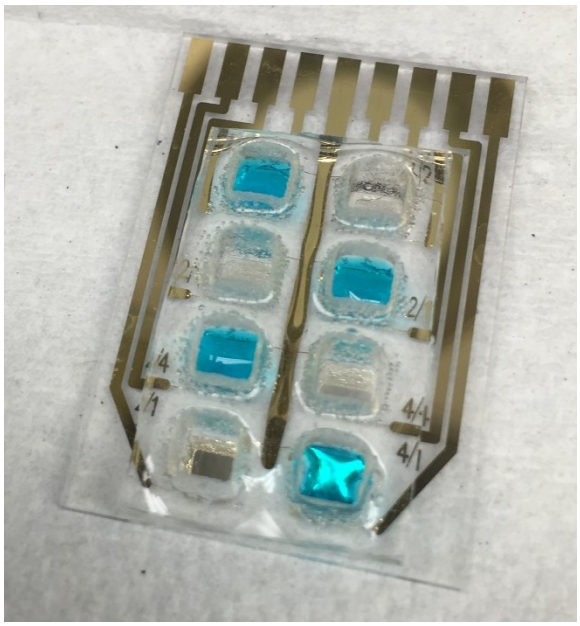

Figure 6.1: A PDMS well cover on an electrode chip. Blue coloured water is used in some of the wells. These removable covers were used for both chemically modifying the electrode surfaces and for taking impedance measurements in salt buffers. Each well holds approximately 50 µL of liquid. The blue liquid in the wells here is used to show a visual representation of the wells.

Droplets, PDMS coverings, and even affixed well covers are ultimately only temporary solutions for fluid handling during testing and design stages. One of the key goals of the final biosensor device is for it to be very easy to use. This means limiting sample handling. In an ideal system, a biosample (blood, urine, etc.) would just need to be loaded into the biosensor and the device would take care of everything itself. This would include getting the sample to the electrode (or electrodes), and washing the electrodes to remove unbound components. To do this in a controlled, automated way, a closed fluidic system was designed. In its final form, this would consist of narrow chambers over the electrode surfaces and fluidic channels going to and away from all of the electrodes. The dimensions of the channels and chambers are important as they must be small enough for laminar flow of fluids (as opposed to turbulent flow) to ensure fluid mixing doesn't occur, making washing out the chambers much easier, but large enough that

pressure can be used to move fluids through the system. Flowing fluids in a thin layer over the electrode has the added benefit of exposing more of the sample to the surface, where binding can take place. With wells or droplets, a large percentage of the sample never interacts directly with the electrode (shown in Figure 6.2). Using pressure to drive fluids through channels and over the electrodes (or an automated pump in a final system), the flow rate can be precisely controlled.

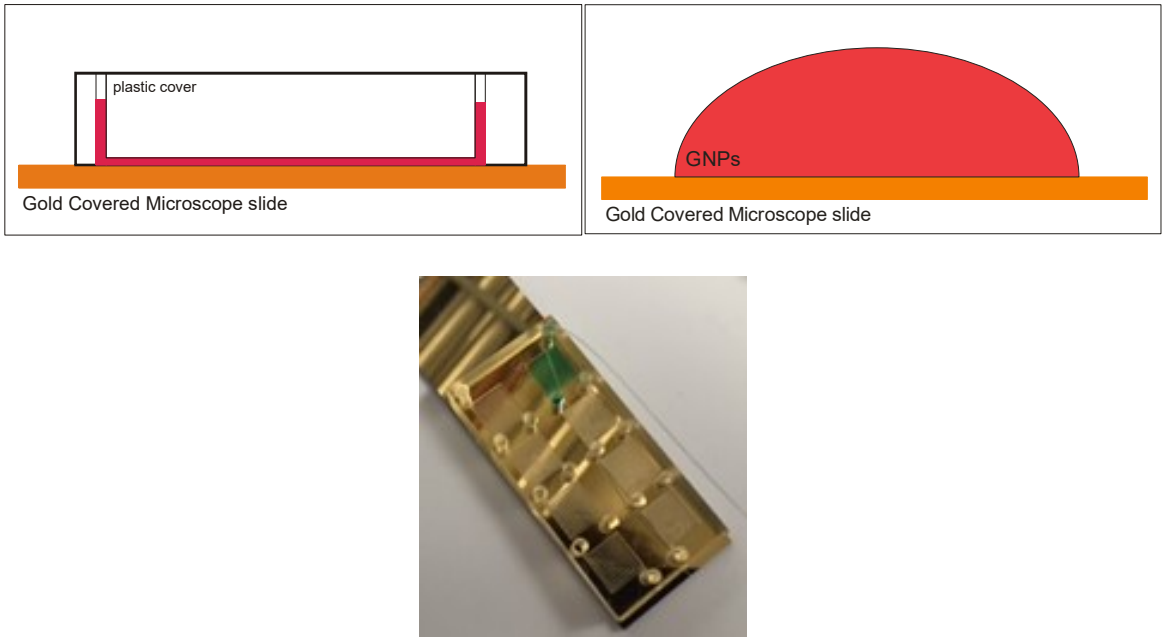

Figure 6.2: Top: basic concept of the fluidic chambers. With the fluidic cover, a thin layer of the sample flows over the electrode, exposing more of the sample to the surface. With wells or droplets, most of the fluid does not contact the surface at all. Bottom: a machined plastic cover over a gold surface. The top chamber of this cover is filled with a blue liquid (to show an example of a filled chamber). Here, a much smaller volume of liquid is used than would be used in a well or droplet on an electrode, and there is still uniform coverage over the entire surface. A fluidic system like this integrated into the sensor electrodes would reduce required sample volume and reagents (MREs, GNPs, etc.), and would lead to better control over electrode modification and washing.

The first iteration of this type of fluidic design was for the first microfabricated chips. The larger surface area of the electrodes allowed for the fluidic cover to be made from machined plastic.

Luer connections and fluidic channels were used along with syringes for injecting and pushing fluids through the system.

For the smaller electrode chips, smaller fluidic covers had to be made, and fluidic channels had to be incorporated directly onto the cover. These were accomplished by 3D printing fluidic covers. A tabletop 3D printer was purchased from MiiCraft (a Miicraft+ 3D printer, www.miicraft.com). The printer uses a clear resin that hardens in UV light. The pattern builds layers of cured resin into a final 3D clear structure. Using this printer, small fluidic channels can be made. For electrode chip covers, 0.5mm channels were made, with 0.5mm deep chambers over the electrodes. The fluidic covers were glued to electrode chips using a thin layer of uncured resin. The thin layer was applied to the bottom surface of the cover, affixed to the electrode chips (or glass), and the entire chip is exposed to UV light to harden the resin and stick the cover to the chip.

Figure 6.3: Top left: the MiiCraft tabletop 3D printer that was used to make fluidic covers for microfabricated electrodes. Top right: a 3D printed fluidic cover for a microfabricated electrode chip. There is an inlet and outlet for each electrode on the chip for samples and buffers to be added.

Bottom: individual 3D printed fluidic chambers for individual IDEs. These chambers have connections for syringes to inject fluid over the electrodes. These here are affixed to a microscope slide for demonstration purposes, and each have blue liquid in them to show the channels and the electrode area that is filled with a small volume of the liquid.

6.2. Ongoing Testing

In addition to the metabolite proof-of-concept tests, direct GNP binding tests, and I-FABP testing, several other applications for the biosensor have been, and are being investigated. Different kinds of biomolecules for different medical research applications, and collaborations for completely new applications are all in different stages of testing and planning. Tests are ongoing for detecting short strands of single stranded RNA that can be a marker for lung cancer [142]. And studies continue to detect the various metabolites outlined in the metabolite table back in the first chapter.

6.2.1. Side Project: Plant Spore Testing[13]

As a separate side project, the same sensor system, including electrodes and impedance measurements, was used for detecting spores responsible for diseases in plants. *Sclerotinia sclerotiorum* is a fungus that infects over 400 plant species including many useful crops (such as canola) [143]. Early detection of *S. sclerotiorum* spores can inform the effective use of counter measures against possible infections in crops. A collaboration was started to investigate if the same detection principles used for the biosensor system could be applied to detecting these spores. At first glance, there is little difference between detecting biological molecules and *S. sclerotiorum* spores. The spores even already had an available multiclonal antibody for binding and recognition. The big difference here is size. The biomolecules tested to this point are just that, molecules. Fungal spores are much larger, several microns across even, and have a much more complex structure. These are not necessarily completely drawbacks to detecting them, but they do force a

[13] Thanks to Afreen Anwar and Lian Shoute who worked on and continued to work on Spore testing using the sensor system. As well as Susi Li and her research group who provided the spores and antibodies for testing.

change in design. For one, there is no way the spores can be bound between electrode digits because they are bigger than the spaces between electrode digits, so the MREs have to be bound to the gold digits. The size of the spores means that they can bridge the gaps between electrodes, which can cause a change in impedance on their own, eliminating the need for signal enhancing nanoparticles. The membranes around the spores act as capacitors in the system [144], and spore also introduces a new resistivity to the system. Like similar cell counting systems which use IDEs, bound spores should therefore cause an increase in measured impedance.

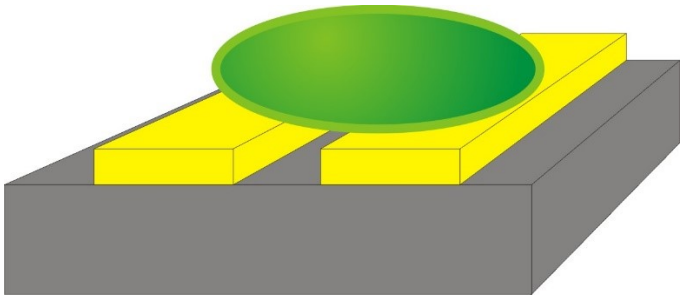

Figure 6.4: Basic diagram of a spore bound to electrode digits. The spores are large enough to bridge the gaps between electrodes. The membranes of the spores act as capacitors, and the spore itself introduces a different resistivity, causing measurable impedance changes.

While this particular side project is in a relatively early stage, there are some primary results. Spore antibodies have been modified with thiol groups and bound to gold IDEs (in the same way that DNA was bound to gold in early proof-of-concept testing), and high concentrations of spores were added to the electrodes. Impedance measurements were taken before and after spores were added to the electrodes, and optical microscope images were taken to confirm the binding of spores on the electrodes. Figure 6.5 shows the impedance results. As expected, there is an increase in impedance magnitude over the entire frequency range as well as a decrease and shift in the phase. This would indicate that the bound spores are having the expected effect of adding capacitance and extra resistivity to the system.

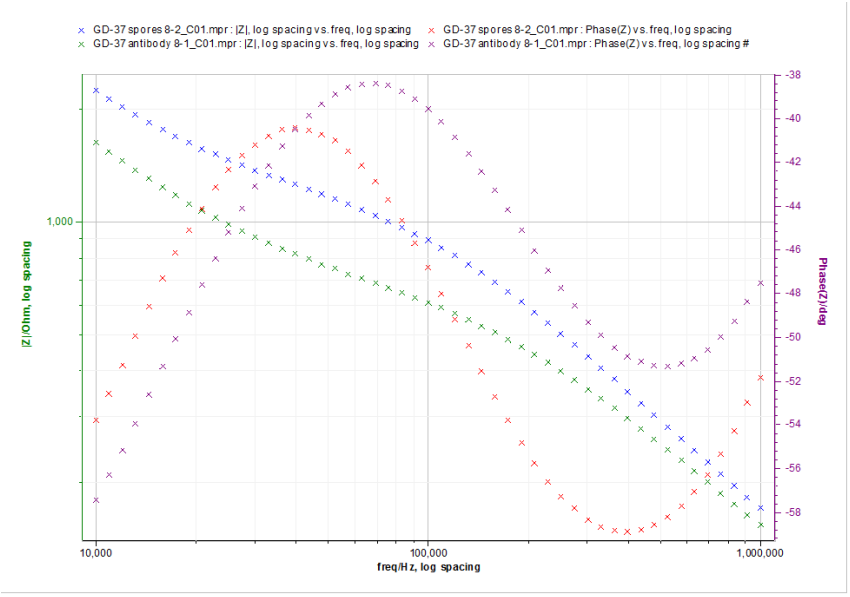

Figure 6.5: Impedance measurements before (green: impedance magnitude, and purple: phase) and after (blue: impedance magnitude, and red: phase) the addition of spores on a gold electrode (Electrode E from Table 3.3).

Microscope images of the electrodes confirmed the presence of the spores (Figure 6.6). Control tests were also done without bound antibodies to test for the potential of non-specific binding of spores. After the addition of spores to the unmodified electrodes (and washing with buffer solution), the impedance values remained the same.

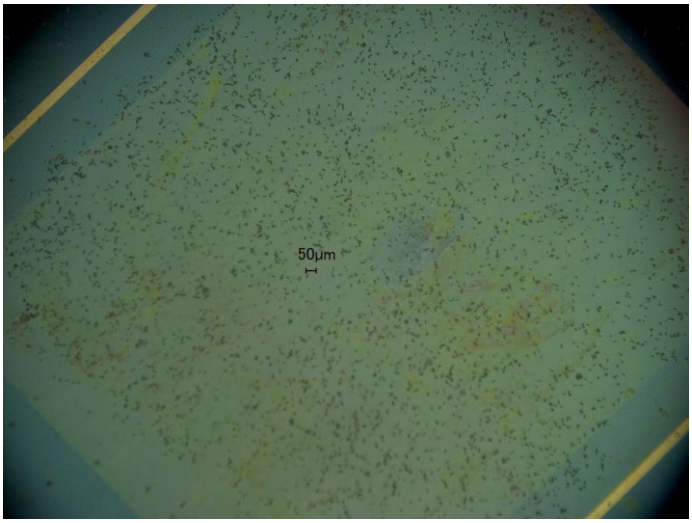

Figure 6.6: Optical microscope image of an electrode pad (Electrode E from Table 3.3) with bound spores.

While these spore detecting results are certainly promising, there is still a lot of work to be done. The key component remaining is spore concentration. These tests were done with highly concentrated pure samples of spores. In real-world applications, samples could contain many different kinds of spores and other contaminants, and the relevant concentrations of spores are so small, the sensor would have to effectively detect only a few spores (1-10) to have relevance in actual applications.

6.3. Future Work

This research has come a long way from its initial conception to this point, but it still has a long way to go. The aim was not to just prove the concept or get a working version of a sensor in a lab, but to design a usable, portable, and practical device. Future work will focus on achieving these goals. Now that the detection concept has been proven and refined, work will continue on making it more reliable, repeatable, and sensitive. Work is also continuing on testing multiple analytes, and testing in different conditions, such as blood and urine, which can introduce new, unknown elements to the system. Design work is being started to make this a usable device outside a lab environment, with handheld casings for electronic components and user-friendly updates to both software and hardware. The aim is to create an all-in-one automated device, and a key element of that is a proper fluidics handling system which can deliver samples and buffers to electrodes on the sensor automatically and consistently. This step is crucial for development of a truly point-of-

care device. A fully automated sample handling and monitoring system allows for portable use in remote environments without the requirement of specially trained personnel. Once this step is completed, the device itself can be put through regulatory approval as a sensor platform, allowing for multiple applications of the sensor technology to be developed independently. Testing is ongoing for multiple applications of the technology for research, environmental monitoring, and clinical applications. Eventually, once the technology is mature enough, the technology will be transferred to a startup company, so that the IP can be protected, and the biosensor can be certified, and distributed to researchers and medical workers for use in the real world.

6.4. Research Accomplishments

Back in Chapter 1 the goals of this thesis research were outlined. These included designing, refining and testing a versatile, portable, and inexpensive sensing system. The system should be capable of detecting a wide variety of metabolites at relevant concentrations found in biological samples, like the ones outlined in Table 1.1. The emphasis of the research was on creating a system that can detect these, rather than detecting specific markers, so aspects such as the proof-of-concept and device design were considered and tested without specific biomarkers. The subsequent chapters outlined the progress of this work. To summarize these results:

Proof-of-concept experiments showed the effect that bound gold nanoparticles can have on the impedance of interdigitated gold electrodes on both the RT-CES cell counting system, and BVT conductivity sensors measured with an LCR meter. Further testing was able to show the detection of cystine and THF metabolites. However, further refinement was necessary.

Interdigitated electrodes were designed specifically for sensing using bound gold nanoparticles. Simulations were done to help optimize the geometry and conditions for optimizing the impedance response. Using the results of these, a series of interdigitated electrodes were made using photolithography and other microfabrication techniques.

Methods for modifying the surface of the electrodes (both on electrode digits and between them) were devised in order to attach molecular recognition elements (such as antibodies, DNA, or binding proteins) for biosensing, or directly attach GNPs for testing purposes. GNPs attached directly between electrode digits did cause a measurable change in the impedance of the electrodes.

A device was designed to measure the impedance of the designed electrodes over a range of frequencies. While this device is much more specialized (limited) than the electrochemical work station that the previous testing was done with, the device is much smaller and less expensive. The device communicates wirelessly with a smartphone app for control, and data processing and display.

Work is continuing in the form of designing a fluidic system to deliver biological samples and buffers onto electrodes in small volumes in controllable ways, and testing applications of the sensor system including testing proteins and fungal spores.

While the initial goal of the research when it started was to detect a set of specific metabolites (shown in Table 1.1) in biological samples, instead the focus became developing the sensor as a general platform. Testing did not involve testing actual biological samples, and testing of some select metabolites, as well as other markers, such as fungal spores and proteins, is just now at the time of writing this currently underway.

The true novelty in this sensor, and the research and design work that went into developing the sensor, comes from its focus on being a platform technology. As described back in Chapter 1, there is no shortage of different biosensor designs. There are even a large number of proposed and actual biosensors based on electrical detection using IDEs. However, these designs are for very specific or very limited purposes. They are limited in what they can detect and how they detect them, often relying on specific labels or reactions. While these tailor-made sensors can be very capable at doing what they're designed to do, the sensor system was designed with the emphasis on versatility. By not relying on specific reactions for detection (just MREs for binding), this sensor can truly be a novel system. By developing the system as a platform technology, the possible applications are numerous.

6.4.1. Research Contributions

The research and design work described in this thesis involves and incorporates aspects from a diverse range of research backgrounds and fields of multidisciplinary study, including, but not limited to, microfabrication, nanofabrication, biochemistry, biology, surface chemistry, electrochemistry, physics, electrical circuit design, microfluidic design, and software design. And as the work spanned so many different specializations, the group of researchers working on this

project came from an equally diverse background of specialities including, but not limited to, chemists, biologists, biochemists, and engineers. Throughout this thesis I have made an effort to provide the proper credit to the individuals who made significant contributions to aspects of this work. The purpose of this section is to highlight and attempt to make completely clear the exact contributions that I (me personally) made during this work.

When I started on this project, I was under the direct supervision of two chemists who were adapting the cell counting RT-CES system into the initial proof-of-concept design for the biosensor idea. My work at this time included learning the general concepts behind the proposed design and assisting with experiments. This includes the work shown in Chapter 2.

After this, I became the "project manager" for the biosensor as a whole, directing its design, overseeing testing, and guiding the general direction of the project. This included supervising and managing a group of researchers on the project making sure the disparate aspects of the project worked well together. My supervisory role was not, however, the bulk of my contribution. I was still directly involved in the design and research process at all levels described in this thesis.

After researching the best mechanism for accomplishing the established goals for the sensor (shown in Chapter 1), I started and carried out the simulations for designing the best electrodes for this specific application (shown in Chapter 3). I directly designed the electrodes for microfabrication and oversaw and determined the microfabrication procedures used (again shown in Chapter 3).

I did direct measurements and characterization of the microfabricated electrodes and contributed to the design of the surface chemistry and biological modification of the electrodes and nanoparticles (shown in Chapter 4).

I created and designed the initial concept and prototype circuits for the impedance sensor, and continued to supervise and contribute to the final implementation of the circuit on a PCB (shown in Chapter 5).

In addition to all of these contributions, I continued to work with and oversee that diverse group of researchers (from many backgrounds and all levels of experience), as well as actively guide the trajectory of the biosensor project as a whole.

6.5. Conclusions

Years ago, at the outset of this project, there was a very clear goal: make an effective, inexpensive, portable biosensor for detecting a variety of biological metabolites. While the scope of the project has shifted slightly, to include different applications and targets, this core goal remained mostly unchanged. Initially based on technology for tracking cell culture growth, and partially inspired by other approaches in biosensing, this biosensor design has become something unique, both simple in its premise, yet deceptively complex in the number of disparate elements that come together to make everything work. From this inspiration, many different channels of design and research were carried out. Chemistry, biology, electronics, microfabrication, and fluidic design all contributed to the final device. Electrodes, with varying dimensions, designs, and materials, were simulated for the appropriate electrical and physical properties, made through various iterations and techniques, and tested. Unique techniques for surface chemistry and surface modification were researched and uniquely designed. Biological molecules like DNA and antibodies were modified and bound to electrodes or gold nanoparticles. A portable handheld device was made that can accurately measure impedance over a range of frequencies, and can communicate with smartphone apps for control and displaying data. All of these separate components work together to form the basis of the overall total biosensor, and, with future work, eventually the inexpensive, precise, versatile sensing platform technology that was first envisioned.

References

[1] S. Sharma, R. Raghav, R. O'Kennedy, and S. Srivastava, "Advances in ovarian cancer diagnosis: A journey from immunoassays to immunosensors," *Enzyme Microb. Technol.*, vol. 89, pp. 15–30, 2016.

[2] B. Lindholm-Sethson, J. Nyström, P. Geladi, R. Koeppe, A. Nelson, and C. Whitehouse, "Are biosensor arrays in one membrane possible? A combination of multifrequency impedance measurements and chemometrics," *Anal. Bioanal. Chem.*, vol. 377, no. 3, pp. 478–485, 2003.

[3] R. W. Peeling and D. Mabey, "Point-of-care tests for diagnosing infections in the developing world.," *Clin. Microbiol. Infect.*, vol. 16, no. 8, pp. 1062–1069, Aug. 2010.

[4] "Does POCT reduce the risk of error in laboratory testing?," *Clin. Chim. Acta*, vol. 404, no. 1, pp. 59–64, 2009.

[5] V. K. Omachonu, "Innovation in Healthcare Delivery Systems : A Conceptual Framework," *Innov. J.*, vol. 15, no. 1, pp. 1–20, 2010.

[6] G. Luka *et al.*, "Microfluidics integrated biosensors: A leading technology towards lab-on-A-chip and sensing applications," *Sensors (Switzerland)*, vol. 15, no. 12, pp. 30011–30031, 2015.

[7] S. Sharma, J. Zapatero-Rodr??guez, P. Estrela, and R. O'Kennedy, "Point-of-Care diagnostics in low resource settings: Present status and future role of microfluidics," *Biosensors*, vol. 5, no. 3, pp. 577–601, 2015.

[8] S. Song, L. Wang, J. Li, C. Fan, and J. Zhao, "Aptamer-based biosensors," *TrAC Trends Anal. Chem.*, vol. 27, no. 2, pp. 108–117, 2008.

[9] A. Ganjoo, H. Jain, C. Yu, J. Irudayaraj, and C. G. Pantano, "Detection and fingerprinting of pathogens: Mid-IR biosensor using amorphous chalcogenide films," *J. Non. Cryst. Solids*, vol. 354, no. 19–25, pp. 2757–2762, 2008.

[10] B. Liedberg, C. Nylander, and I. Lunström, "Surface plasmon resonance for gas detection and biosensing," *Sensors and Actuators*, vol. 4, no. C, pp. 299–304, 1983.

[11] D. Nedelkov, A. Rasooly, and R. W. Nelson, "Multitoxin biosensor-mass spectrometry analysis: A new approach for rapid, real-time, sensitive analysis of staphylococcal toxins in food," *Int. J. Food Microbiol.*, vol. 60, no. 1, pp. 1–13, 2000.

[12] J. Wang, "Glucose biosensors: 40 years of advances and challenges," *Electroanalysis*, vol. 13, no. 12, pp. 983–988, 2001.

[13] X. Zeng, Z. Shen, and R. Mernaugh, "Recombinant antibodies and their use in biosensors.," *Anal. Bioanal. Chem.*, vol. 402, no. 10, pp. 3027–38, Apr. 2012.

[14] J. A. Capobianco, W. Y. Shih, Q. A. Yuan, G. P. Adams, and W. H. Shih, "Label-free, all-electrical, in situ human epidermal growth receptor 2 detection," *Rev. Sci. Instrum.*, vol. 79, no. 7, pp. 3–5, 2008.

[15] M. Varshney and Y. Li, "Interdigitated array microelectrode based impedance biosensor coupled with magnetic nanoparticle-antibody conjugates for detection of Escherichia coli O157:H7 in food samples.," *Biosens. Bioelectron.*, vol. 22, no. 11, pp. 2408–14, May 2007.

[16] J.-M. Nam, C. S. Thaxton, and C. A. Mirkin, "Nanoparticle-based bio-bar codes for the ultrasensitive detection of proteins.," *Science*, vol. 301, no. 5641, pp. 1884–6, 2003.

[17] L. Q. Zhou and E. G. Cass, "Short communication Periplasmic binding protein based

biosensors 1 . Preliminary study of maltose binding protein as sensing element for maltose biosensor," *Biosens. Bioelectron.*, vol. 6, pp. 445–450, 1991.
[18] N. Kimura, R. Oda, Y. Inaki, and O. Suzuki, "Attachment of oligonucleotide probes to poly carbodiimide-coated glass for microarray applications.," *Nucleic Acids Res.*, vol. 32, no. 7, p. e68, Jan. 2004.
[19] M. Liu *et al.*, "A DNA tweezer-actuated enzyme nanoreactor.," *Nat. Commun.*, vol. 4, p. 2127, 2013.
[20] D. H. J. Bunka and P. G. Stockley, "Aptamers come of age - at last.," *Nat. Rev. Microbiol.*, vol. 4, no. 8, pp. 588–96, Aug. 2006.
[21] J. E. Weigand and B. Suess, "Aptamers and riboswitches: perspectives in biotechnology.," *Appl. Microbiol. Biotechnol.*, vol. 85, no. 2, pp. 229–36, Nov. 2009.
[22] S. E. Osborne, I. Matsumura, and a D. Ellington, "Aptamers as therapeutic and diagnostic reagents: problems and prospects.," *Curr. Opin. Chem. Biol.*, vol. 1, no. 1, pp. 5–9, 1997.
[23] C. Yao, T. Zhu, Y. Qi, Y. Zhao, H. Xia, and W. Fu, "Development of a quartz crystal microbalance biosensor with aptamers as bio-recognition element," *Sensors*, vol. 10, pp. 5859–5871, 2010.
[24] R. Datar, A. Passian, R. Desikan, and T. Thundat, "Microcantilever biosensors," *Proc. IEEE Sensors*, vol. 37, no. 2005, p. 5, 2007.
[25] M. Su, S. Li, and V. P. Dravida, "Microcantilever resonance-based DNA detection with nanoparticle probes," *Appl. Phys. Lett.*, vol. 82, no. 20, pp. 3562–3564, 2003.
[26] L. Tan, K. G. Neoh, E.-T. Kang, W.-S. Choe, and X. Su, "Affinity analysis of DNA aptamer-peptide interactions using gold nanoparticles.," *Anal. Biochem.*, vol. 421, no. 2, pp. 725–31, Feb. 2012.
[27] J. S. Lee and C. A. Mirkin, "Chip-based scanometric detection of mercuric ion using DNA-functionalized gold nanoparticles," *Anal. Chem.*, vol. 80, no. 17, pp. 6805–6808, 2008.
[28] J. S. Lee, P. A. Ulmann, M. S. Han, and C. A. Mirkin, "A DNA - Gold nanoparticle-based colorimetric competition assay for the detection of cysteine," *Nano Lett.*, vol. 8, no. 2, pp. 529–533, 2008.
[29] K. C. Bantz *et al.*, "Recent progress in SERS biosensing.," *Phys. Chem. Chem. Phys.*, vol. 13, no. 24, pp. 11551–67, 2011.
[30] A. I. Henry, B. Sharma, M. F. Cardinal, D. Kurouski, and R. P. Van Duyne, "Surface-enhanced Raman spectroscopy biosensing: In vivo diagnostics and multimodal imaging," *Anal. Chem.*, vol. 88, no. 13, pp. 6638–6647, 2016.
[31] J. Wang, "Glucose Biosensors: 40 Years of Advances and Challenges," *Electroanalysis*, vol. 13, no. 12, pp. 983–988, Aug. 2001.
[32] E. Yoo and S. Lee, "Glucose biosensors: An overview of use in clinical practice," *Sensors*, vol. 10, pp. 4558–4576, 2010.
[33] F. Phillips *et al.*, "Measurement of sodium ion concentration in undiluted urine with cation-selective polymeric membrane electrodes after the removal of interfering compounds," *Talanta*, vol. 74, no. 2, pp. 255–264, 2007.
[34] L. Su, W. Jia, C. Hou, and Y. Lei, "Biosensors and Bioelectronics Microbial biosensors : A review," *Biosens. Bioelectron.*, vol. 26, no. 5, pp. 1788–1799, 2011.
[35] I. R. Lauks, "Microfabricated Biosensors and Microanalytical Systems for Blood Analysis," *Acc. Chem. Res.*, vol. 31, no. 5, pp. 317–324, May 1998.
[36] M. Mascini and S. Tombelli, "Biosensors for biomarkers in medical diagnostics.,"

Biomarkers, vol. 13, no. 7, pp. 637–57, Nov. 2008.
[37] G. Patti, O. Yanes, and G. Siuzdak, “Innovation: Metabolomics: the apogee of the omics trilogy,” *Nat. Rev. Mol. Cell Biol.*, vol. 13, no. 4, pp. 263–269, 2012.
[38] M. Sugimoto, D. T. Wong, A. Hirayama, T. Soga, and M. Tomita, “Capillary electrophoresis mass spectrometry-based saliva metabolomics identified oral, breast and pancreatic cancer-specific profiles,” *Metabolomics*, vol. 6, no. 1, pp. 78–95, 2010.
[39] P. Dak and M. A. Alam, “Non-Faradaic Impedance Model of a Biochemical Sensor,” pp. 1–14, 2015.
[40] Y. Liu, Z. Matharu, and M. Howland, “Affinity and enzyme-based biosensors: recent advances and emerging applications in cell analysis and point-of-care testing,” *Anal. Bioanal. Chem.*, vol. 404, pp. 1181–1196, 2012.
[41] J. Wang, “Electrochemical biosensors: Towards point-of-care cancer diagnostics,” *Biosens. Bioelectron.*, vol. 21, no. 10, pp. 1887–1892, 2006.
[42] M. Saberian, H. Hamzeiy, A. Aghanejad, and D. Asgari, “Aptamer-based nanosensors: juglone as an attached-redox molecule for detection of small molecules,” *Bioimpacts*, vol. 1, no. 1, pp. 31–36, 2011.
[43] S. Guo and S. Dong, “Biomolecule-nanoparticle hybrids for electrochemical biosensors,” *Trends Anal. Chem.*, vol. 28, no. 1, pp. 96–109, 2009.
[44] Y. Peng, D. Zhang, Y. Li, H. Qi, Q. Gao, and C. Zhang, “Label-free and sensitive faradic impedance aptasensor for the determination of lysozyme based on target-induced aptamer displacement.,” *Biosens. Bioelectron.*, vol. 25, no. 1, pp. 94–9, Sep. 2009.
[45] M. C. Rodriguez, A.-N. Kawde, and J. Wang, “Aptamer biosensor for label-free impedance spectroscopy detection of proteins based on recognition-induced switching of the surface charge.,” *Chem. Commun. (Camb).*, no. 34, pp. 4267–4269, 2005.
[46] D. Grieshaber, R. Mackenzie, J. Vörös, and E. Reimhult, “Electrochemical Biosensors - Sensor Principles and Architectures,” *Sensors*, vol. 8, no. March, pp. 1400–1458, 2008.
[47] J. P. Zheng, P. C. Goonetilleke, C. M. Pettit, and D. Roy, “Probing the electrochemical double layer of an ionic liquid using voltammetry and impedance spectroscopy: A comparative study of carbon nanotube and glassy carbon electrodes in [EMIM]+[EtSO4]-,” *Talanta*, vol. 81, no. 3, pp. 1045–1055, 2010.
[48] C. H. Yeh, W. T. Wang, P. L. Shen, and Y. C. Lin, “A developed competitive immunoassay based on impedance measurements for methamphetamine detection,” *Microfluid. Nanofluidics*, vol. 13, no. 2, pp. 319–329, 2012.
[49] D. Xu, X. Yu, Z. Liu, W. He, and Z. Ma, “Label-free electrochemical detection for aptamer-based array electrodes,” *Anal. Chem.*, vol. 77, no. 16, pp. 5107–5113, 2005.
[50] X. Luo, M. Xu, C. Freeman, T. James, and J. J. Davis, “Ultrasensitive label free electrical detection of insulin in neat blood serum,” *Anal. Chem.*, vol. 85, no. 8, pp. 4129–4134, 2013.
[51] S. M. Radke and E. C. Alocilja, “Design and fabrication of a microimpedance biosensor for bacterial detection,” *IEEE Sens. J.*, vol. 4, no. 4, pp. 434–440, 2004.
[52] S. W. Chen and R. W. Murray, “Electrochemical quantized capacitance charging of surface ensembles of gold nanoparticles,” *J. Phys. Chem. B*, vol. 103, no. 45, pp. 9996–10000, 1999.
[53] C. Berggren and P. Stålhandske, “A feasibility study of a capacitive biosensor for direct detection of DNA hybridization,” …, pp. 156–160, 1999.
[54] N. Couniot, a. Afzalian, N. Van Overstraeten-Schl??gel, L. a. Francis, and D. Flandre,

"Capacitive biosensing of bacterial cells: Analytical model and numerical simulations," *Sensors Actuators, B Chem.*, vol. 211, pp. 428–438, 2015.

[55] S. K. Mcgraw, E. Alocilja, K. Senecal, and A. Senecal, "A Resistance Based Biosensor That Utilizes Conductive Microfibers for Microbial Pathogen Detection," *J. Appl. Biosens.*, vol. 1, no. November, pp. 36–43, 2012.

[56] R. S. Lima *et al.*, "Contactless conductivity biosensor in microchip containing folic acid as bioreceptor.," *Lab Chip*, vol. 12, no. 11, pp. 1963–1966, 2012.

[57] D. L. Chapman *et al.*, "A CMOS Electrochemical Impedance Spectroscopy (EIS) Biosensor Array.," *Sensors Actuators, B Chem.*, vol. 4, no. 1, pp. 379–90, Dec. 2010.

[58] J.-O. Lee, H.-M. So, E.-K. Jeon, H. Chang, K. Won, and Y. H. Kim, "Aptamers as molecular recognition elements for electrical nanobiosensors.," *Anal. Bioanal. Chem.*, vol. 390, no. 4, pp. 1023–32, Feb. 2008.

[59] T. Hermann and D. J. D. Patel, "Adaptive Recognition by Aptamers Nucleic Acid," *Science (80-.).*, vol. 287, no. 5454, pp. 820–825, 2000.

[60] M. Löhndorf, U. Schlecht, T. M. A. Gronewold, A. Malavé, and M. Tewes, "Microfabricated high-performance microwave impedance biosensors for detection of aptamer-protein interactions," *Appl. Phys. Lett.*, vol. 87, no. 24, pp. 1–3, 2005.

[61] M. Moreno, V. M. González, E. Rincón, a Domingo, and E. Domínguez, "Aptasensor based on the selective electrodeposition of protein-linked gold nanoparticles on screen-printed electrodes.," *Analyst*, vol. 136, no. 9, pp. 1810–5, May 2011.

[62] J. Nyagilo, M. Xiao, X. Sun, and D. P. Dave, "Gold nanoprobes for multi-modality tumor imaging," *Library (Lond).*, vol. 7576, no. 6, p. 75760X–75760X–4, 2010.

[63] J. Ahn *et al.*, "Electrical immunosensor based on a submicron-gap interdigitated electrode and gold enhancement.," *Biosens. Bioelectron.*, vol. 26, no. 12, pp. 4690–6, Aug. 2011.

[64] C. Yang, Y. Wang, J. Marty, and X. Yang, "Aptamer-based colorimetric biosensing of Ochratoxin A using unmodified gold nanoparticles indicator," *Biosens. Bioelectron.*, vol. 26, no. 5, pp. 2724–2727, 2011.

[65] Z. Chen, L. Li, H. Zhao, L. Guo, and X. Mu, "Electrochemical impedance spectroscopy detection of lysozyme based on electrodeposited gold nanoparticles.," *Talanta*, vol. 83, no. 5, pp. 1501–6, Feb. 2011.

[66] Y. Du, B. Li, and E. Wang, "Analytical potential of gold nanoparticles in functional aptamer-based biosensors," *Bioanal. Rev.*, vol. 1, pp. 187–208, 2010.

[67] P. Baptista, E. Pereira, and P. Eaton, "Gold nanoparticles for the development of clinical diagnosis methods," *Anal. Bioanal. Chem.*, vol. 391, pp. 943–950, 2008.

[68] R. Popovtzer *et al.*, "Targeted gold nanoparticles enable molecular CT imaging of cancer.," *Nano Lett.*, vol. 8, no. 12, pp. 4593–6, Dec. 2008.

[69] R. DeLong and C. Reynolds, "Functionalized gold nanoparticles for the binding, stabilization, and delivery of therapeutic DNA, RNA, and other biological macromolecules," *Nanotechnol. Sci. Appl.*, vol. 3, pp. 53–63, 2010.

[70] E. E. Connor, J. Mwamuka, A. Gole, C. J. Murphy, and M. D. Wyatt, "Gold nanoparticles are taken up by human cells but do not cause acute cytotoxicity.," *Small*, vol. 1, no. 3, pp. 325–7, Mar. 2005.

[71] N. Bhatt, P.-J. J. Huang, N. Dave, and J. Liu, "Dissociation and degradation of thiol-modified DNA on gold nanoparticles in aqueous and organic solvents.," *Langmuir*, vol. 27, no. 10, pp. 6132–7, May 2011.

[72] J. C. Love, L. A. Estroff, J. K. Kriebel, R. G. Nuzzo, and G. M. Whitesides, *Self-*

assembled monolayers of thiolates on metals as a form of nanotechnology, vol. 105, no. 4. 2005.

[73] B. Wen, J. N. Lampe, A. G. Roberts, W. M. Atkins, A. D. Rodrigues, and S. D. Nelson, "The Structure of a Tetrahydrofolate Sensing Riboswitch Reveals Two Ligand Binding Sites in a Single Aptamer," *October*, vol. 454, no. 1, pp. 42–54, 2007.

[74] M. Liss, B. Petersen, H. Wolf, and E. Prohaska, "An aptamer-based quartz crystal protein biosensor," *Anal. Chem.*, vol. 74, no. 17, pp. 4488–4495, 2002.

[75] K. Solly, X. Wang, X. Xu, B. Strulovici, and W. Zheng, "Application of real-time cell electronic sensing (RT-CES) technology to cell-based assays.," *Assay Drug Dev. Technol.*, vol. 2, no. 4, pp. 363–372, 2004.

[76] R. Ehret, W. Baumann, M. Brischwein, a Schwinde, K. Stegbauer, and B. Wolf, "Monitoring of cellular behaviour by impedance measurements on interdigitated electrode structures.," *Biosens. Bioelectron.*, vol. 12, no. 1, pp. 29–41, Jan. 1997.

[77] R. Ehret, W. Baumann, M. Brischwein, a Schwinde, and B. Wolf, "On-line control of cellular adhesion with impedance measurements using interdigitated electrode structures.," *Med. Biol. Eng. Comput.*, vol. 36, no. 3, pp. 365–70, May 1998.

[78] J. Min and A. J. Baeumner, "Characterization and Optimization of Interdigitated Ultramicroelectrode Arrays as Electrochemical Biosensor Transducers," *Electroanalysis*, vol. 16, no. 9, pp. 724–729, May 2004.

[79] E. Valera and A. Rodríguez, "Immunosensors Based on Interdigitated Electrodes for the Detection and Quantification of Pesticides in Food," *Mohammed Naguib Abd El-Ghany ...*, 2011.

[80] A. Bonanni, I. Fernández-Cuesta, X. Borrisé, F. Pérez-Murano, S. Alegret, and M. Valle, "DNA hybridization detection by electrochemical impedance spectroscopy using interdigitated gold nanoelectrodes," *Microchim. Acta*, vol. 170, pp. 275–281, Apr. 2010.

[81] D. Xu, D. Xu, X. Yu, Z. Liu, W. He, and Z. Ma, "Label-Free Electrochemical Detection for Aptamer-Based Array Electrodes," vol. 77, no. 16, pp. 5107–5113, 2005.

[82] S. Guo and S. Dong, "Biomolecule-nanoparticle hybrids for electrochemical biosensors," *TrAC Trends Anal. Chem.*, vol. 28, no. 1, pp. 96–109, 2009.

[83] W. Li *et al.*, "A sensitive, label free electrochemical aptasensor for ATP detection.," *Talanta*, vol. 78, no. 3, pp. 954–8, May 2009.

[84] E. J. D. C. Filho, L. E. B. Ribeiro, and F. Fruett, "Full Design of an Electrochemical Impedance Spectroscopy Sensor," *Work. Circuits Syst. Curitiba, Brazil*, pp. 3–6, 2013.

[85] L. Bonel, J. C. Vidal, P. Duato, and J. R. Castillo, "An electrochemical competitive biosensor for ochratoxin A based on a DNA biotinylated aptamer," *Biosens. Bioelectron.*, vol. 26, no. 7, pp. 3254–3259, 2011.

[86] Y. Yun, A. Bhattacharya, N. Watts, and M. Schulz, "A Label-Free Electronic Biosensor for Detection of Bone Turnover Markers," *Sensors*, vol. 9, pp. 7957–7969, 2009.

[87] J. M. Pingarrón, P. Yáñez-Sedeño, and A. González-Cortés, "Gold nanoparticle-based electrochemical biosensors," *Electrochim. Acta*, vol. 53, no. 19, pp. 5848–5866, 2008.

[88] Y. Li, H. J. Schluesener, and S. Xu, "Gold nanoparticle-based biosensors," *Gold Bull.*, vol. 43, no. 1, pp. 29–41, 2010.

[89] C. Deng *et al.*, "Impedimetric aptasensor with femtomolar sensitivity based on the enlargement of surface-charged gold nanoparticles.," *Anal. Chem.*, vol. 81, no. 2, pp. 739–45, Jan. 2009.

[90] Y. Iwasaki and M. Morita, "Electrochemical measurements with interdigitated array

microelectrodes," *Curr. Sep.*, vol. 1, no. 13, pp. 2–8, 1995.
[91] M. Varshney, Y. Li, B. Srinivasan, and S. Tung, "A label-free, microfluidics and interdigitated array microelectrode-based impedance biosensor in combination with nanoparticles immunoseparation for detection of Escherichia coli O157:H7 in food samples," *Sensors Actuators B Chem.*, vol. 128, no. 1, pp. 99–107, Dec. 2007.
[92] A. Cohen and R. Kunz, "Large-area interdigitated array microelectrodes for electrochemical sensing," *Sensors Actuators B Chem.*, pp. 23–29, 2000.
[93] P. Van Gerwen *et al.*, "Nanoscaled interdigitated electrode arrays for biochemical sensors," *Sensors Actuators B Chem.*, vol. 49, no. 1–2, pp. 73–80, Jun. 1998.
[94] X. Chen *et al.*, "Electrical nanogap devices for biosensing," *Mater. Today*, vol. 13, no. 11, pp. 28–41, 2010.
[95] X. Luo and J. J. Davis, "Electrical biosensors and the label free detection of protein disease biomarkers.," *Chem. Soc. Rev.*, vol. 42, no. 13, pp. 5944–62, 2013.
[96] H. A. Stone, A. D. Stroock, and A. Ajdari, "ENGINEERING FLOWS IN SMALL DEVICESMicrofluidics Toward a Lab-on-a-Chip," *Annu. Rev. Fluid Mech.*, vol. 36, no. 1, pp. 381–411, 2004.
[97] K. Kerman, M. Saito, E. Tamiya, S. Yamamura, and Y. Takamura, "Nanomaterial-based electrochemical biosensors for medical applications," *TrAC - Trends Anal. Chem.*, vol. 27, no. 7, pp. 585–592, 2008.
[98] E. Stern, R. Wagner, F. J. Sigworth, R. Breaker, T. M. Fahmy, and M. A. Reed, "Importance of the debye screening length on nanowire field effect transistor sensors," *Nano Lett.*, vol. 7, no. 11, pp. 3405–3409, 2007.
[99] S. MacKay, P. Hermansen, D. Wishart, and J. Chen, "Simulations of interdigitated electrode interactions with gold nanoparticles for impedance-based biosensing applications," *Sensors (Switzerland)*, vol. 15, no. 9, pp. 22192–22208, 2015.
[100] M. W. den Otter, "Approximate expressions for the capacitance and electrostatic potential of interdigitated electrodes," *Sensors Actuators A Phys.*, vol. 96, no. 2–3, pp. 140–144, Feb. 2002.
[101] M. Philpott and J. Glosli, "Molecular dynamics simulation of interfacial electrochemical double layer screening," *Solid-Liquid Electrochem. Interfaces*, pp. 13–30, 1997.
[102] M. E. Fisher and Y. Levin, "Criticality in ionic fluids: Debye-H??ckel theory, Bjerrum, and beyond," *Phys. Rev. Lett.*, vol. 71, no. 23, pp. 3826–3829, 1993.
[103] H. Helmholtz, "Studien Uber electrische Grenzschichten," *Ann. Phys.*, vol. 243, no. 7, pp. 337–382, 1879.
[104] M. Gouy, "Sur la constitution de la charge électrique à la surface d'un électrolyte," *J. Phys. Théorique Appliquée*, vol. 9, no. 1, pp. 457–468, 1910.
[105] D. L. Chapman, "LI. *A contribution to the theory of electrocapillarity*," *Philos. Mag. Ser. 6*, vol. 25, no. 148, pp. 475–481, 1913.
[106] O. Stern, "Zur Theorie Der Elektrolytischen Doppelschicht," *Zeitschrift für Elektrochemie und Angew. Phys. Chemie*, vol. 30, no. 21–22, pp. 508–516, 1924.
[107] D. C. Grahame, "The Role of the Cation in the Electrical Double Layer," *J. Electrochem. Soc.*, vol. 98, no. 9, p. 343, 1951.
[108] N. Gavish and K. Promislow, "Dependence of the dielectric constant of electrolyte solutions on ionic concentration," *Arxiv*, no. 2, pp. 1–5, 2012.
[109] K. Hu, D. Lan, X. Li, and S. Zhang, "Electrochemical DNA biosensor based on nanoporous gold electrode and multifunctional encoded DNA-Au bio bar codes," *Anal.*

Chem., vol. 80, no. 23, pp. 9124–9130, 2008.
[110] E. Cortés, A. a Rubert, G. Benitez, P. Carro, M. E. Vela, and R. C. Salvarezza, "Enhanced stability of thiolate self-assembled monolayers (SAMs) on nanostructured gold substrates.," *Langmuir*, vol. 25, no. 10, pp. 5661–6, May 2009.
[111] N. Phares, R. J. White, and K. W. Plaxco, "Improving the stability and sensing of electrochemical biosensors by employing trithiol-anchoring groups in a six-carbon self-assembled monolayer.," *Anal. Chem.*, vol. 81, no. 3, pp. 1095–100, Feb. 2009.
[112] R. Moeller, A. Csaki, J. M. Koehler, and W. Fritzsche, "DNA probes on chip surfaces studied by scanning force microscopy using specific binding of colloidal gold," *Nucleic Acids Res.*, vol. 28, no. 20, p. 91, 2000.
[113] "the enzyme-linked immunosorbent assay (ELISA)," *Bull. World Health Organ.*, vol. 54, no. 2, pp. 129–139, 1976.
[114] R. M. Lequin, "Enzyme immunoassay (EIA)/enzyme-linked immunosorbent assay (ELISA)," *Clin. Chem.*, vol. 51, no. 12, pp. 2415–2418, 2005.
[115] U. Hersel, C. Dahmen, and H. Kessler, "RGD modified polymers: Biomaterials for stimulated cell adhesion and beyond," *Biomaterials*, vol. 24, no. 24, pp. 4385–4415, 2003.
[116] Y. Tamada and Y. Ikada, "Cell adhesion to plasma-treated polymer surfaces," *Polymer (Guildf).*, vol. 34, no. 10, pp. 2208–2212, 1993.
[117] W. J. Ansorge, "Next-generation DNA sequencing techniques," *N. Biotechnol.*, vol. 25, no. 4, pp. 195–203, 2009.
[118] A. Bourjilat, D. Kourtiche, F. Sarry, and M. Nadi, "Interdigitated electrode biosensor for DNA sequences detection," *Proc. Int. Conf. Microelectron. ICM*, vol. 2016–March, no. 2, pp. 194–197, 2016.
[119] Z. Jingyue and F. Bernd, "Synthesis of Gold Nanoparticles Via Chemical Reduction Methods," *Nanocon*, 2015.
[120] A. D. McFarland, C. L. Haynes, C. a. Mirkin, R. P. Van Duyne, and H. a. Godwin, "Color My Nanoworld," *J. Chem. Educ.*, vol. 81, no. 4, p. 544A, 2004.
[121] J. Gao, X. Huang, H. Lui, F. Zan, and J. Ren, "Colloidal stability of gold nanoparticles modified with thiol compounds: bioconjugation and application in cancer cell imaging.," *Langmuir*, vol. 28, pp. 4464–4471, 2012.
[122] D. D. MacDonald, "Reflections on the history of electrochemical impedance spectroscopy," *Electrochim. Acta*, vol. 51, no. 8–9, pp. 1376–1388, 2006.
[123] M. E. Orazem and B. Tribollet, "Electrochemical Impedance Spectroscopy," *Annu. Rev. Anal. Chem.*, vol. 3, pp. 207–229, 2010.
[124] M. Vidotti, R. F. Carvalhal, R. K. Mendes, D. C. M. Ferreira, and L. T. Kubota, "Biosensors based on gold nanostructures," *J. Braz. Chem. Soc.*, vol. 22, no. 1, pp. 3–20, 2011.
[125] S. Kaya, P. Rajan, H. Dasari, D. C. Ingram, W. Jadwisienczak, and F. Rahman, "A Systematic Study of Plasma Activation of Silicon Surfaces for Self Assembly," *ACS Appl. Mater. Interfaces*, p. acsami.5b08358, 2015.
[126] G. N. Abdelrasoul, B. Farkas, I. Romano, A. Diaspro, and S. Beke, "Nanocomposite scaffold fabrication by incorporating gold nanoparticles into biodegradable polymer matrix: Synthesis, characterization, and photothermal effect," *Mater. Sci. Eng. C*, vol. 56, pp. 305–310, 2015.
[127] M. J. E. Fischer, "Amine Coupling Through EDC/NHS: A Practical Approach," vol. 627, pp. 55–73, 2010.

[128] T. Kim, C. H. Lee, S. W. Joo, and K. Lee, “Kinetics of gold nanoparticle aggregation: Experiments and modeling,” *J. Colloid Interface Sci.*, vol. 318, no. 2, pp. 238–243, 2008.
[129] L. Kim, T.; Crooks, R.M.; Tsen, M.; Sun, “Polymeric Self-Assembled Monolayers. 2. Synthesis and Characterization of Self-Assembled Polydiacetylene Mono- and Multilay ers,” *J. Am. Chem. Soc.*, vol. 117, pp. 3963–3967, 1995.
[130] F. Cecchet, M. Marcaccio, M. Margotti, F. Paolucci, S. Rapino, and P. Rudolf, “Redox mediation at 11-mercaptoundecanoic acid self-assembled monolayers on gold,” *J. Phys. Chem. B*, vol. 110, no. 5, pp. 2241–2248, 2006.
[131] F. P. Zamborini and R. M. Crooks, “Corrosion Passivation of Gold by n-Alkanethiol Self-Assembled Monolayers: Effect of Chain Length and End Group,” *Langmuir*, vol. 14, no. 12, pp. 3279–3286, 1998.
[132] M. D. Porter, T. B. Bright, D. L. Allara, and C. E. D. Chidsey, “Spontaneously Organized Molecular Assemblies. 4. Structural Characterization of n-Alkyl Thiol Monolayers on Gold by Optical Ellipsometry, Infrared Spetcroscopy, and Electrochemistry,” *J. Am. Chem. Soc.*, vol. 109, no. 6, pp. 3559–3568, 1987.
[133] Y. Song, Z. Li, Z. Liu, G. Wei, L. Wang, and L. Sun, “Immobilization of DNA on 11-mercaptoundecanoic acid-modified gold (111) surface for atomic force microscopy imaging,” *Microsc. Res. Tech.*, vol. 68, no. 2, pp. 59–64, 2005.
[134] R. G. Khadaroo, S. Fortis, S. Y. Salim, C. Streutker, T. A. Churchill, and H. Zhang, “I-FABP as biomarker for the early diagnosis of acute mesenteric ischemia and resultant lung injury,” *PLoS One*, vol. 9, no. 12, pp. 1–16, 2014.
[135] H. Funaoka, T. Kanda, S. Kajiura, Y. Ohkaru, and H. Fujii, “Development of a high-specificity sandwich ELISA system for the quantification of human intestinal fatty acid-binding protein (I-FABP) concentrations.,” *Immunol. Invest.*, vol. 40, no. August 2016, pp. 223–242, 2011.
[136] C. Donfack, M. Sawan, and Y. Savaria, “Implantable measurement technique dedicated to the monitoring of electrode-nerve contact in bladder stimulators.,” *Med. Biol. Eng. Comput.*, vol. 38, no. 4, pp. 465–468, 2000.
[137] J. Wright, “Peak Detectors Gain in Speed and Performance – Design Note 61.”
[138] “Half Wave Rectifier Circuit with Diagram - Learn Operation & Working.” [Online]. Available: http://www.circuitstoday.com/half-wave-rectifiers. [Accessed: 04-Apr-2017].
[139] G. Comina, A. Suska, and D. Filippini, “PDMS lab-on-a-chip fabrication using 3D printed templates.,” *Lab Chip*, vol. 14, no. 2, pp. 424–30, 2014.
[140] J. Mairhofer, K. Roppert, and P. Ertl, “Microfluidic systems for pathogen sensing: a review.,” *Sensors*, vol. 9, no. 6, pp. 4804–23, Jan. 2009.
[141] J. C. McDonald and G. M. Whitesides, “Poly (dimethylsiloxane) as a Material for Fabricating Microfluidic Devices,” *Acc. Chem. Res.*, vol. 35, no. 7, pp. 491–499, 2002.
[142] W. H. Roa, “Sputum MicroRNA Pro ling : A Novel Approach for the Early Detection of Non-Small Cell Lung Cancer,” vol. 35, no. 5, pp. 271–281, 2012.
[143] “Sclerotinia stem rot - Canola Council of Canada.” [Online]. Available: http://www.canolacouncil.org/canola-encyclopedia/diseases/sclerotinia-stem-rot/. [Accessed: 04-Apr-2017].
[144] M. L. López Rodriguez, C. Benimeli, R. E. Madrid, and C. E. Giacomelli, “A simple Streptomyces spore-based impedimetric biosensor to detect lindane pesticide,” *Sensors Actuators, B Chem.*, vol. 207, no. Part A, pp. 447–454, 2015.

Appendix A: Electrode Mask Designs

The following figures are the mask designs used for the microfabrication of the various iterations of electrode chips.

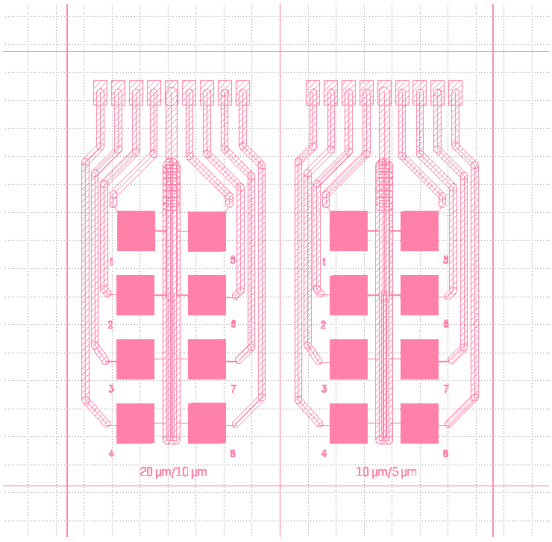

The first iteration of fabricated electrode chips are based directly on purchased electrodes (printed on plastic with much larger dimensions). These chips are large, with only two full chips with eight electrodes each fitting on each wafer. IDEs have two configurations: 20 µm digit width with 10 µm spacing between adjacent digits and 10 µm digit width with 5 µm spacing between adjacent digits.

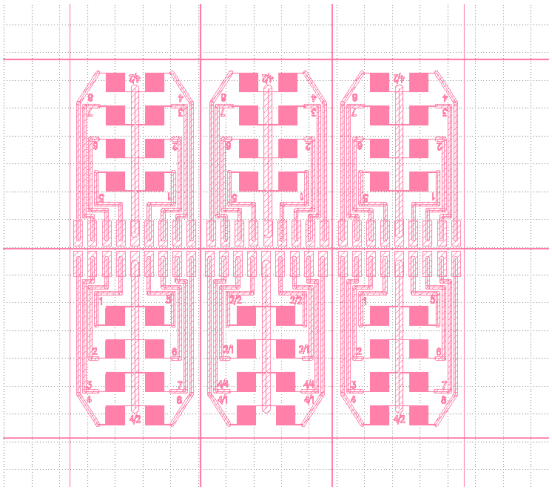

The next iteration features a much more compact design, with six electrode chips fitting onto a single wafer. There are still eight IDEs on each chip. Five out of the six chips have IDEs with 4

μm digit width and 2 μm spacing between adjacent digits, and the sixth has four different configurations for testing purposes.

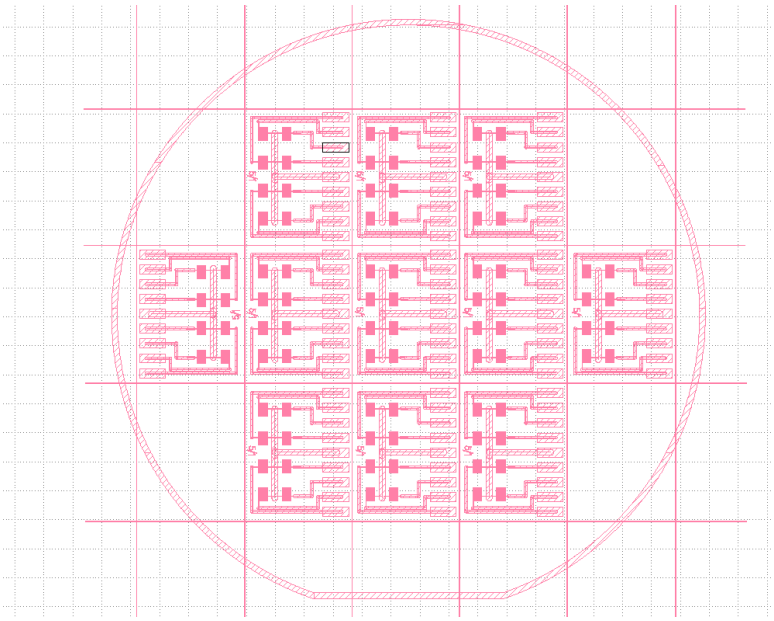

The newest iteration of electrode chips that have been made. They are about a third of the size of the previous chips and eleven can fit onto a single wafer. The electrical contacts on the chips were kept the same as the previous design so the connector used with the impedance measuring equipment did not have to be redesigned. Electrodes have 5 μm digit width with 1 μm spacing between adjacent digits

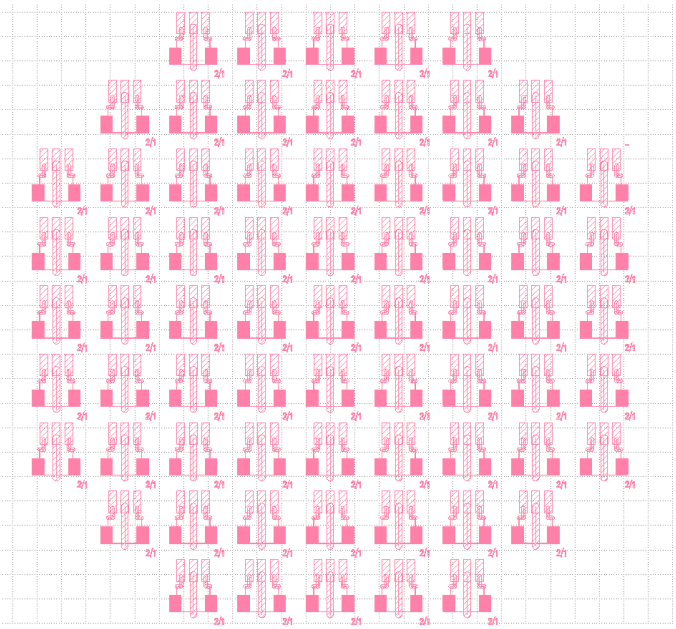

This alternate design was made for a larger wafer process, but has not yet been used for actual electrodes. There are eighty-three chips on each wafer, with two IDEs on each with 2 μm digit width and 1 μm spacing between adjacent digits.

Appendix B: PDMS Fabrication Procedure

1. In a Petri dish, pour both base and curing agent into a container using a 10:1 mass ratio.

2. Stir the two chemicals for 5 minutes.

3. Put the mixture into a vacuum desiccator and pump the chamber down to below 65 kPa for 60 minutes to remove bubbles from the mixture.

4. Pour the mixture in the center of a cleaned silicon wafer piece in an aluminum foil boat. Place the 3D printed mold into the solution and agitate to remove voids.

5. Let the substrate sit for a few minutes after pouring

6. Bake the PDMS coated substrate at 100°C for 1 hour.

7. Peel the PDMS film of the substrate, a razor blade or scalpel can be used to start the peel.

Appendix C: Impedance PCB Layout

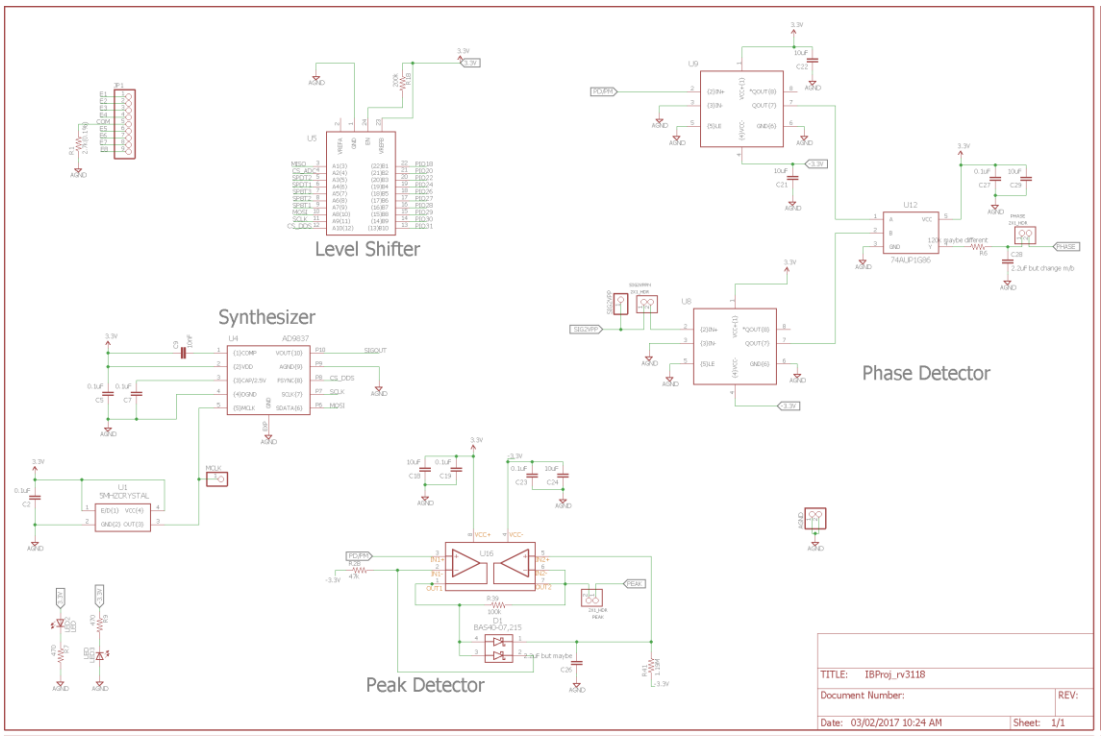

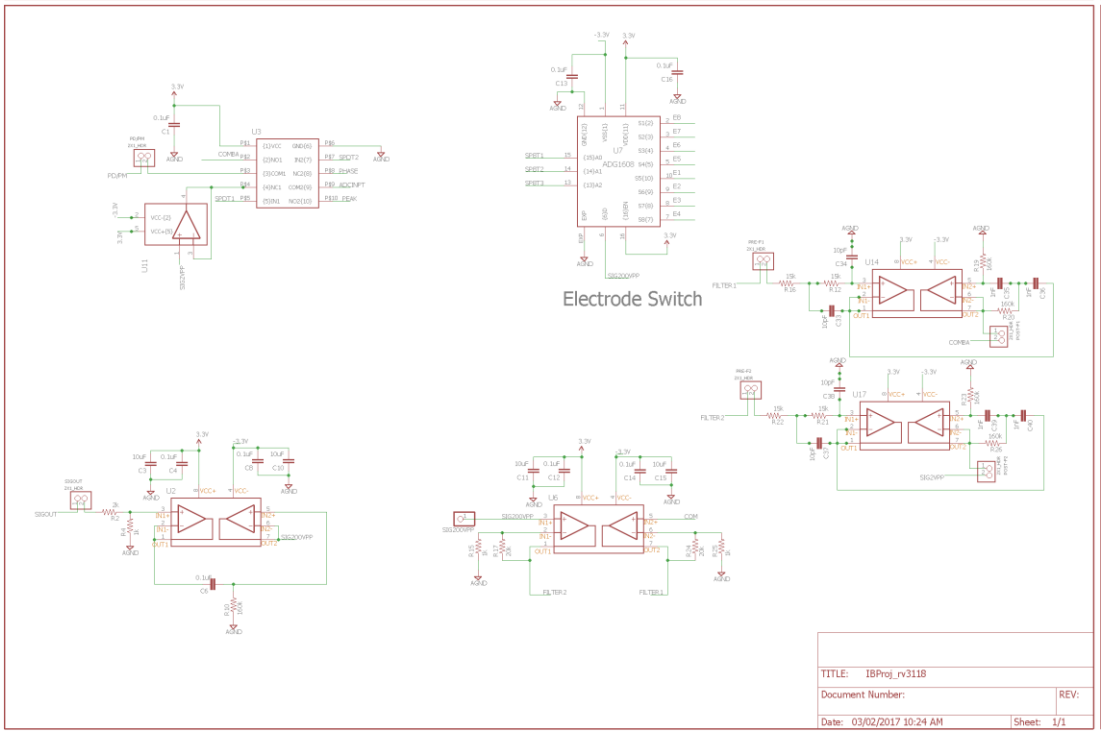

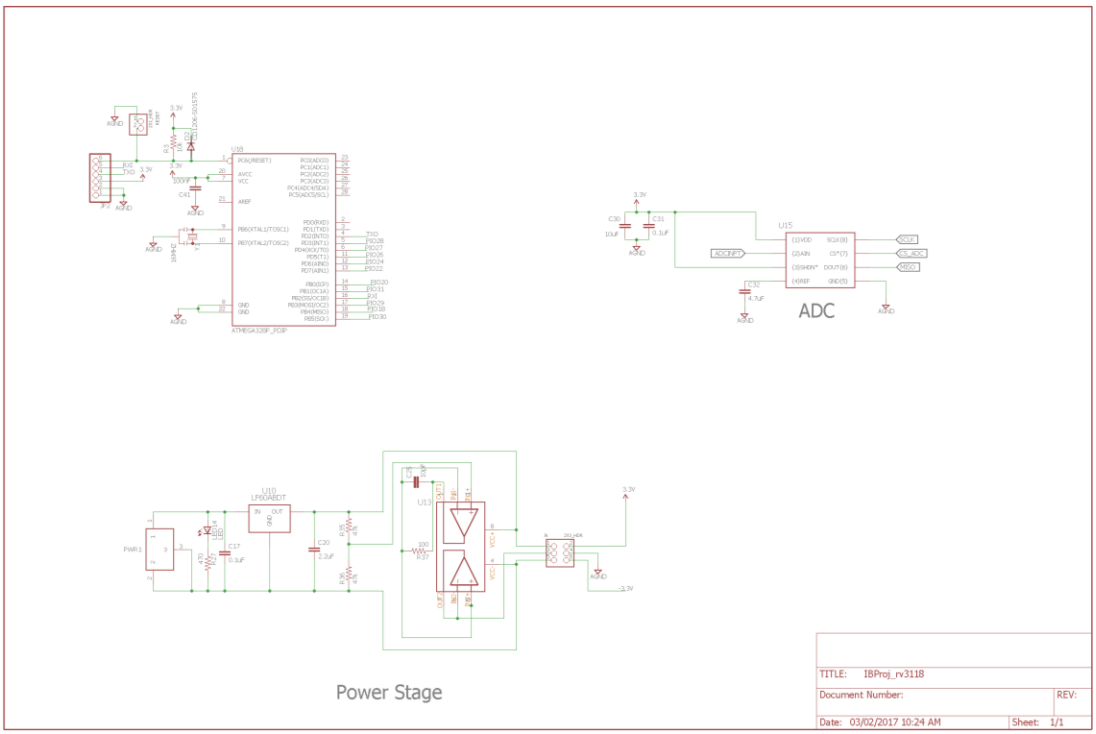
ADC
Power Stage
TITLE: IBProj_rv3118
Document Number:
REV:
Date: 03/02/2017 10:24 AM
Sheet: 1/1

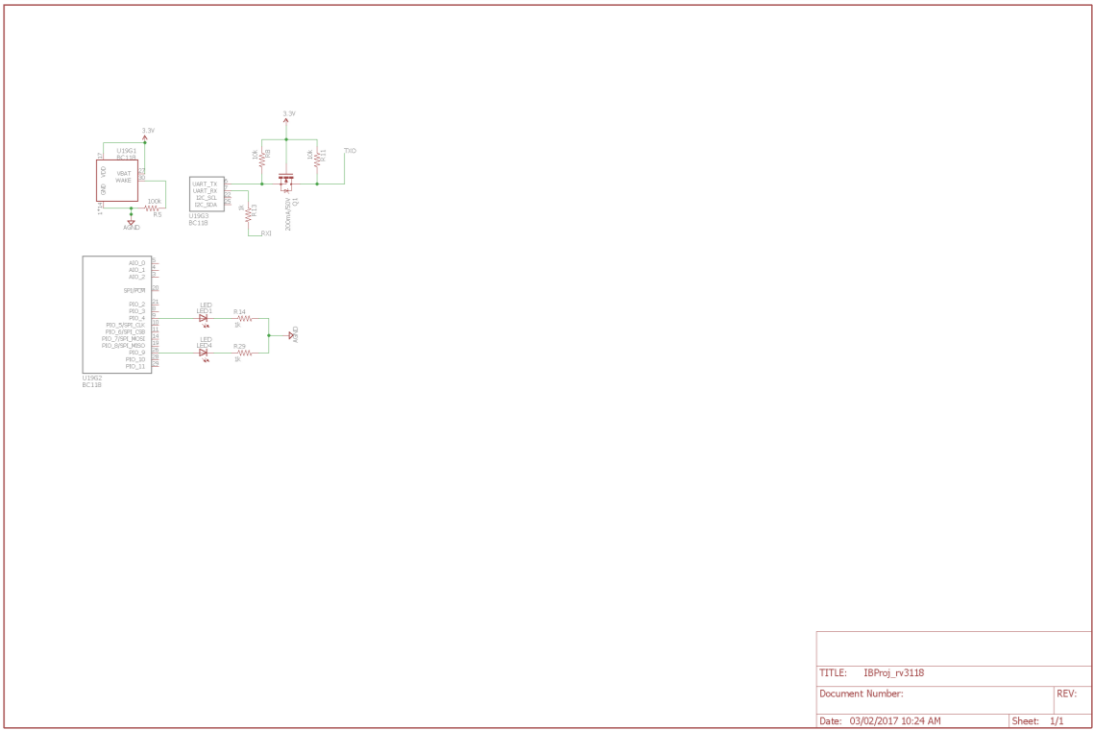
TITLE: IBProj_rv3118
Document Number:
REV:
Date: 03/02/2017 10:24 AM
Sheet: 1/1

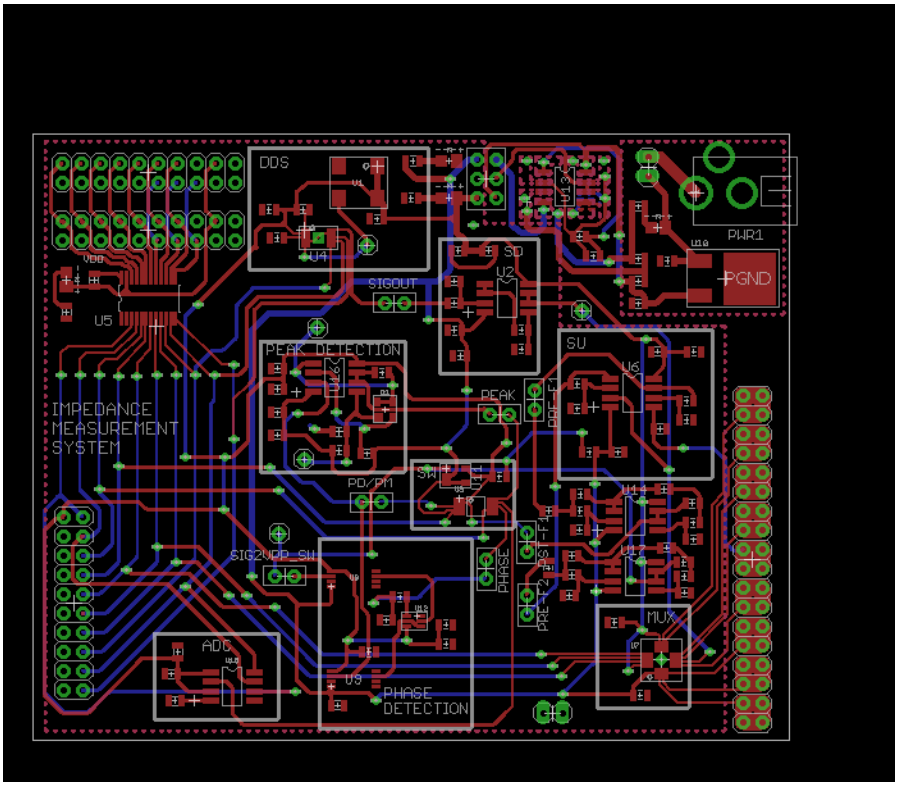
DDS
SD
SIGOUT
PEAK DETECTION
PEAK
SU
IMPEDANCE
MEASUREMENT
SYSTEM
PD/PM
SW
SIG2VDD_SW
PHASE
ADC
PHASE
DETECTION
MUX
PWR1
PGND